Defense Threat Reduction Agency
8725 John J. Kingman Road, MS 6201
Fort Belvoir, VA 22060-6201

DTRA-TR-03-25

TECHNICAL REPORT

Seismic Calibration of Group 1 IMS Stations in Eastern Asia for Improved IDC Event Location

Approved for public release; distribution is unlimited.

April 2006

DTRA 01-00-C-0024

J.R. Murphy et, al

Prepared by:
Science Applications International Corporation
Mail Stop X1
10260 Campus Drive
San Diego, CA 92121-

DARE Tracking
73765

DESTRUCTION NOTICE

<u>FOR CLASSIFIED</u> documents, follow the procedures in DoD 5550.22-M, National Industrial Security Program Operating Manual, Chapter 5, Section 7 (NISPOM) or DoD 5200.1-R, Information Security Program Regulation, Chapter 1X.

<u>FOR UNCLASSIFIED</u> limited documents, destroyed by any method that will prevent disclosure of contents or reconstruction of the document.

Retention of this document by DoD contractors is authorized in accordance with DoD 5220.22M, Industrial Security manual.

PLEASE NOTIFY THE DEFENSE THREAT REDUCTION AGENCY, ATTN: IMMI, 8725 JOHN J. KINGMAN ROAD, MS-6201, FT. BELVOIR, VA 22060-6201. IF YOUR ADDRESS IS INCORRECT, IF YOU WISH IT DELETED FROM THE DISTRIBUTION LIST, OR IF THE ADDRESSEE IS NO LONGER EMPLOYED BY YOUR ORGANIZATION.

DISTRIBUTION LIST UPDATE

This mailer is provided to enable DTRA to maintain current distribution lists for reports. (We would appreciate you providing the requested information.)

- ☐ Add the individual listed to your distribution list.
- ☐ Delete the cited organization/individual.
- ☐ Change of address.

Note:
Please return the mailing label from the document so that any additions, changes, corrections or deletions can be made easily. For distribution cancellation or more information call DTRA/BDLMI (703) 767-4725.

NAME: ____________________

ORGANIZATION: ____________________

OLD ADDRESS	**NEW ADDRESS**
____________________	____________________
____________________	____________________
____________________	____________________

TELEPHONE NUMBER: (   ) ____________________

DTRA PUBLICATION NUMBER/TITLE	**CHANGES/DELETIONS/ADDITONS, etc.** *(Attach Sheet if more Space is Required)*
____________________	____________________
____________________	____________________
____________________	____________________

DTRA or other GOVERNMENT CONTRACT NUMBER: ____________________

CERTIFICATION of NEED-TO-KNOW BY GOVERNMENT SPONSOR (if other than DTRA):

SPONSORING ORGANIZATION: ____________________

CONTRACTING OFFICER or REPRESENTATIVE: ____________________

SIGNATURE: ____________________

DEFENSE THREAT REDUCTION AGENCY
ATTN: BDLMI
8725 John J Kingman Road, MS 6201
Fort Belvoir, VA 22060-6201

DEFENSE THREAT REDUCTION AGENCY
ATTN: BDLMI
8725 John J Kingman Road, MS 6201
Fort Belvoir, VA 22060-6201

REPORT DOCUMENTATION PAGE

Form Approved
OMB No. 0704-0188

1. REPORT DATE *(DD-MM-YYY)* April 2006	**2. REPORT TYPE** Technical Report	**3. DATES COVERED** *(From - To)*
4. TITLE AND SUBTITL Seismic Calibration of Group 1 IMS Stations in Eastern Asia for Improved IDC Event Location (U)		**5a. CONTRACT NUMBER** DTRA 01-00-C-0024 **5b. GRANT NUMBER** **5c. PROGRAM ELEMENT NUMBER** 134D
6. AUTHOR(S) J.R. Murphy, W.L. Rodi, M. Johnson, J.D. Sultanov, T.J. Bennett, M.N. Toksoz, V. Ovtchinnikov, B.W. Barker, A.M. Rosca, and Y. Shchukin		**5d. PROJECT NUMBER** CO **5e. TASK NUMBER** IS **5f. WORK UNIT NUMBER** DH01578
7. PERFORMING ORGANIZATION NAME(S) AND ADDRESS(ES) Science Applications International Corp. 10260 Campus Point Drive, MS X1 Santa Diego, CA 92121		**8. PERFORMING ORGANIZATION REPORT NUMBER** SAID-03-/1022
9. SPONSORING / MONITORING AGENCY NAME(S) AND ADDRESS(ES) Defense Threat Reduction Agency 8725 John J. Kingman Rd., MS 6201 Fort Belvoir, VA 22060-6201		**10. SPONSOR/MONITOR'S ACRONYM(S)** DTRA **11. SPONSOR/MONITOR'S REPORT NOS.** TR-03-25

12. DISTRIBUTION / AVAILABILITY STATEMENT
Approved for public release; distribution is unlimited.

13. SUPPLEMENTARY NOTES
This work was sponsored by the Defense Threat Reduction Agency under the RDT&E RMC Code B 134D D 4000 CO IS 01578 24904D.

14. ABSTRACT
The determination of accurate seismic locations for detected events is one of the most important functions of nuclear test monitoring because location plays such a key role in nuclear test monitoring. In order to establish a robust nuclear test monitoring capability, it is necessary to calibrate the IMS seismic stations, used in monitoring, to account for systematic deviations from the nominal travel time curves. This report presents a summary of the research which has been accomplished during the three year program directed at the seismic calibration of the 30 Group 1 IMS stations of Eastern Asia. A Consortium of institutions, led by SAIC (formerly Maxwell Technologies, Inc.) was assembled to address this calibration effort. This consortium included the Massachusetts Institute of Technology's Earth Resources Laboratory, Weston Geophysical Corporation and the Russian Institute for Dynamics of the Geospheres. The consortium approach used a three dimensional velocity model to estimate SSSC at each station, supplemented with empirical corrections to take rigorous account of all the calibration data available for source regions surrounding each station. P-wave and S-wave SSSCs now have been determined and delivered to DTRA for all 30 Group 1 stations for surface focus and ten additional source depths.

15. SUBJECT TERMS

Seismic location	IMS	Regional monitoring	IDC	
Calibration	IASPEI91	SSSC	Finite difference	Ray tracing

16. SECURITY CLASSIFICATION OF:			**17. LIMITATION OF ABSTRACT**	**18. NUMBER OF PAGES**	**19a. NAME OF RESPONSIBLE PERSON**
a. REPORT Unclassified	**b. ABSTRACT** Unclassified	**c. THIS PAGE** Unclassified	SAR	130	**19b. TELEPHONE NUMBER** *(include area code)*

Standard Form 298 (Rev. 8-98)
Prescribed by ANSI Std. Z39.18

CONVERSION TABLE

Conversion Factors for U.S. Customary to metric (SI) units of measurement.

MULTIPLY ⟶ BY ⟶ TO GET

TO GET ⟵ BY ⟵ DIVIDE

angstrom	1.000 000 x E -10	meters (m)
atmosphere (normal)	1.013 25 x E +2	kilo pascal (kPa)
bar	1.000 000 x E +2	kilo pascal (kPa)
barn	1.000 000 x E -28	meter^2 (m^2)
British thermal unit (thermochemical)	1.054 350 x E +3	joule (J)
calorie (thermochemical)	4.184 000	joule (J)
cal (thermochemical/cm^2)	4.184 000 x E -2	mega joule/m^2 (MJ/m^2)
curie	3.700 000 x E +1	*giga bacquerel (GBq)
degree (angle)	1.745 329 x E -2	radian (rad)
degree Fahrenheit	$t_k = (t^o f + 459.67)/1.8$	degree kelvin (K)
electron volt	1.602 19 x E -19	joule (J)
erg	1.000 000 x E -7	joule (J)
erg/second	1.000 000 x E -7	watt (W)
foot	3.048 000 x E -1	meter (m)
foot-pound-force	1.355 818	joule (J)
gallon (U.S. liquid)	3.785 412 x E -3	meter^3 (m^3)
inch	2.540 000 x E -2	meter (m)
jerk	1.000 000 x E +9	joule (J)
joule/kilogram (J/kg) radiation dose absorbed	1.000 000	Gray (Gy)
kilotons	4.183	terajoules
kip (1000 lbf)	4.448 222 x E +3	newton (N)
kip/inch^2 (ksi)	6.894 757 x E +3	kilo pascal (kPa)
ktap	1.000 000 x E +2	newton-second/m^2 (N-s/m^2)
micron	1.000 000 x E -6	meter (m)
mil	2.540 000 x E -5	meter (m)
mile (international)	1.609 344 x E +3	meter (m)
ounce	2.834 952 x E -2	kilogram (kg)
pound-force (lbs avoirdupois)	4.448 222	newton (N)
pound-force inch	1.129 848 x E -1	newton-meter (N-m)
pound-force/inch	1.751 268 x E +2	newton/meter (N/m)
pound-force/foot^2	4.788 026 x E -2	kilo pascal (kPa)
pound-force/inch^2 (psi)	6.894 757	kilo pascal (kPa)
pound-mass (lbm avoirdupois)	4.535 924 x E -1	kilogram (kg)
pound-mass-foot^2 (moment of inertia)	4.214 011 x E -2	kilogram-meter^2 (kg-m^2)
pound-mass/foot^3	1.601 846 x E +1	kilogram-meter^3 (kg/m^3)
rad (radiation dose absorbed)	1.000 000 x E -2	**Gray (Gy)
roentgen	2.579 760 x E -4	coulomb/kilogram (C/kg)
shake	1.000 000 x E -8	second (s)
slug	1.459 390 x E +1	kilogram (kg)
torr (mm Hg, 0^0 C)	1.333 22 x E -1	kilo pascal (kPa)

*The bacquerel (Bq) is the SI unit of radioactivity; 1 Bq = 1 event/s.

**The Gray (GY) is the SI unit of absorbed radiation.

TABLE OF CONTENTS

FIGURES

TABLES

SECTION 1

INTRODUCTION

1.1 BACKGROUND

The determination of accurate seismic locations for detected events is one of the most important aspects of nuclear test monitoring because location plays such a key role in event identification. More specifically, a nominal event location uncertainty area of 1000 km^2 is often quoted as an ultimate location performance goal, consistent, for example, with the onsite inspection area limit established during the negotiations leading up to the CTBT. However, it has proven difficult to demonstrate that this level of accuracy can be routinely achieved, particularly for small events recorded by limited numbers of monitoring stations. The principal reason for this difficulty is that the earth is laterally heterogeneous over a very broad range of length scales; and, therefore, travel time curves based on radially symmetric earth models, such as the standard IASPEI91 model, can be seriously in error for some source and station locations. This problem is particularly acute at regional distances where the propagation paths of the seismic phases used in location are predominantly confined to the crust and upper mantle portions of the earth which exhibit the greatest regional variability. Since many of the small seismic events, which are of primary concern in nuclear test monitoring, will have to be located using regional seismic data, such variability places significant limitations on currently achievable location accuracy. It follows that in order to establish a robust nuclear test monitoring capability, it will be necessary to calibrate the seismic monitoring stations to account for such systematic deviations from the nominal travel time curves.

This report presents a summary of the research which has been accomplished over the past three years in a program directed at the seismic calibration of the 30 Group 1 IMS stations of Eastern Asia shown in Figure 1-1. These Group 1 stations include 11 Primary and 19 Auxiliary stations of the IMS network, and it can be seen from this figure that the area sampled by the regional distance ranges around these stations (i.e. out to 20°) encompasses much of the vast landmass of central and eastern Asia. Simply stated,

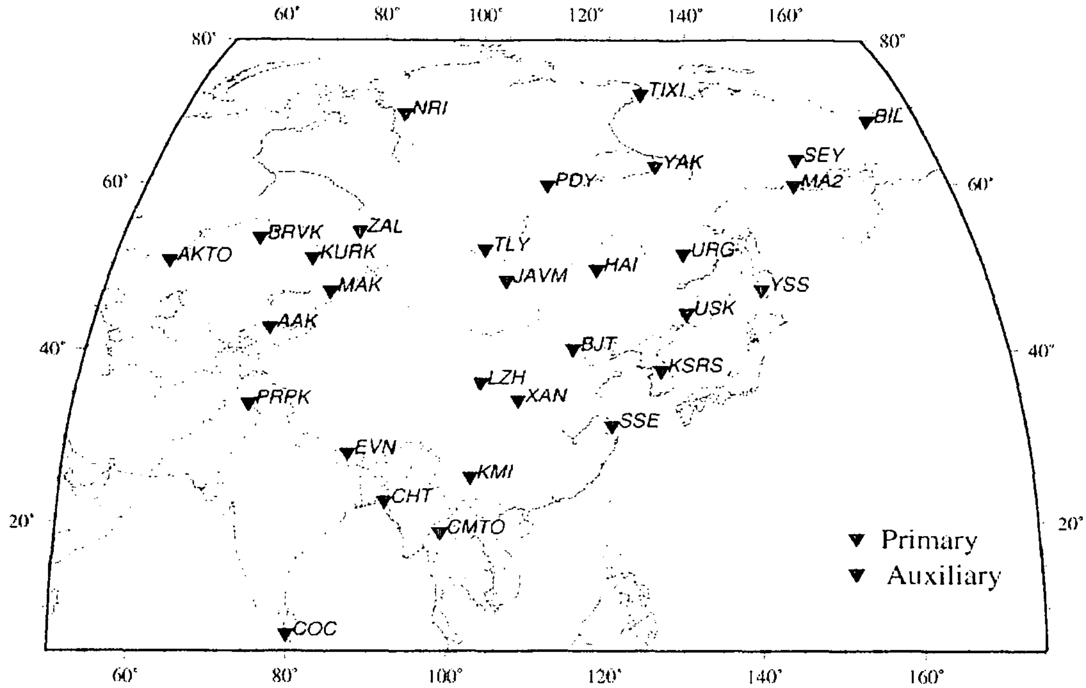

Figure 1-1. Map of IMS station locations in Group 1 study region.

the objective of our research has been to calibrate the travel time characteristics of the crust and upper mantle structure beneath this region over the depth range sampled by the regional seismic ray paths to these stations from all seismic source locations of potential interest.

A Consortium of institutions led by SAIC was assembled to address this Group 1 IMS station calibration effort. This consortium included the Massachusetts Institute of Technology's Earth Resources Laboratory (ERL), Weston Geophysical Corporation, and the Russian Institute for Dynamics of the Geospheres (IDG). Jack Murphy of SAIC was the principal investigator on the project and was responsible for its overall direction and coordination. The MIT/ERL group leader was Nafi Toksöz, Jim Lewkowicz was leader of the Weston Geophysical Corporation effort, and Jamil Sultanov was the leader of the Russian IDG effort. In general, responsibilities for the different aspects of this research have been divided between the participating institutions to facilitate and focus efforts, although collaboration between the groups has also assisted in identifying and resolving specific research issues. Participants in the project are listed in Figure 1-2. W. Rodi of

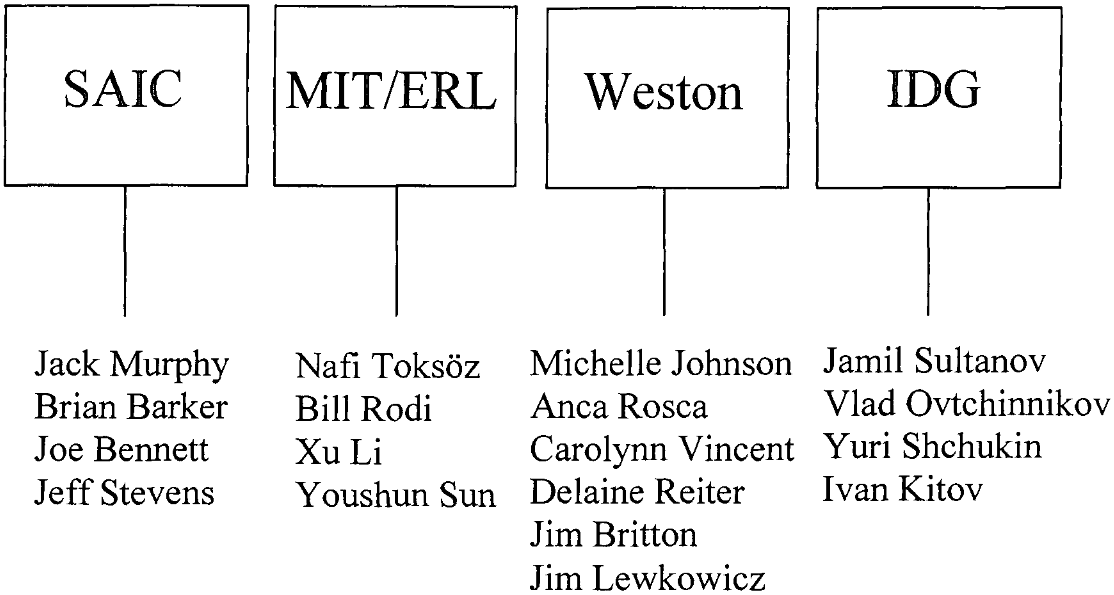

Figure 1-2. Study participants from the various institutions of the Group 1 IMS station calibration consortium.

ERL had overall responsibility for modeling and statistics. N. Toksöz and his colleagues at MIT focused on the development of an improved velocity model for China. The Weston group, led by M. Johnson, had lead responsibility for ray tracing, implementation of the tomography algorithm and computation of our travel time correction estimates. The IDG group, led by J. Sultanov and V. Ovtchinnikov, had primary responsibility for preliminary model development and ground truth compilation for the region bounded by the territories of the former Soviet Union.

1.2 GENERAL APPROACH

Our strategy for addressing this research problem was based on the belief that, in order to be successful, the proposed program to improve regional seismic location capability in this study area would have to be based on a carefully crafted scientific approach, which effectively merges the limited observed calibration data with rigorous seismological and statistical modeling procedures. The ultimate goal is to generate accurate 3-D travel time tables for each station and seismic phase. Each table contains predicted travel times to the station from every point of a 3-D grid of prospective event hypocenters around the station, nominally spaced at 1° distance intervals and representative depth intervals.

Given such a table, the predicted travel time for an arbitrary hypocenter can be calculated via interpolation between grid points. Subtracting the predicted IASPEI91 travel time for each grid point from the corresponding table travel time yields a correction (with respect to IASPEI91) as a function of source hypocenter location for each IMS station under investigation. For the purposes of this project, these corrections are denoted as source specific station corrections or SSSCs.

The predicted travel times for each station are represented as a sum of model-based travel times and empirical corrections. The model-based component is obtained by raytracing through an appropriate 3-D velocity model of the crust and upper mantle region surrounding the station. The algorithm which we selected to compute travel times in our complex 3-D velocity models is an extension of a finite difference approximation method originally developed by Podvin and Lecomte (PL, 1991). This algorithm is well suited to the present application to rapidly varying models of the crust and upper mantle in that it can properly treat velocity contrasts as great as 10:1 independent of the geometry of the feature. The empirical correction component of the predicted travel times is derived from calibration events observed at the IMS stations. Calibration events include ground truth (GT) events with known locations and origin times (GT0 events), as well as GT events with various degrees of uncertainty in their hypocentral coordinates (i.e. GT2, GT5, etc., where the GT level refers to the location uncertainty in km). Thus, the empirical correction is essentially an interpolation of the observed travel time residuals (with respect to our 3-D velocity model) for the calibration events, analogous to the empirical correction surfaces estimated by Schultz et al. (1998) and others for different sets of stations using Bayesian kriging and other comparable stochastic inversion procedures.

A key element of our approach has been the refinement of our initial 3-D velocity model through tomographic inversion analyses of relevant data sets, which have included the IMS station calibration data referenced above as well as supplemental data from the region under investigation. These supplemental data include arrival times from calibration events observed at non-IMS stations, arrival times from well-recorded earthquakes, and long-line refraction data, where available. The tomographic inversions have been carried out using a new algorithm developed for this project which is fully

nonlinear with respect to both the velocity model and event locations, as is required for obtaining accurate solutions in the structurally heterogeneous regional distance range. This algorithm has been implemented as an iterative nonlinear process, which combines grid search event location and conjugate gradient inversion methods. Within each iteration, travel times through the current 3-D model and associated sensitivities of travel times to cell slownesses are computed using our newly extended version of the PL algorithm. At each step in the iterative process the event locations are re-estimated for the current model using a grid search location technique developed by Rodi (2002), which explicitly accounts for the varying levels of GT data available for analysis. Following each event relocation step, the velocity model is updated using a linear conjugate gradients (LSQR) subject to appropriate smoothness constraints. This entire process is then iterated until the results converge to a final stable estimate of the 3-D velocity model which is most consistent with the available calibration data. It is this tomographically refined 3-D velocity model, together with associated empirical corrections, which has been used to predict our final estimates of the SSSCs for each of the Group 1 IMS stations, together with associated estimates of the uncertainties in those corrections.

1.3 SUMMARY OF MAIN RESULTS

As was noted above, this report documents the completion of a three year project. The main results from the studies conducted during the first two years of the effort have already been extensively documented in previous annual technical reports (Murphy, et al., 2001, 2002) and will only be briefly summarized here. Principal accomplishments achieved under this project are described in more detail in subsequent sections of this report, but may be briefly outlined as follows:

- A new 3-D velocity model of the entire Group 1 study region has been formulated which incorporates both P- and S-wave velocity distributions defined at resolutions ranging from 1/3 to 1 degree across the area of interest.
- A unique Soviet explosion ground truth database has been assembled and delivered to the SMR (formerly CMR) Research and Development Support Services (RDSS) data archive. This database consists of over 1000 carefully validated, regional

distance initial P-wave arrival time observations from Soviet PNE and weapons tests recorded at stations of the FSU permanent seismic network.

- A sophisticated, fully nonlinear tomographic inversion module has been formulated, implemented, and applied to the refinement of the upper mantle P-wave velocity distributions in the FSU, India/Pakistan, and China/Mongolia regions of our study area. Data used in these tomographic inversions have been collected into a uniform database and delivered to the RDSS at the SMR.
- Extensive testing of these tomographically refined P-wave velocity models against available data from ground truth events indicates that they are highly accurate with essentially zero bias and total RMS model errors on the order of 1 second across much of the Group 1 study area. This is to be compared with an average bias of - 3.65 seconds and RMS error of more than 2 seconds associated with the default IASPEI91 model in the FSU region.
- Comparison of regional seismic event location accuracies for a sample of 21 widely distributed Soviet PNE explosions using observations from 4-6 IMS or surrogate IMS stations indicate an average mislocation of 6.9 km when using the tomographically refined 3-D velocity model, as compared to an average mislocation of 20.4 km obtained for the same data set using the default IASPEI91 model. A similar analysis of data recorded at a subset of these same stations from a sample of 20 Novaya Zemlya explosions indicate an average mislocation of less than 10 km for the 3-D model, as opposed to an average mislocation value of 44 km obtained using the IASPEI91 model.
- Similar validation tests of the 3-D velocity model using data from ground truth events in the India/Pakistan and China/Mongolia regions indicate that it is also significantly superior to the default IASPEI91 model in those regions. A ground truth sample of arrival time data observed at stations of the Chinese National Network from Lop Nor explosions with well-constrained locations (i.e. GT1, GT2) and origin times has been collected to support these validation studies.
- A corresponding S-wave velocity model for the entire Group 1 study region has been derived from our final, tomographically refined P-wave model using Poisson's ratio relations determined from available P and S wave velocity data for

the crust and upper mantle across the area. Limited tests of this model have indicated that it is generally consistent with observed S-wave travel times in the region. However, it is now clear that the variance of the corrected S-wave travel times will be much larger than that for the corresponding P-wave times, even for a very good S-wave velocity model, which means that they will be significantly down-weighted in the location process.

- Empirical correction surfaces which account for travel time deviations that are not accounted for by the 3-D velocity model have been estimated using a newly developed, multistation kriging algorithm. This new algorithm represents an enhancement of the standard kriging algorithms in that it explicitly satisfies the physical constraints of the seismic reciprocity theorem. Application of these corrections to the model-based Soviet explosion ground truth travel time residuals results in reduced RMS errors on the order of 0.7 seconds. We consider this residual error to be close to the lower bound on the resolution of the total calibration process which we have implemented for this study.
- Final P and S wave SSSCs have been estimated for all 30 Group 1 IMS stations, as well as for 11 surrogate IMS station locations, out to 20 degrees from each station for 11 depths extending from the earth's surface down to 200 km. These SSSC estimates have been delivered to the RDSS at SMR.

1.4 REPORT ORGANIZATION

The report is divided into seven sections including these introductory remarks. Section 2 describes the methodology and the composition and refinement of the 3-D velocity model which form the bases for our travel time prediction methodology and calibration of the Group 1 study area. In Section 3 we describe the project efforts to validate the travel time predictions and to test refined velocity models for the study area. In Section 4 we discuss extension of this model-based approach to travel time calibration for secondary seismic phases in the Group 1 study area and additional issues arising from pick uncertainty for such signals. Section 5 describes examples of the SSSCs derived for the regional P- and S-wave travel times which have been derived for each of the Group 1 IMS stations and discusses the significance of their depth dependence. In Section 6 we

describe the empirical correction surfaces determined using the new reciprocal kriging methodology and the implications for location uncertainty. Finally, Section 7 summarizes our major results and conclusions and addresses issues for future seismic travel time calibration to improve event location. In addition, we include in an appendix plots of the surface-focus SSSCs for the regional P-wave travel times for each of the 30 IMS stations from the Group 1 study area.

SECTION 2

METHODOLOGY AND VELOCITY MODELS

2.1 TRAVEL TIME PREDICTIONS

Throughout this project we have utilized a model-based approach to predict travel times and determine SSSCs for the Group 1 IMS stations. We selected this approach because it provides the best utilization of available knowledge for use in regions where calibration data are sparse or non-existent. The essential elements of this approach are (1) velocity models extending out to regional distances (i.e. out to 20°) from each of the IMS seismic stations of interest, and (2) methods of tracing ray paths and computing travel times through the models for the seismic phases useful for event location. For the former we have used prior knowledge to construct a three-dimensional velocity model covering the entire Group 1 study region, and we have used available ground truth information to refine the model through an inversion process. Seismic ray paths through the model and the associated travel times are calculated using a sophisticated ray-tracing algorithm, which is capable of handling transmission through the complex 3-D structures. The latter travel time calculation methods are used initially for determining the residuals forming the basis for model refinements within the tomographic inversion process and also for producing the travel times at each Group 1 IMS station from the regional hypocenters calculated from the final 3-D velocity model for eastern Asia, which ultimately determine the SSSCs.

Our step-by-step approach to the calibration problem can be summarized as follows:

(1) Formulate an initial 3-D velocity model for the Group 1 station study area.

(2) Ray trace through the initial model to determine travel times and define preliminary SSSCs with respect to the IDC default IASPEI91 model for each of the Group 1 stations.

(3) Determine source-specific empirical travel time corrections for each station and phase by interpolating between observed calibration event travel time residuals relative to the 3-D model.

(4) Generate a 3-D travel-time table for each Group 1 IMS station and phase by summing:

- Model based travel times from 3-D ray tracing through the refined model and
- Empirical travel time corrections.

(5) Compute revised SSSCs by subtracting IASPEI91 travel times from the resulting 3-D travel time tables as a function of the hypothetical source hypocenters surrounding each station.

(6) Perform joint tomography and multiple event location to update and refine the velocity model and relocate events.

(7) Perform validation testing of the refined 3-D velocity models and station corrections through relocation analyses of ground truth events.

(8) Iterate process to incorporate additional calibration events or model changes, as they become available.

The method used to compute travel times in the complex 3-D velocity models is based on a finite difference approximation to the eikonal equation developed by Podvin and Lecomte (1991) and implemented by Lomax (1999). To determine the values of the travel time functions, T_i, we evaluate $T_i(x; m)$ for a fixed hypocenter by interpolating a travel time table stored on a 3-D hypocenter grid. T_i is a function that predicts the travel time to station i from an event hypocenter x_j. This function depends on the model parameter vector m. The 3-D hypocenter grid is created by applying the Podvin and Lecomte (PL) algorithm to the earth model defined by m, using the ith station as the "source" in the calculation. The PL algorithm can accurately model different propagation modes, such as transmitted and diffracted body waves or head waves. The algorithm is well suited to the present application in that it can properly treat velocity contrasts as great as 10:1, independent of the geometry of the feature. Thus, this approach represents a significant improvement over similar method (e.g. Vidale, 1988, 1990; Moser, 1991), which can encounter serious difficulties in the presence of sharp first-order contrasts.

For use in the PL algorithm, the model is discretized on an equally spaced grid comprised of constant velocity cells. The PL algorithm is used to compute travel times from each station to every surrounding grid point. That is, the "source" is placed at the station location and, using reciprocity, each node of the 3-D grid is then the hypocenter of an event. The resulting grids, one for each phase and station, embody a set of 3-D travel

time tables that can be used for calculating the corresponding SSSCs. Multiple arrivals (transmitted, diffracted, and head waves) are calculated at each grid node and the first arrival time is identified. The time t at the current node is a function of the times t_n at some (3 or fewer) of the neighboring nodes and the slowness, s, in the cell traversed by the wavefront to reach this node. That is, $t = t(t_n, s)$. This method of travel time computation produces a full grid of travel times considerably faster than two-point ray tracing, and the sources and receivers can be located anywhere within the model. The PL computations are output in the form of 3-D travel-time tables, one for each station and seismic phase, which then can be used by a grid-search event location algorithm in lieu of global travel time tables, such as IASPEI91. The accuracy of the PL raytracing algorithm with respect to the present application has been tested in a variety of ways; and it has been concluded that, when run with grid spacings on the order of 5 km, it can be expected to provide 3-D travel time estimates with accuracies of better than 0.25 seconds out to the 2000 km distance range of interest in this calibration study.

The PL algorithm has also been extended to compute the sensitivities of travel times to cell velocities, which are required as part of the model inversion process. To calculate the ray path, we save the node pattern ("stencil") at each step through the model as we perform the normal PL forward travel time calculation to predict arrival times. This stencil indicates which of the neighboring nodes were used to calculate the minimum time at the current node. The stencils can be used to reconstruct a path from any node of the grid to the source. The ray tracing is accomplished by identifying all of the grid nodes and the cells (slownesses) that contribute to the calculation of the time at the receiver. As the wavefront propagates away from the source, more nodes (and cells) are involved in the travel time calculation at each step. After the midpoint of the ray path, the propagation region narrows until it reaches the single node at the source location. The sensitivity of the travel time to the slowness, dt/ds, is calculated at each grid node of the "ray" for the last cell traversed by the wavefront to reach that node. The weight of each neighboring node in the calculation of the time at the current node (dt/dt_n) determines the weight of the subsequent node-to-source subpath in the total travel time

calculation for the ray. The sensitivities along each subpath are then weighted by this term.

This is illustrated in Figure 2-1 which shows the sensitivities of the travel times calculated by PL to cell slownesses for paths originating at station DSH in Tajikistan. After the sensitivities are calculated for multiple station-centered Cartesian grids, they are then mapped to a single geographic grid. Following this procedure the Pn sensitivities are extracted to form the kernel matrix for the tomographic inversion used in refining the velocity model. The ray tracing algorithm and sensitivity calculation were tested for

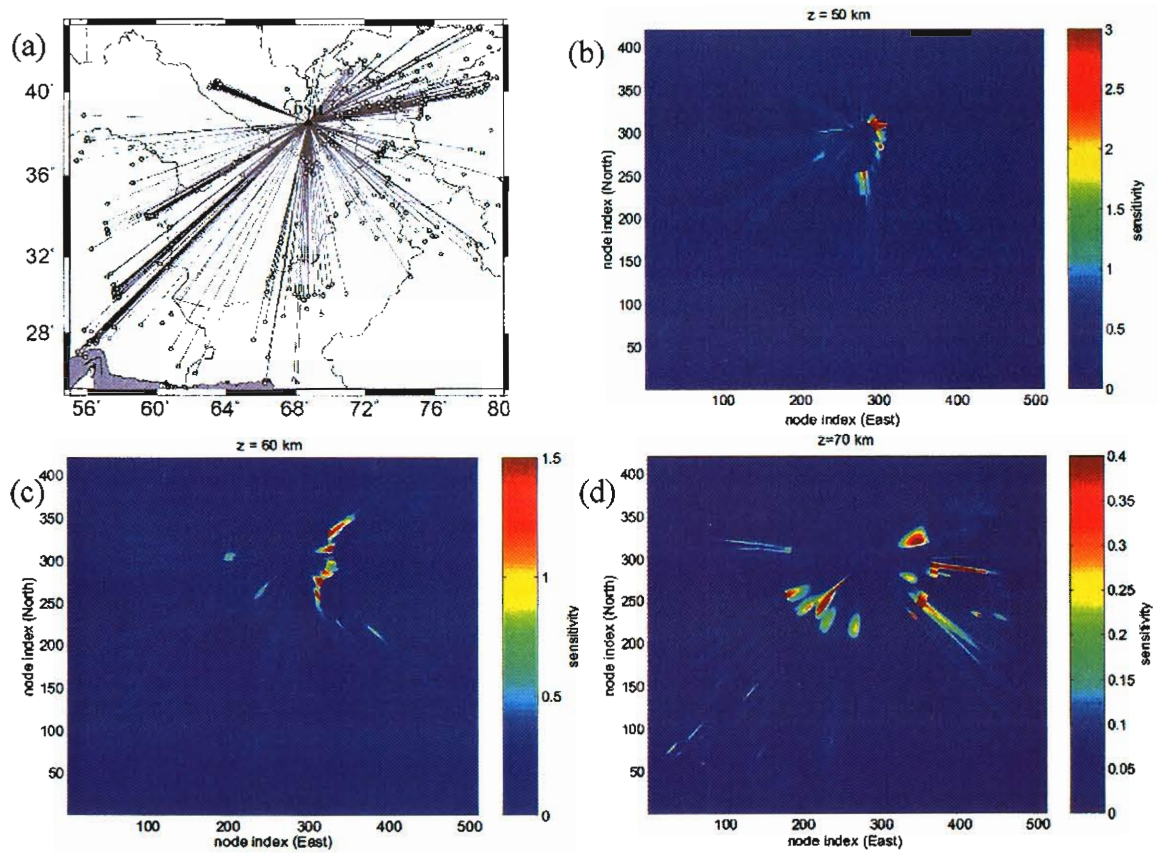

Figure 2-1. Ray path sensitivities calculated using the extended PL algorithm. (a) Station DSH and events for which sensitivities were calculated shown with straight line approximations of the ray paths. (b), (c), and (d) Sensitivities for 50 km, 60 km and 70 km depth slices calculated for station DSH and events shown in panel (a). Note that the sensitivities are unitless. The sensitivities for all rays that encounter a cell are summed, producing scales that can range from zero upward. Deeper slices through the sensitivity matrix naturally have smaller scale ranges, since the rays spread out as they propagate away from the station.

precision by comparing the travel time computed as the sum of the weighted sensitivity-slowness products to the forward PL calculated times. For rays with 10^5 nodes, the difference between travel times calculated by these two methods is on the order of 10^{-2} seconds, when the calculation is done in single precision. This error is accounted for by the level of precision in the calculation, demonstrating that the ray tracing technique is accurately tracing the minimum time PL ray path.

The PL algorithm performs completely 3-D travel time and ray tracing calculations. It is important to make a distinction between 3-D and pseudo 3-D or "2.5-D" methods, where rays are traced through 2-D slices of a 3-D model. We illustrate the difference between rays calculated using a fully 3-D method and a 2.5-D method in an example of Figure 2-2. The 3-D ray shows out-of-plane effects not accounted for by the 2-D ray and a difference of 5 km in the turning depth. These differences arise because the 3-D ray traverses the fastest path between the source and receiver, which may or may not be in-plane; while the 2-D ray is constrained to in-plane propagation. Consequently, the travel

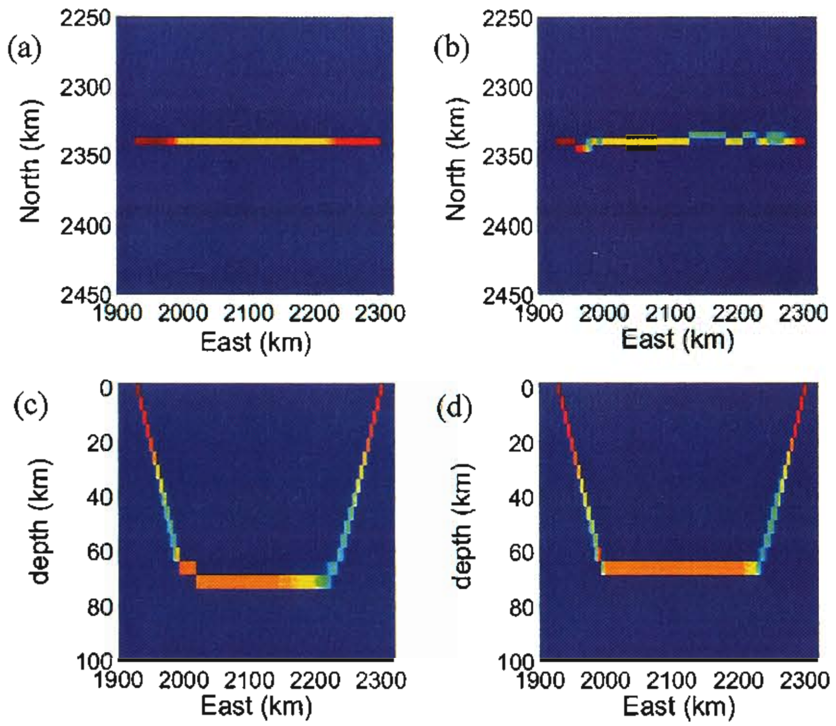

Figure 2-2. 2-D vs. 3-D ray paths. Map view plots showing the 2-D raypath (a) and the 3-D raypath (b). Depth vs. longitude plots of the 2-D raypath (c) and the 3-D raypath (d). Travel times computed by each method differ by 0.3 sec. In addition to the out of plane effects seen in the 3-D ray, the turning depths of the two rays differ by about 5 km.

time of the ray calculated by the 3-D method is 0.3 seconds faster than the travel time for the 2-D ray. The discrepancy in travel time calculations between the 3-D and the 2-D methods could be much greater for even longer ray paths. We note that this example is for a ray with a source-station distance of 400 km, and our regional calibration studies include calculations extending to 20°, or over 2000 km in distance, where significantly greater differences could be expected between the fully 3-D approach and the simplified models.

2.2 EVENT LOCATION

As noted above, we incorporate calibration data into our travel time calculations and velocity model refinement in the form of ground truth (GT) events. A fundamental element in utilization of such GT data is event location. We locate events using the grid search method GMEL (Grid-Search Multiple Event Location) developed by Rodi and Toksöz (2002). This method is a grid search technique that allows for both Gaussian and non-Gaussian error distributions. GMEL also allows us to incorporate GT data of varying levels, constraining hypocenter solutions based on the accuracy of event origins within the GT database. Because GMEL offers the option of performing multiple event locations instead of traditional single event locations, we are able to use the calibration data to simultaneously solve for a set of travel time corrections at each station. We do this in a final relocation of events subsequent to our tomographic inversions in order to account for any deficiencies in the crustal part of our models that are not updated in the tomographic velocity model refinements.

2.3 VELOCITY MODELS

2.3.1 MODEL PARAMETERIZATION AND STARTING MODELS

We have defined a Unified Model Parameterization (UMP) that consists of a velocity-versus-depth profile at each point on a geographic grid, sampled uniformly in latitude and longitude. These profiles are divided into geological units such as water, sediment layers, crustal layers, and mantle layers that allow us to preserve velocity discontinuities without over parameterizing the model. At each geographic grid-point, the velocity profile is given as velocity/depth pairs at nodes ranging from sea level to a depth of 760 km. The velocity varies within each layer as a smooth gradient. Discontinuities in velocity are

allowed at the ocean bottom, Moho and the major mantle discontinuities (410 and 660 km depth). This parameterization reduces the number of model parameters to be solved for in the inversion.

Models of differing parameterization and spatial resolutions are integrated, according to a specified hierarchy, and converted to the UMP by a software module denoted as QUILT. Our overall 3-D velocity model includes seven submodels covering virtually all the Group 1 region landmass, plus a background 3-D model based on surface-wave inversion analysis (cf. Stevens et al., 2001). The composite is illustrated in Figure 2-3. We described the bases for the various submodels which make-up the UMP composite in prior annual reports (cf. Murphy et al., 2001, 2002). In defining these velocity submodels, we have drawn upon different knowledge bases depending on the levels of information available from the different areas and utilizing calibration data to update the model, in areas where that is appropriate. The initial P-wave velocity model included

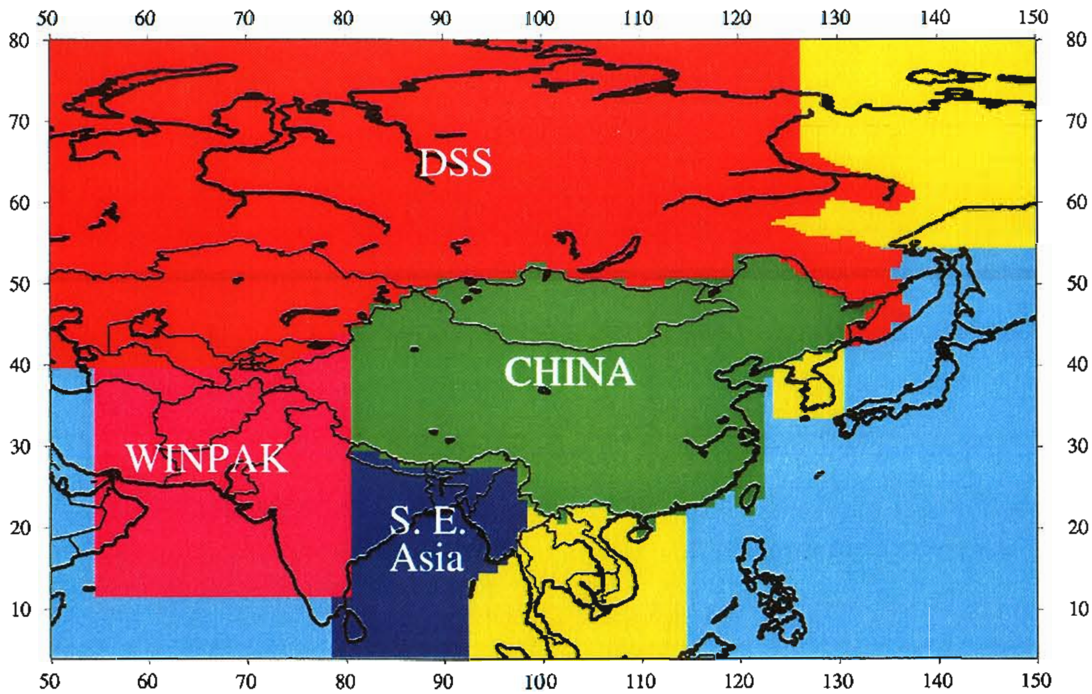

Figure 2-3. Map outlines of our composite 3-D velocity model for the Group 1 study area. Each of the submodels has been defined using the best available reference data for that region. The global background model (denoted by the light blue color) is the 1°-x-1° surface wave model of Stevens et al. (2001). Yellow denotes regions where the upper mantle model of Stevens et al. has been replaced by the IASPEI91 upper mantle model to be consistent with local travel time observations.

prior knowledge based on (1) Deep Seismic Sounding results analyzed by the IDG from the FSU, (2) a new China model developed by Toksöz and colleagues at MIT using a Monte Carlo inversion of earthquake travel times, (3) a model for the India-Pakistan region derived from published models and subsequently refined through tomography, (4) a new southeast Asia model based on previously published models, (5) models for Thailand, the Korean peninsula, and far eastern Russia based on surface wave studies modified by regional P wave travel time observations, and (6) a general 1°-x-1° background model based on recent surface wave studies by Stevens and Adams (2001). Contributions from the various models are assigned priorities and composed into the general 3-D velocity model covering the entire Group 1 study region using the QUILT computer software module. The UMP grids are generated with 0.5° spacing in latitude. Longitude spacing is 0.75° for the DSS and Russian tomography regions, while it is 0.5° for the WINPAK3D and China tomography regions. This selection of longitude grid spacing accounts for the decreasing aspect ratio of longitude versus latitude in regions which approach the North Pole. Longitude spacing for the WINPAK3D and China UMP grids is defined to be equal to the latitude spacing, since the aspect ratio of longitude versus latitude is more constant over the latitude ranges for these model regions.

One complication in using this geographically-defined velocity model is that our current implementation of the Podvin-Lecomte algorithm solves the eikonal equation in Cartesian coordinates for a flat-earth model. To address this issue, we have developed the algorithms for accurately mapping from UMP to Cartesian coordinates (software module XPLMOD) as required by our ray tracing algorithm and for mapping the 3-D Cartesian travel time grids and related ray path sensitivities back to geographic grids (software module XPLTAB) for use in the inversion. In mapping from geographic to Cartesian coordinates, earth-flattening transformations are performed on depth and velocity within the model. A mapping transformation is carried out for each IMS station to produce station-centered grids. This preserves distances and azimuths between all possible source locations and the station, minimizing mapping errors. We use bi-cubic interpolation to convert the UMP models into uniformly sampled Cartesian grids. Both

the depths to layer interfaces and the layer velocities are interpolated, preserving the integrity of geologic layers.

The sampling of the Cartesian grids is constrained by limitations of the finite-difference Podvin-Lecomte method. The Podvin-Lecomte method uses a plane wave approximation which is inaccurate in the source region; therefore, the Cartesian grids must be generated on very finely spaced grids to minimize travel time error in this region. Uniformly sampled 5-x-5-x-5 km spaced grids result in a maximum calculation error of 0.5 seconds due to the plane wave approximation. Using an enhanced version of the Podvin-Lecomte travel time algorithm that implements a multigridding technique, we are able to reduce error in travel time computation to less than 0.25 seconds at regional distances for models with grid spacing of 5 km.

2.3.2 MODEL REFINEMENTS

A state-of-the-art joint velocity tomography and event relocation algorithm has been developed to generate more accurate velocity models in geologically complex regions. Applying this algorithm, we have generated a set of tomographically updated models for calibration of the Group 1 IMS stations in three areas: (a) the India-Pakistan region, (b) China, Mongolia, and surrounding regions, and (c) two regions in Russia, one surrounding station BRVK and the adjacent area to the east.

In this procedure a data set of regional seismic events is used to iteratively update the velocity model following a conjugate gradients technique that adjusts the velocity model to minimize the misfit between the calculated and observed travel times from multiple stations and events, subject to smoothness constraints. The travel times and their sensitivities to the 3-D velocity structure are computed with an extension of the Podvin-Lecomte (1991) method. Earthquake locations are often not known precisely; therefore, we also relocate events using a 3-D grid search location method (Rodi and Toksöz, 2002) after each update of the 3-D velocity model. This process of inversion is fully nonlinear with respect to both velocity and event location. However, when sufficient prior data exists to constrain one set of parameters or the other, we can decouple the location and

velocity imaging problems. For example, we can constrain the hypocenters of Peaceful Nuclear Explosions to their known locations.

Figure 2-4 is a simple flowchart of the tomography algorithm used to develop the new 3-D velocity model refinements for the India-Pakistan, China-Mongolia, and Russian regions. There are three major components involved in this joint tomography/location procedure: (1) 3-D ray tracing to predict first arrival times using an enhanced version of the Podvin-Lecomte (PL) method (1991); (2) a 3-D grid search location algorithm (GMEL) by Rodi and Toksöz (2002) to relocate events inside the appropriate velocity model; and (3) a linear conjugate gradient inversion algorithm to produce the updated velocity model inside each iteration of the overall nonlinear algorithm. In the next few subsections, we describe the tomographic velocity model refinements which make-up the new 3-D velocity model for the Group 1 region.

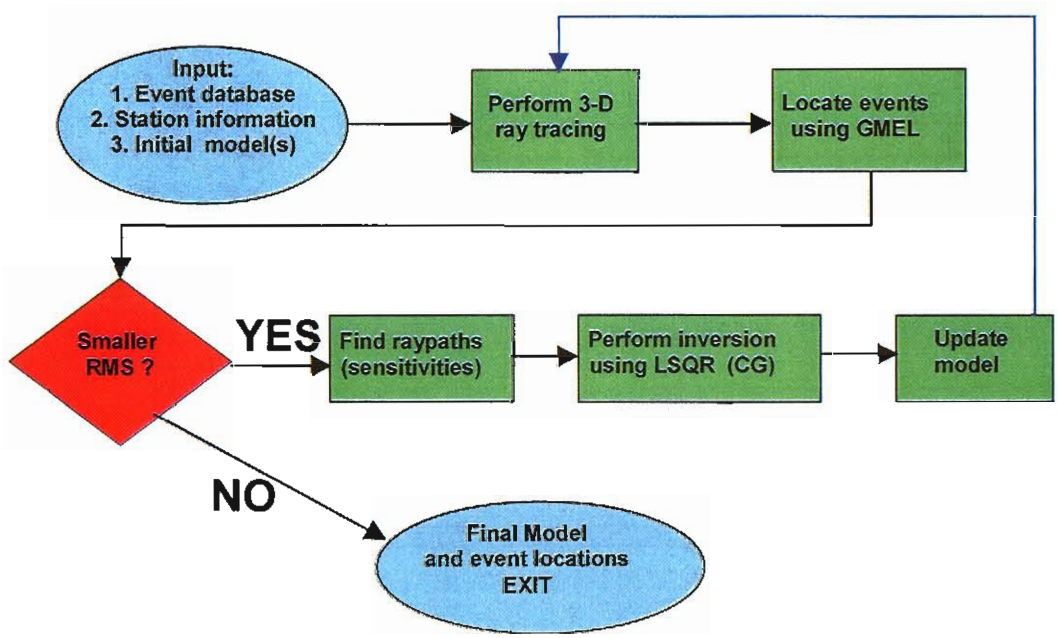

Figure 2-4. Simplified flowchart of the nonlinear joint tomography and location procedure used to develop 3-D models of regions in Eastern Asia for the calibration of Group 1 IMS stations.

In the preceding subsections, we described the 3-D raytracing using the PL algorithm and utilization of the GMEL for relocating events within the region covered by the model. Once the database of events has been relocated and the ray path sensitivities have been calculated, we perform a linear conjugate gradients inversion for an optimized update to the velocity model. We use a version of the LSQR algorithm (cf. Nolet, 1983; Paige and Saunders, 1982) to produce this update. The LSQR algorithm is a linear conjugate gradient method used to iteratively solve large systems of sparse, linear equations. The output of the algorithm is a vector of changes to the input velocity model. The model update produced by LSQR is constrained in several ways. First, we fix a small buffer region along the model region perimeter to the values of the initial model. This is to prevent large velocity variations from occurring in areas of the model that are poorly constrained by data and to allow us to seamlessly integrate our final models into other global models. Second, we apply a smoothing operator to the model using a second differencing operator, which is equivalent to ensuring the curvature of the model is smooth (Twomey, 1977). Finally, we apply a scalar damping parameter to the model to balance the sharpness or noisiness with the horizontal spread or smoothness of the recovered velocity contrasts. After the linear conjugate gradient method has converged to an optimized update to the model, we use the model change vector as a search direction in the next iteration of the nonlinear conjugate gradient inversion.

Thus, our inversion algorithm jointly solves the nonlinear problem, iterating over linear inversion steps that include updates of the hypocenters, velocities and ray paths. This technique explicitly addresses the coupling between the hypocenters and the velocity structure by computationally breaking down the large matrix that must be inverted for velocities and locations. This computational technique results in two separate smaller matrices which may be inverted separately, but still solve the simultaneous problem (cf. Spencer and Gubbins, 1980; Rodi et al., 1981).

Although we are currently only solving for Pn velocity in the inversion, model updates extend beyond Pn velocity. Based on the updated Pn velocity, velocities from the Moho to 410 km are refined in a smooth manner as shown in Figure 2-5. A constant shift in

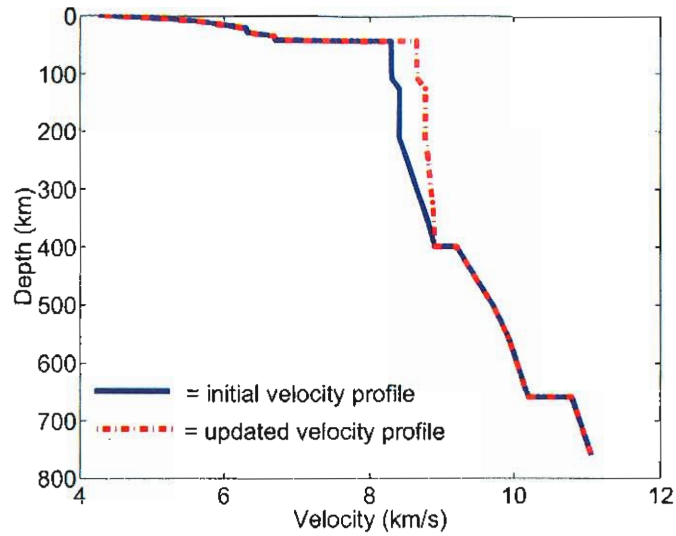

Figure 2-5. While we only invert for the Pn velocity, the velocity profile is smoothly updated from the Moho to 410 km based on the updated Pn velocity.

velocity is applied from the Moho extending to 210 km depth. Tapering between 210 km and 410 km depth insures a smooth transition down to the 410 km discontinuity.

Application to the India-Pakistan Region

We first look at tomography applied in the India-Pakistan region using a set of earthquake data. The **W**eston Geophysical **In**dia-**Pak**istan **3-D** velocity model (WINPAK3D), a detailed 3-D velocity model synthesized from numerous previous studies, was used as an initial model. The references utilized to develop the initial WINPAK3D model included data such as seismic reflection and refraction surveys (i.e. DSS profiles, Pn tomography, Pnl waveform inversion), interpretations of gravity data, surface wave studies, and receiver function analyses. The velocity model is defined on a grid of one-degree by one-degree blocks and 5 km depth intervals from 0 to 75 km. The IASPEI91 model (Kennett and Engdahl, 1991) is appended to the base of the preliminary velocity model, beginning at 80 km depth and extending into the mantle, to accommodate ray paths that travel into the upper mantle. Some preliminary validation was performed on the initial model to verify its suitability and potential to improve event locations. See Johnson and Vincent (2002) for details on the development and validation of this initial WINPAK3D model. Previously, the eastern boundary of the India-Pakistan model, at

80° longitude, encompassed only central and western India. Recently, Weston Geophysical extended the bounds of the WINPAK3D region to incorporate all of India and performed joint velocity and hypocenter relocation tomography on the new model, solving for revised upper mantle velocities. This work was completed under the auspices of the Defense Threat Reduction Agency contract number DTRA01-00-C-0098.

The data set for the inversion is made up of a larger, more accurate database of events than was used in the initial WINPAK3D inversion. Events were selected from an updated version of the Engdahl et al. (1998) database (EHB) of well-located earthquakes and explosions that we obtained in February 2002. The EHB data set is generally considered to be GT15 or better in continental areas, according to the IASPEI Working Group on Reference Events (http://lemond.colorado.edu/~copgte/). To ensure that the most accurate data subset was used in the inversion, only events that had a secondary station azimuth gap (largest azimuthal gap closed by one station) of <130° were selected from the EHB data set. Based on relocated explosion studies, 95% of the events will be mislocated by no worse than 15 km (Engdahl, 2002). Additionally, data outliers with residuals of greater than ± 7 sec were omitted. This threshold was chosen because residuals of 5 seconds or greater can be attributed to structure in tectonically complicated regions such as the Hindu Kush (cf. Murphy et al., 1998). We chose a distance cut-off of 14° in order to filter out rays bottoming deeper than the upper mantle. We also restricted event depths to the crust and upper mantle, with a maximum depth of 60 km. Final selection was focused on obtaining optimal spatial distribution across the region, both in latitude/longitude and depth. The events in the data set were recorded at 89 stations within our model region, and consisted of over 22,500 arrivals for 1,337 events that were used in the joint inversion. This data set is shown in Figure 2-6a.

To ensure that the tomography algorithm was functioning properly and to provide a test of the resolution of our data set for the India-Pakistan region, we performed a "checkerboard" inversion test using the subset of the EHB database (Figure 2-6a). For the resolution test, we perturbed the Pn velocity of an IASPEI91 1-D model, imposing a 3° by 3° checkerboard pattern of alternating high (viz. 8.3 km/sec) and low

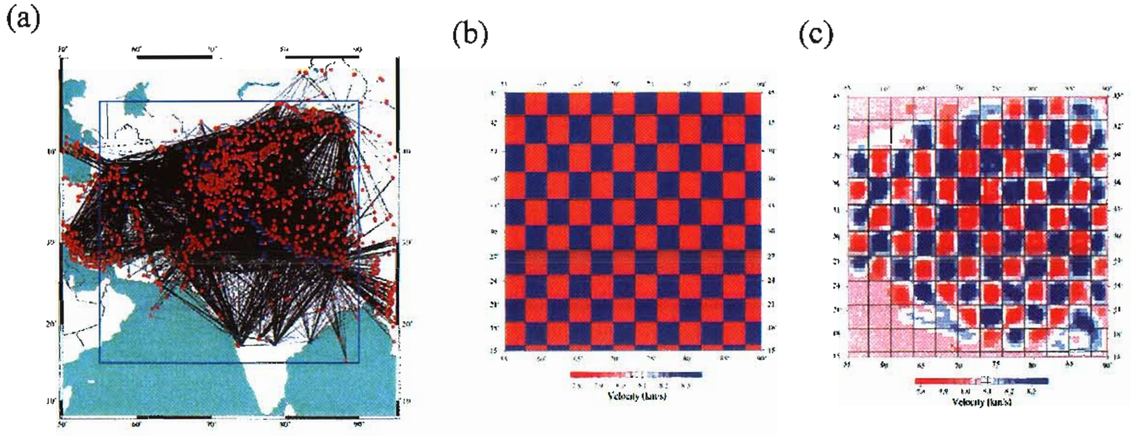

Figure 2-6. Results from a checkerboard resolution test of the earthquake data set used to update the WINPAK3D model. a) Ray coverage (straight line approximations) of the earthquake data set used to produce a tomographic update to the Pn velocity over the model region. The blue box indicates the region that was inverted for revised upper mantle velocities. b) The model we used to predict synthetic travel times from events to stations in our data set. c) The checkerboard pattern resolved by one iteration of the nonlinear inversion method. Across the majority of the inverted region, the resolution of the individual checkers is excellent. Less well-resolved regions to the south-southeast reflect the reduced data coverage, while poorly resolved areas in the far northwest and southwest reflect sheer lack of data.

(viz. 7.9 km/sec) velocities (cf. Figure 2-6b). Inversion was performed using synthetic arrival times calculated through the perturbed IASPEI91 model, while the unmodified IASPEI91 model (Pn velocity of 8.04 km/s) served as the starting model. We performed one iteration of our nonlinear conjugate gradient scheme to retrieve an estimate of the resolving capability of our data set. The damping parameter was chosen to reduce the RMS error while keeping the noise (one-node variations) low. The damping parameter chosen also preserves the amplitude of the velocity variations of the synthetic model. Figure 2-6c shows that the checkerboard pattern Pn velocity was successfully recovered in the inversion with especially good results in the central areas having very dense ray coverage. These results indicate both that our tomography algorithm is performing well and that the set of earthquake data selected to update the WINPAK3D model is providing high resolution across much of the region.

After the checkerboard resolution test, we performed several iterations of our nonlinear inversion technique to update the Pn velocity map extracted from our initial model. We inverted for Pn velocity as a function of latitude and longitude and then imposed a fixed rule for extrapolating this velocity into the upper mantle. Tomography was applied to the initial WINPAK3D model using the arrivals shown in Figure 2-6a. The event hypocenters were constrained to the EHB locations, since the starting locations were known to be very accurate based on the event selection criteria. The damping parameter for the inversions was again chosen to reduce the RMS while keeping the noisiness of the recovered velocity change low. Figure 2-7a shows the initial Pn map. The final Pn model is presented in Figure 2-7b. The general distribution of high and low velocities in the final model is similar to the starting model, but contains more detail. The RMS travel-time error of the tomography data set was 1.70 sec for the updated model, compared to 2.28 sec for the IASPEI91 model.

(a) (b)

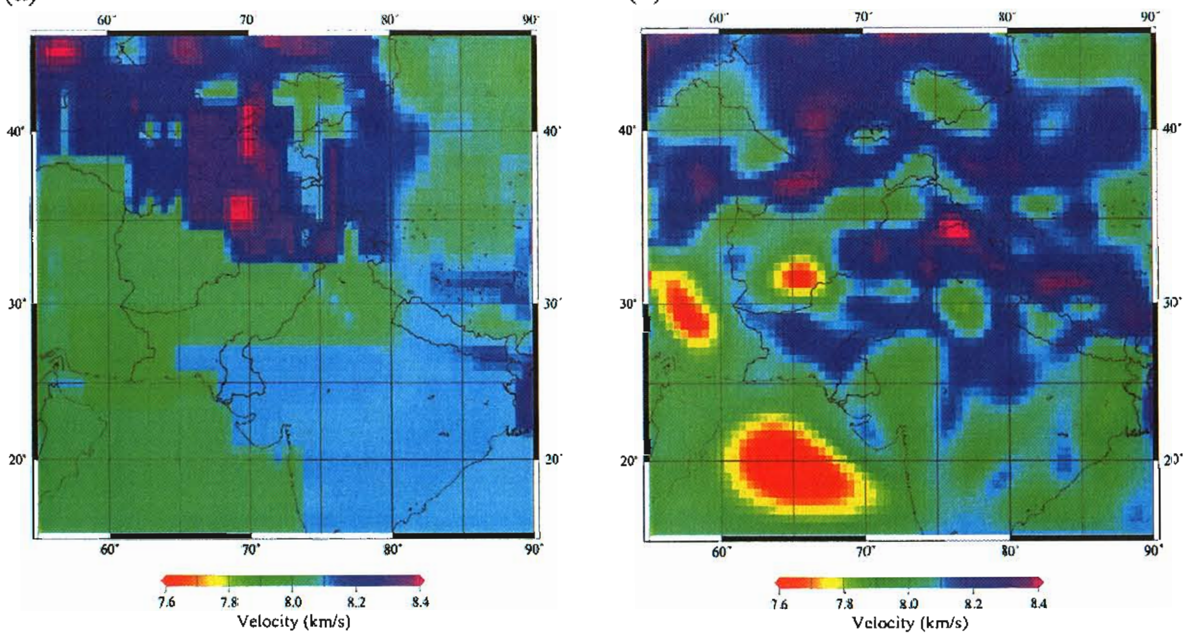

Figure 2-7. Initial (a) and final (b) Pn velocity maps from the WINPAK3D model resulting from application of our tomography scheme.

Application to the China Region

The preliminary model for the China inversion was developed at M.I.T. (Toksöz et al., 2003) as a composite of 1D models defined on a latitude-longitude grid, with the model at each grid point being obtained by Monte Carlo inversion of P-wave travel-times from rays lying within a 10-degree square region centered on its grid point. Development of the initial China model was described in detail in our prior annual report. We updated this model using a subset of earthquake data selected from the Annual Bulletin of Chinese Earthquakes (ABCE) that were chosen to ensure a reliable data set and optimum coverage for tomographic inversion. The criteria for event selection were similar to those used for the WINPAK3D database. Data outliers with residuals of greater than ± 7 sec were omitted. We again chose a distance cut-off of 14° in order to filter out rays bottoming deeper than the upper mantle. We also restricted event depths to the crust and upper mantle, with a maximum depth of 60 km. The resulting database included over 64,000 arrivals from nearly 10,000 events recorded at 88 stations in and around China (Figure 2-8).

We inverted for Pn velocity as a function of latitude and longitude and extrapolated this velocity into the upper mantle as described previously. Tomography was applied to the initial China model using the arrivals shown in Figure 2-8. In this case, we performed hypocenter relocation as part of the tomographic inversion procedure. Events were relocated with varying constraints relative to the initial locations provided in the ABCE bulletin. The new hypocenter solutions were constrained to be within a maximum of 15 km from the starting location, in epicenter and in depth. The revised model and event locations reduced the root mean square (RMS) travel-time residuals as compared with the global 1-D IASPEI91 model from 2.84 sec to 1.55 sec. The initial velocity model (Figure 2-9a) is less variable in velocity compared with the updated Pn model (Figure 2-9b). The inverted model also appears to resolve model details with higher resolution.

Application to the Former Soviet Union

We have described the tomographic inversion procedures applied to areas of the FSU with good groundtruth data in prior annual reports. In particular, tomographic analyses similar to those for the WINPAK region were applied to the FSU region around IMS

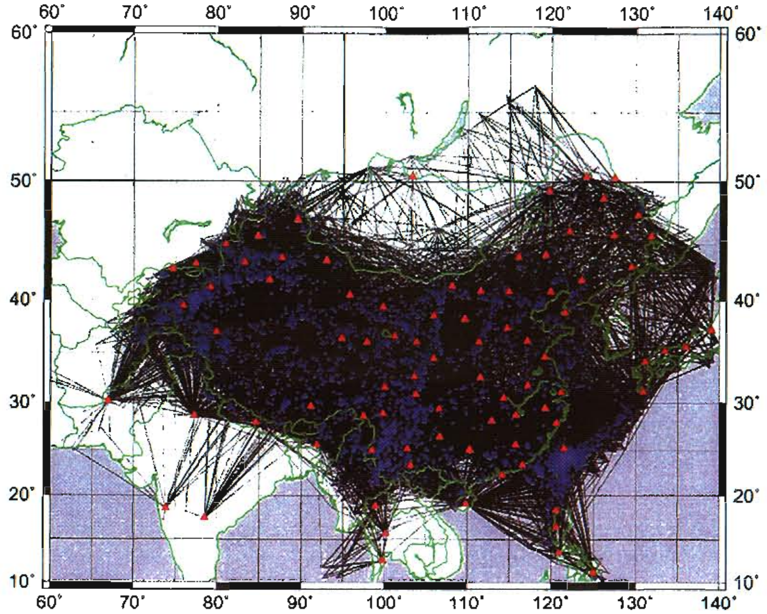

Figure 2-8. Ray coverage (straight line approximations) of the earthquake data set used to produce a tomographic update to the Pn velocity over the China model region.

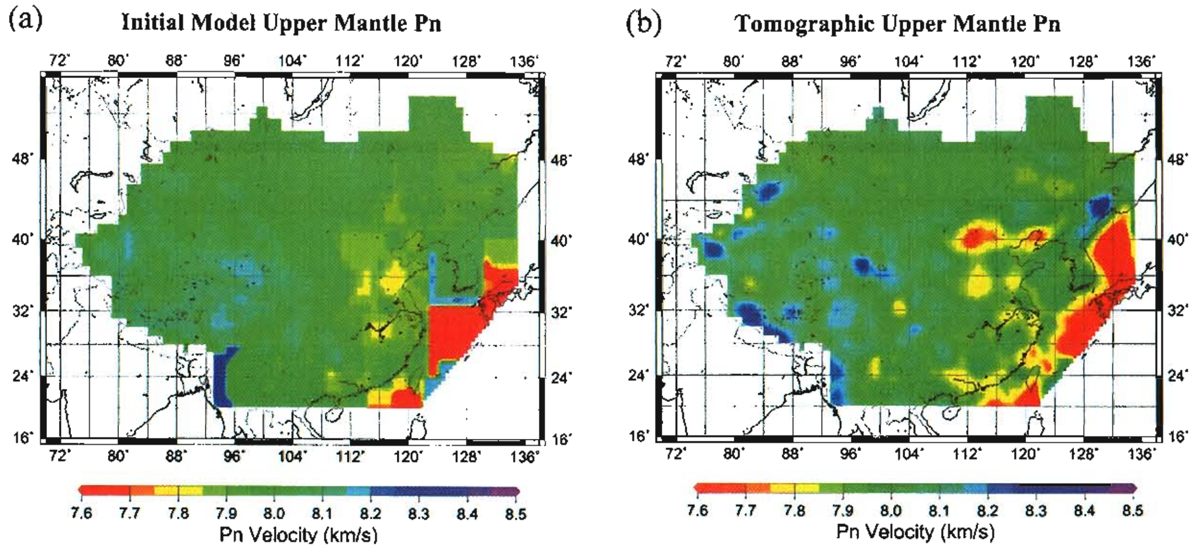

Figure 2-9. Initial (a) and final (b) Pn velocity maps for the China region. The final Pn velocity model results from our nonlinear tomography scheme.

station BRV and the adjacent region to the east in Russia. For these analyses we used data from PNE explosions throughout the FSU plus additional data from nuclear tests at the Semipalatinsk and Novaya Zemlya test sites. These explosions were recorded at BRV and other stations of the FSU permanent seismic network, including several with locations at or near IMS station sites. For the Borovoye station the explosion data were supplemented with about 300 precise arrival time observations at BRVK from Soviet bulletin earthquakes, located primarily along the active seismic zones to the south and east. Figure 2-10 illustrates travel paths and ray coverage used in the tomographic inversion for the region around BRVK for FSU nuclear explosions and the supplemental earthquakes. So, over much of this FSU region we have very accurate travel times and good station coverage from the PNE database which enables very good resolution for the tomographic inversion.

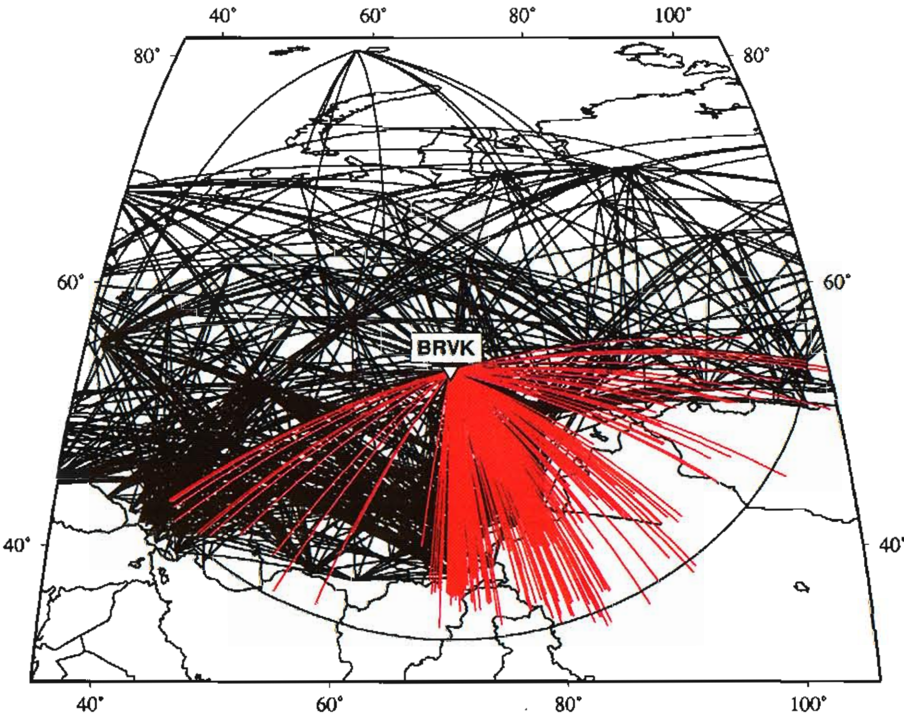

Figure 2-10. Ray coverage for the Borovoye DSS tomography inversion provided by Soviet PNE events (in black) and Soviet bulletin earthquakes (in red) recorded at stations of the Soviet permanent seismic network.

As with the other two subareas, we found that the tomographically revised models for the FSU regions produced reductions in the travel-time errors relative to IASPEI91. The RMS travel-time error for the Soviet PNEs from the tomography data set was 1.1 sec for the updated model, compared to 3.1 sec for the IASPEI91 model. Results of the tomographic analyses, including the FSU, WINPAK, and China region are shown in Figure 2-11. We show here the Pn velocities for the tomographically refined models covering much of our Group 1 region. Focusing on the FSU region, we find some apparent correlations of the tomography model results with published crust and upper mantle characteristics in the region. For example, two lower velocity features to the north correlate remarkably well with regions of crustal thinning associated with the NE Volga-Ural Uplift (to the west) and the crest of the West Siberian Platform (to the east). Similarly, a prominent low velocity zone in eastern China correlates with the Yin Shan Uplift. So, it appears that the tomographic analyses are generally giving reasonable results.

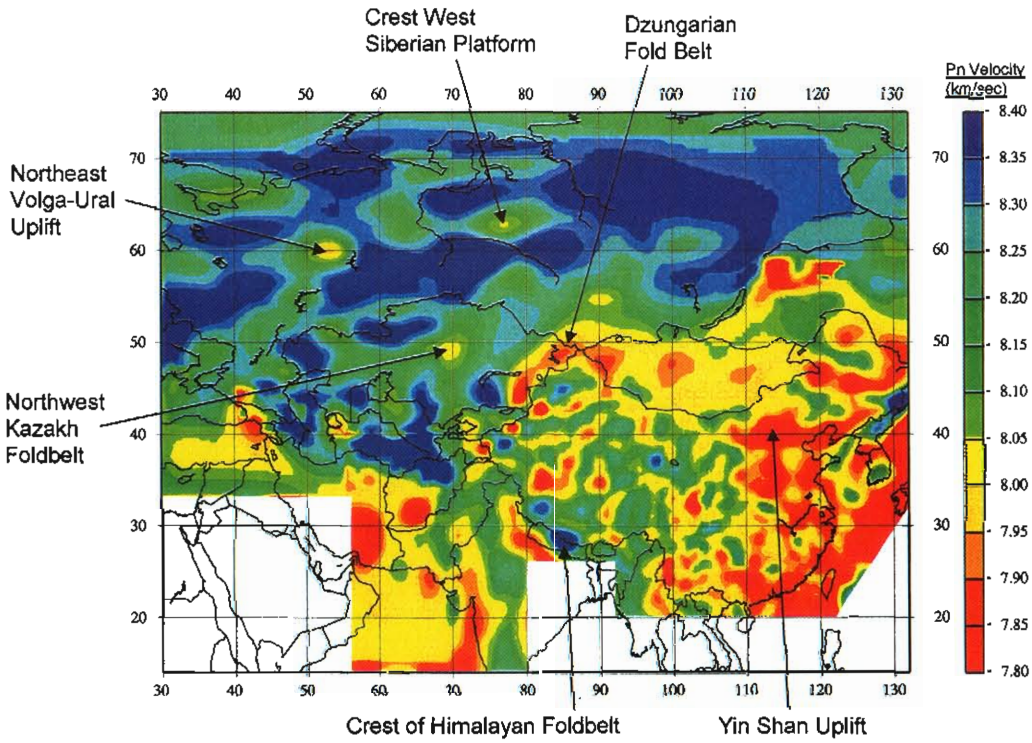

Figure 2-11. Map of the Pn lid velocity corresponding to the tomographically refined areas within the Group 1 study region (viz. DSS area of the FSU, WINPAK area of India/Pakistan, and the China/Mongolia area).

SECTION 3

TRAVEL TIME PREDICTION VALIDATION

3.1 FORMER SOVIET UNION VALIDATION

Our validation analyses of the velocity models for the FSU have been described extensively in prior annual reports; we show in this section some of the highlights of those prior reports as well as some additional recent developments. Figure 3-1 shows a comparison of the P-wave travel-time residuals for 55 FSU PNEs measured at the Borovoye station (BRV) relative to the nominal IASPEI91 travel times (left) and relative to our 3-D velocity model (right). It is apparent from the left-hand figure that the observed travel times are much faster than IASPEI91 for most of the events, as evidenced by the large negative residuals. On the other hand, for our 3-D regional velocity model the travel time residuals are significantly reduced and are more random geographically.

Figure 3-2 shows the same residuals at BRV plotted as a function of event distance for the FSU PNEs. The average residual relative to IASPEI91 travel times is – 3.5 seconds compared to average residuals of only 0.06 seconds for the 3-D model. Furthermore, there is also a significant reduction in the scatter of the data from $\sigma = 2.26$ seconds for IASPEI91 to $\sigma = 0.96$ seconds for the 3-D model.

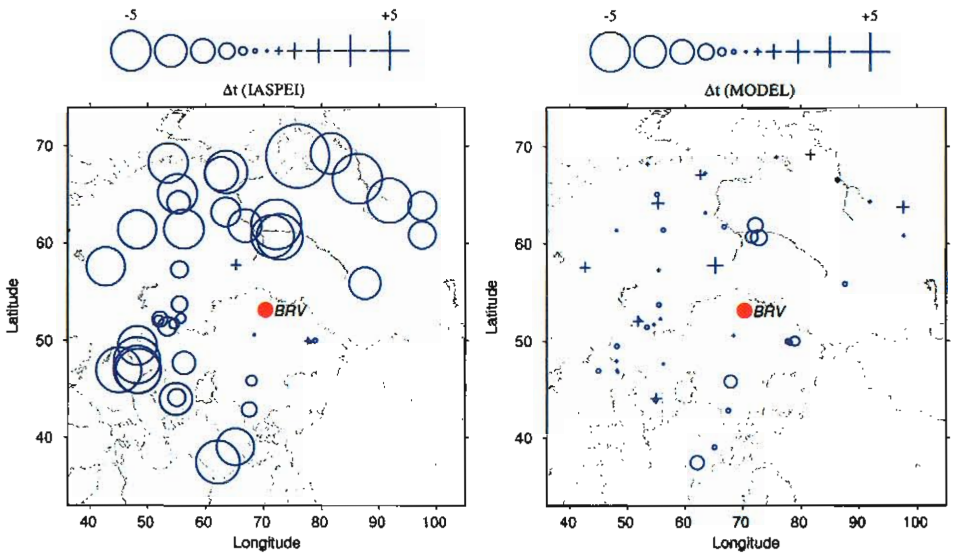

Figure 3-1. Comparison of P-wave travel time residuals for 55 GT0 PNEs from the FSU measured at the Borovoye station relative to IASPEI91 travel times (left) and relative to the travel times predicted by the regional 3-D model (right).

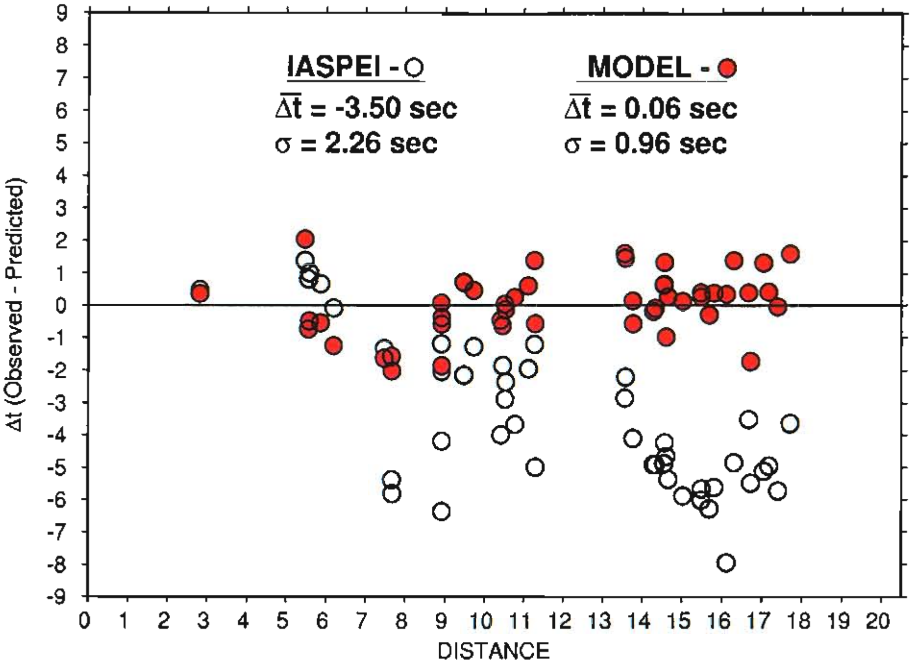

Figure 3-2. Comparison of the explosion P-wave travel time residuals as a function of distance for PNEs recorded at the Borovoye station for IASPEI91 travel times (open circles) and for the travel times from the 3-D regional model (closed circles).

We made similar comparisons for the PNEs recorded at 8 additional IMS and surrogate station sites in the FSU (cf. Figure 3-3) with similar results. For each of the stations, we

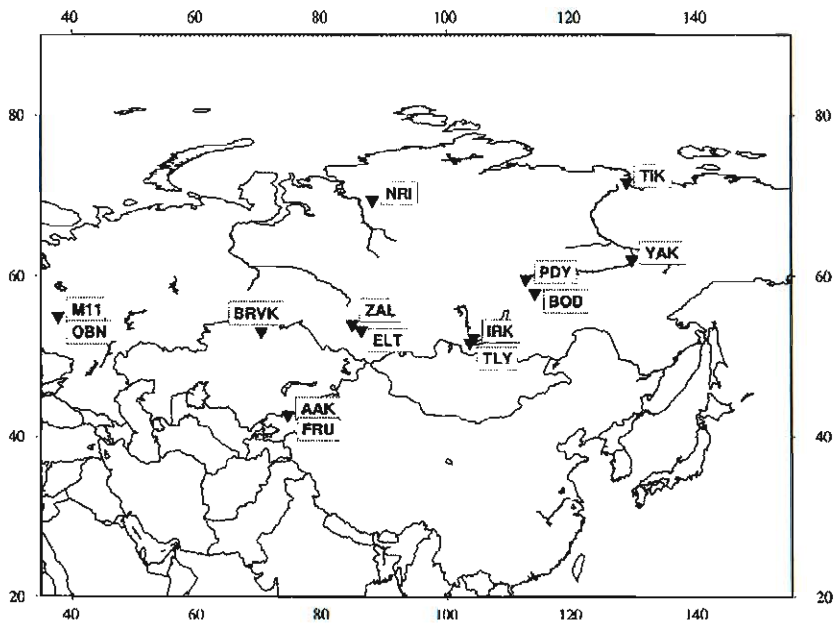

Figure 3-3. Locations of selected IMS or surrogate stations where FSU explosion data have been used to validate the P-wave travel time predictions.

computed the observed P-wave travel time residuals with respect to the predictions based on the IASPEI91 model and our refined 3-D velocity model for the region. Figures 3-4 through 3-11 show the P-wave residuals plotted as a function of location and distance based on the FSU PNE ground truth events. The results indicate that in all cases the residuals are consistently reduced for our 3-D model relative to the IASPEI91 model.

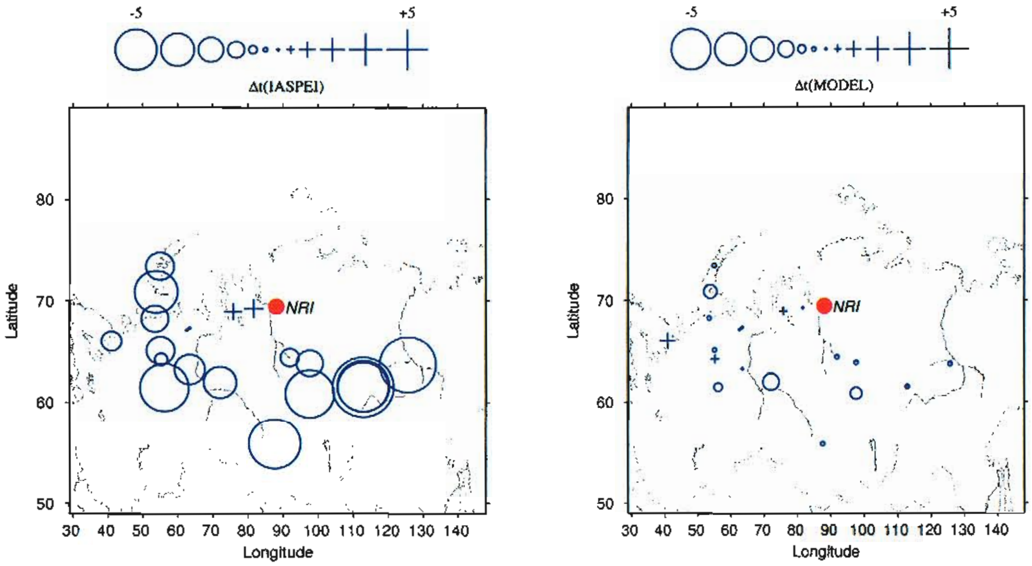

Figure 3-4a. Comparison of observed PNE residuals computed with respect to IASPEI91 (left) and our regional 3-D velocity model (right) for station NRI.

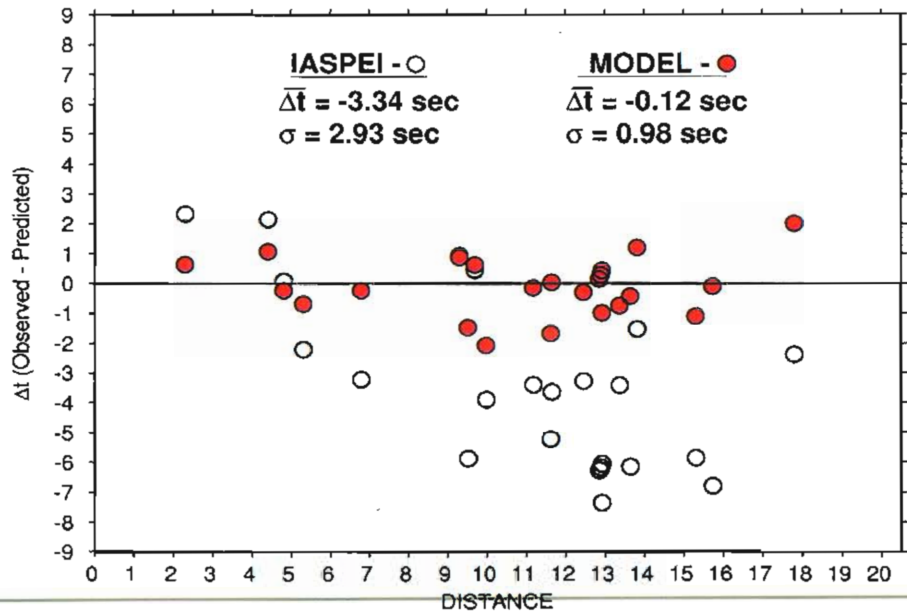

Figure 3-4b. Comparison of explosion P-wave residuals as a function of distance at NRI computed with respect to the IASPEI91 and regional 3-D velocity model.

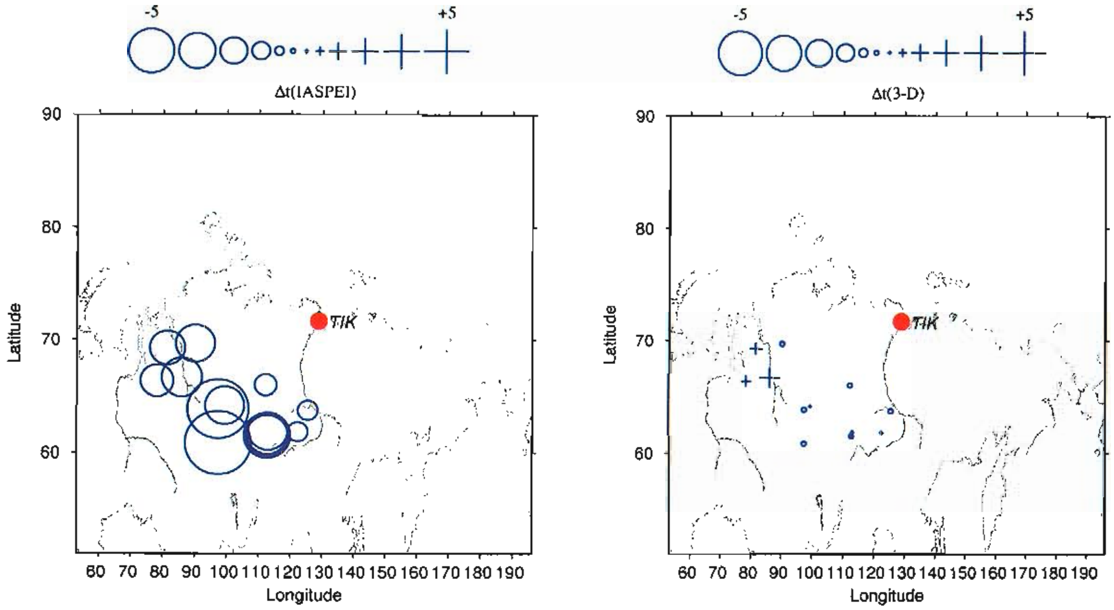

Figure 3-5a. Comparison of observed PNE residuals computed with respect to IASPEI91 (left) and our regional 3-D velocity model (right) for station TIK.

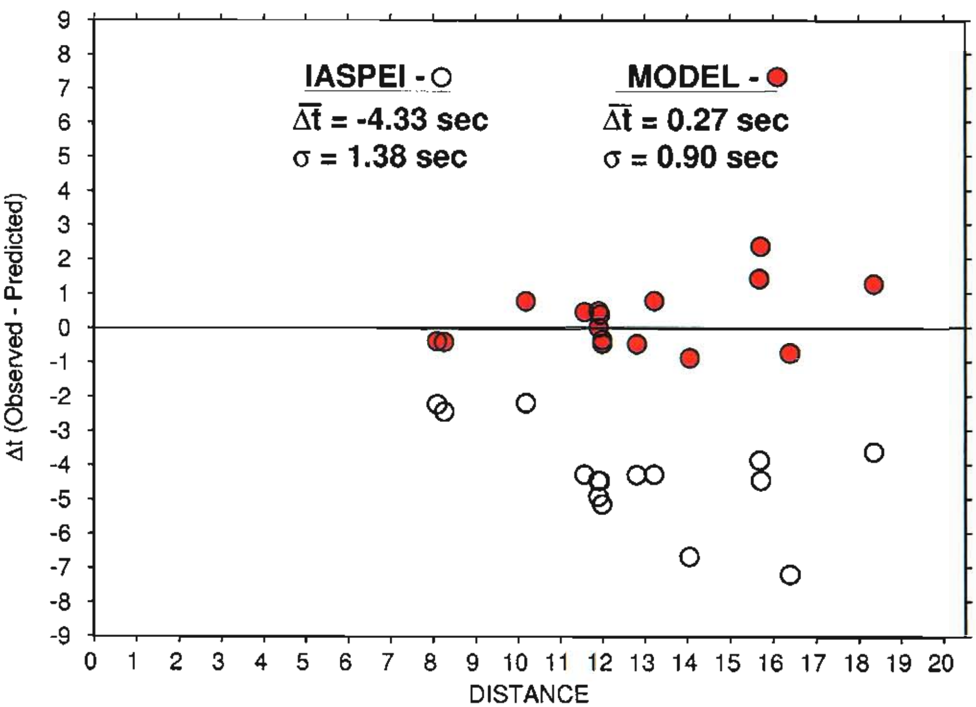

Figure 3-5b. Comparison of explosion P-wave residuals as a function of distance at TIK computed with respect to the IASPEI91 and regional 3-D velocity model.

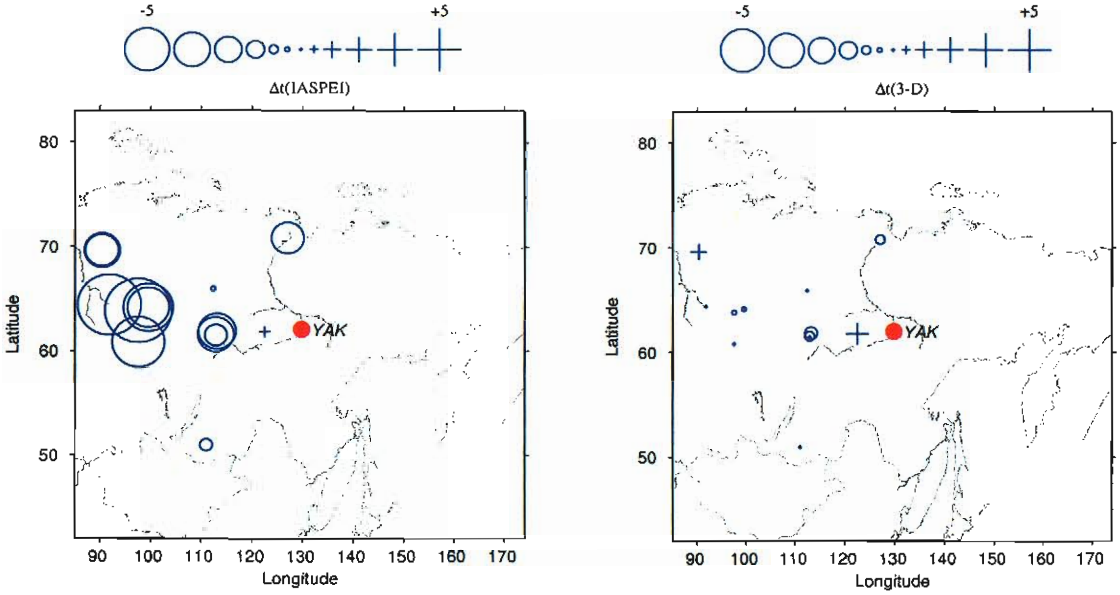

Figure 3-6a. Comparison of observed PNE residuals computed with respect to IASPEI91 (left) and our regional 3-D velocity model (right) for station YAK.

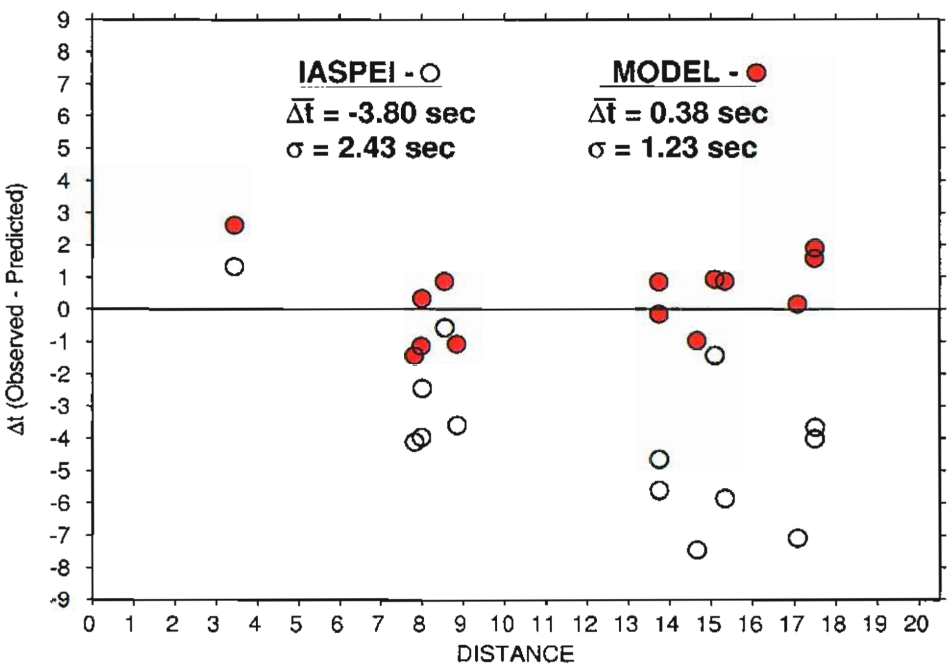

Figure 3-6b. Comparison of explosion P-wave residuals as a function of distance at YAK computed with respect to the IASPEI91 and regional 3-D velocity model.

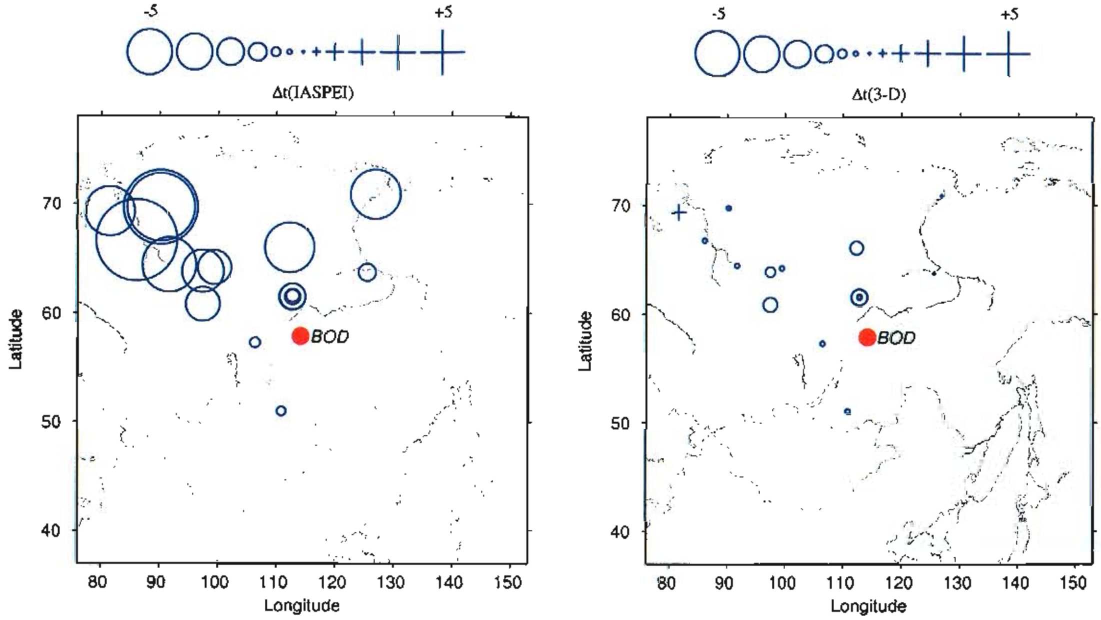

Figure 3-7a. Comparison of observed PNE residuals computed with respect to IASPEI91 (left) and our regional 3-D velocity model (right) for station BOD.

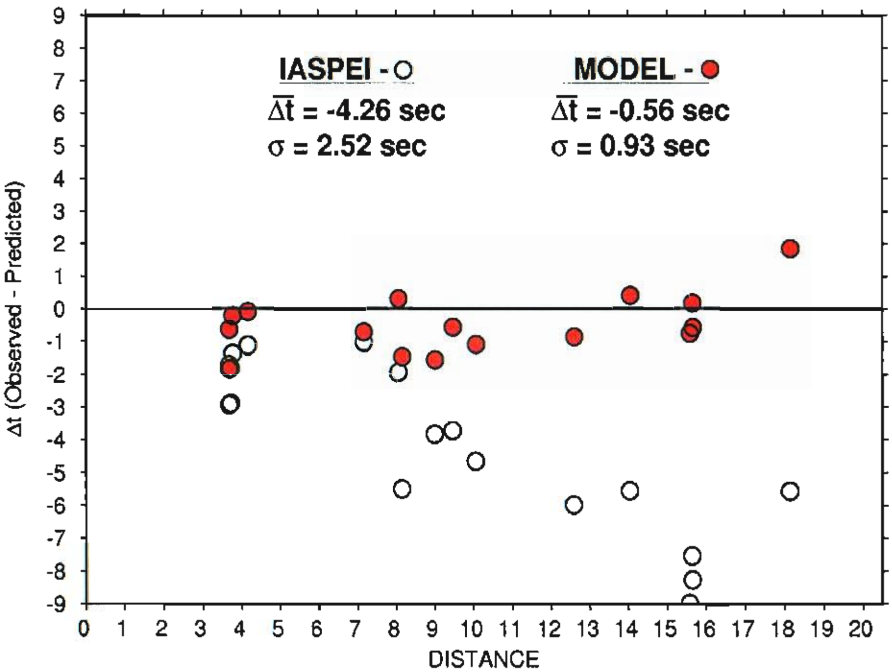

Figure 3-7b. Comparison of explosion P-wave residuals as a function of distance at BOD computed with respect to the IASPEI91 and regional 3-D velocity model.

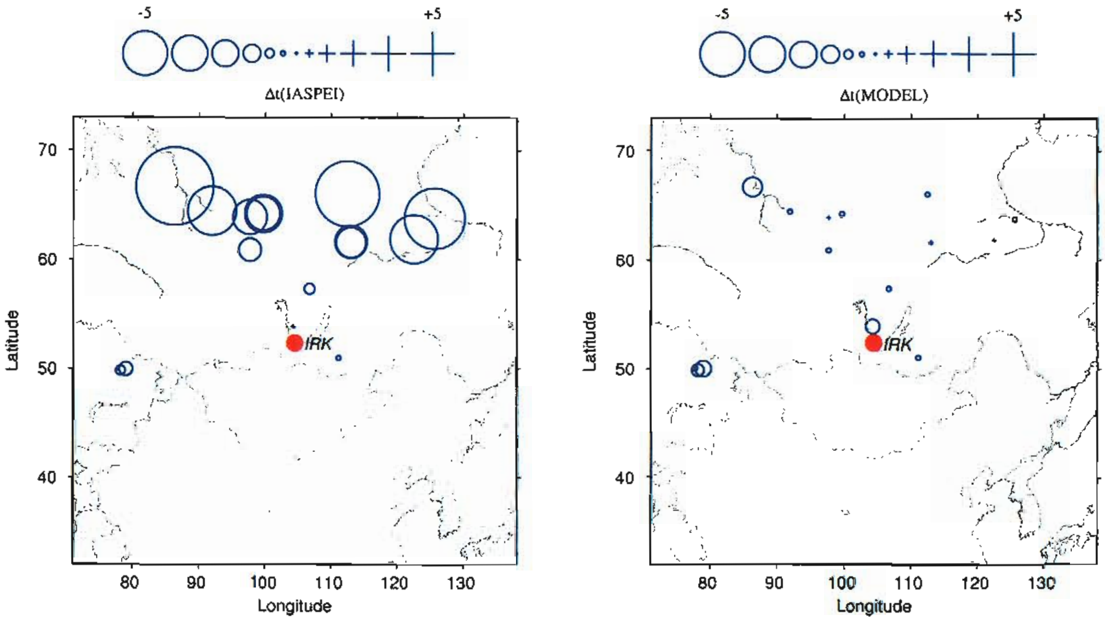

Figure 3-8a. Comparison of observed PNE residuals computed with respect to IASPEI91 (left) and our regional 3-D velocity model (right) for station IRK.

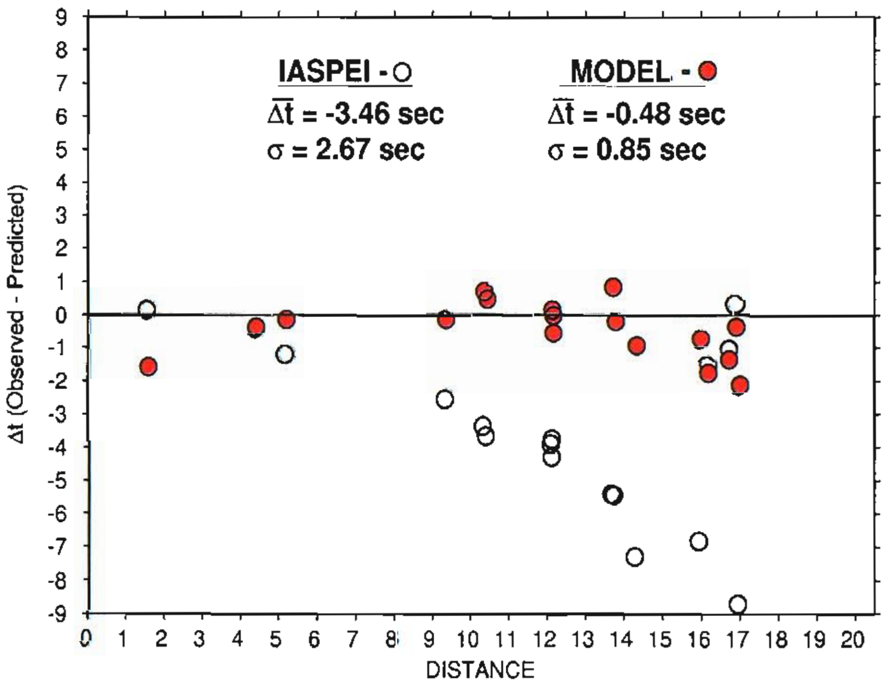

Figure 3-8b. Comparison of explosion P-wave residuals as a function of distance at IRK computed with respect to the IASPEI91 and regional 3-D velocity model.

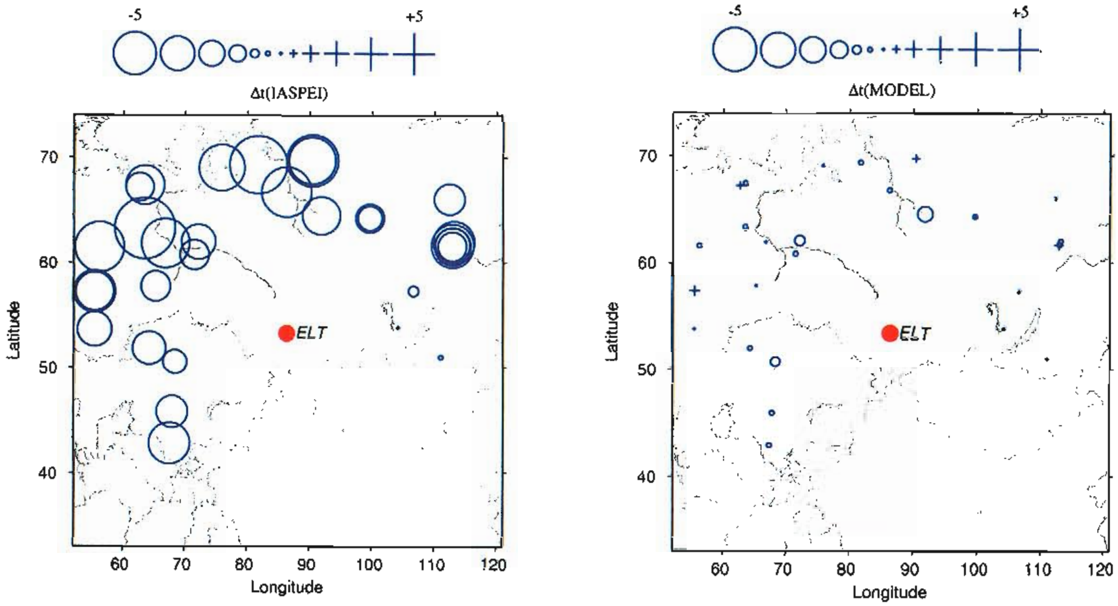

Figure 3-9a. Comparison of observed PNE residuals computed with respect to IASPEI91 (left) and our regional 3-D velocity model (right) for station ELT.

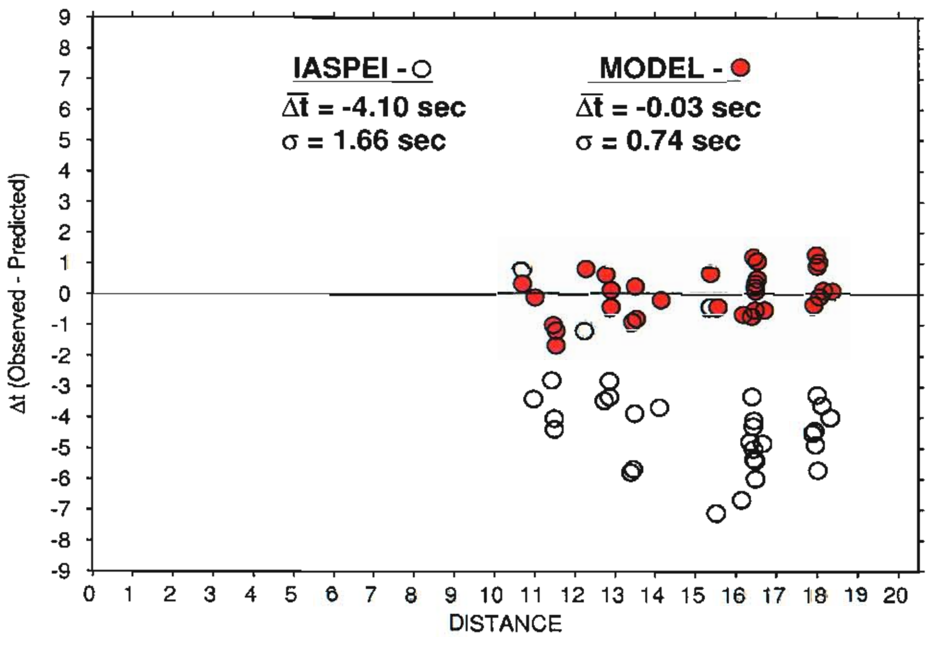

Figure 3-9b. Comparison of explosion P-wave residuals as a function of distance at ELT computed with respect to the IASPEI91 and regional 3-D velocity model.

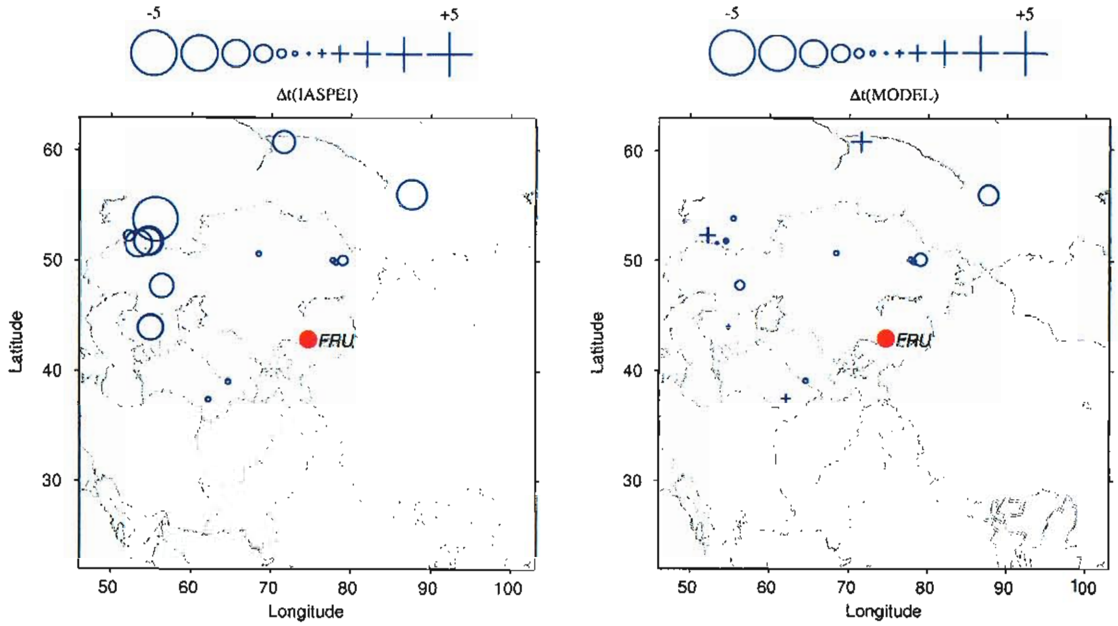

Figure 3-10a. Comparison of observed PNE residuals computed with respect to IASPEI91 (left) and our regional 3-D velocity model (right) for station FRU.

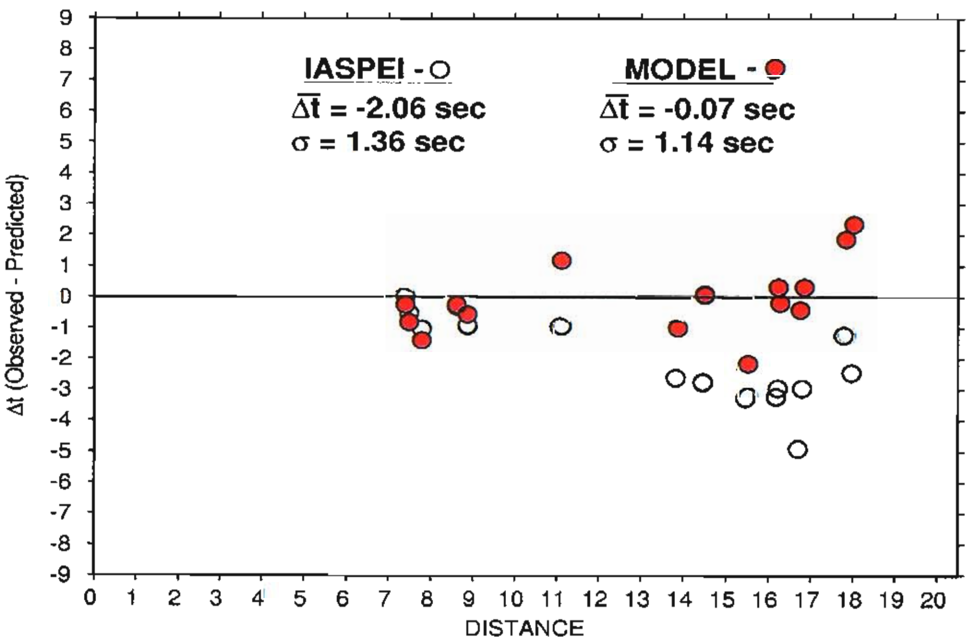

Figure 3-10b. Comparison of explosion P-wave residuals as a function of distance at FRU computed with respect to the IASPEI91 and regional 3-D velocity model.

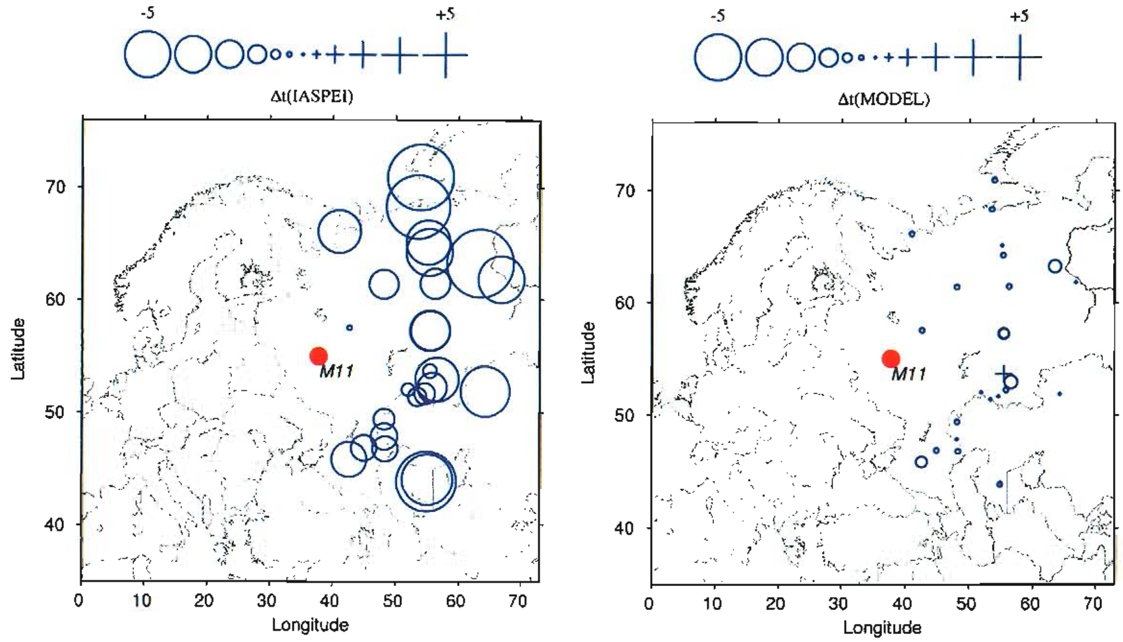

Figure 3-11a. Comparison of observed PNE residuals computed with respect to IASPEI91 (left) and our regional 3-D velocity model (right) for station M11.

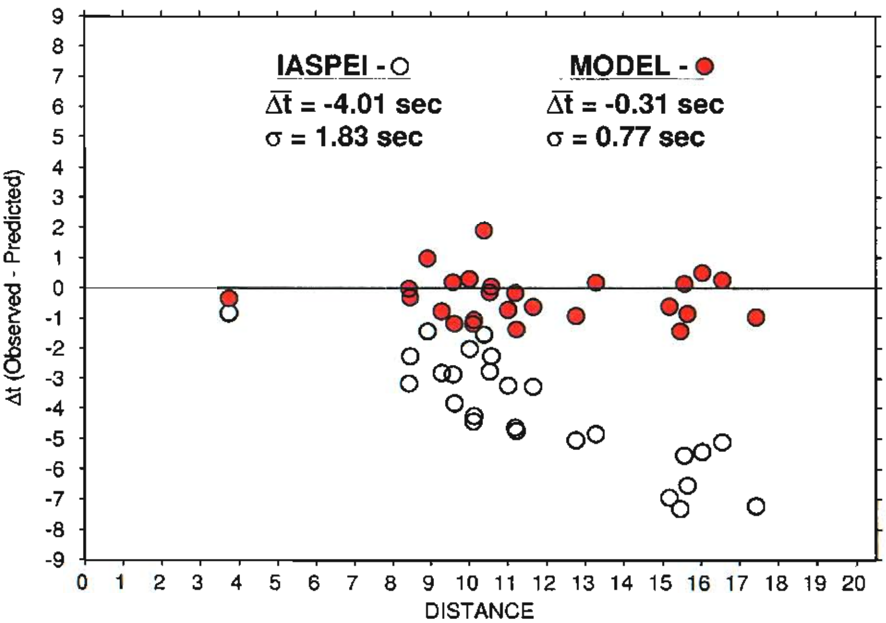

Figure 3-11b. Comparison of explosion P-wave residuals as a function of distance at M11 computed with respect to the IASPEI91 and regional 3-D velocity model.

As noted above, in all cases the average travel time residuals have been greatly reduced using the 3-D regional model (cf. Table 3-1). Over the 9 stations the average P-wave residual bias drops from – 3.65 seconds for IASPEI91 to – 0.10 seconds for the 3-D model. The corresponding average scatter is reduced from $\bar{\sigma} = 2.12$ seconds for IASPEI91 to $\bar{\sigma} = 0.94$ seconds for the 3-D model. So, our 3-D velocity model appears to be very accurately representing the travel times throughout the DSS model region of the FSU sampled by the widely distributed Soviet PNE events.

Table 3-1. Comparison of average P-wave travel time residuals for PNEs recorded at IMS stations in the FSU based on IASPEI91 and 3-D regional model.

Summary Soviet PNE Statistics for Tomographically Refined DSS Velocity Model

	IASPEI-91		3-D Model	
Station	Δt, seconds	σ, seconds	Δt, seconds	σ, seconds
BRVK	-3.50	2.26	0.06	0.96
NRI	-3.34	2.93	-0.12	0.98
TIK	-4.33	1.38	0.27	0.90
YAK	-3.80	2.43	0.38	1.23
BOD (PDY)	-4.26	2.52	-0.56	0.93
IRK (TLY)	-3.46	2.67	-0.48	0.85
ELT (ZAL)	-4.10	1.66	-0.03	0.74
FRU (AAK)	-2.06	1.36	-0.07	1.14
M11 (OBN)	-4.01	1.83	-0.31	0.77
	$\overline{\Delta t}$ = -3.65 sec	$\bar{\sigma}$ = 2.12 sec	$\overline{\Delta t}$ = -0.10 sec	$\bar{\sigma}$ = 0.94 sec

To further assess the relevance of the improvement to the P-wave travel time estimates produced from our 3-D regional model, we have analyzed the P-wave errors associated with various travel time representations used in event location. In particular, in Figure 3-12 we compare the travel time residual errors as a function of distance from our tomographically refined 3-D model for the DSS region with several alternative P-wave error estimates. The "Original IDC" error corresponds to the model used in weighting the travel time observations within the IDC hypocenter location code; so, it essentially corresponds to the errors relative to the default IASPEI91 travel time tables and is very conservative. The error model labeled "CUB" corresponds to results from the Group 2

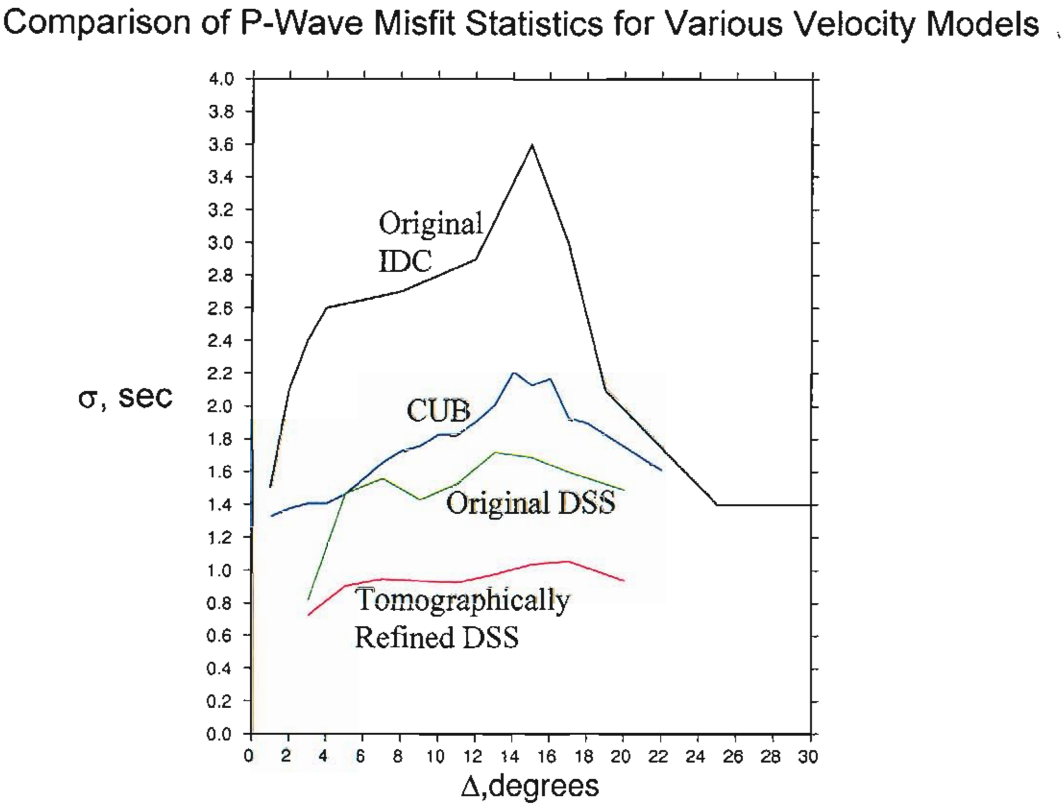

Figure 3-12. P-wave error estimates as a function of distance based on travel time residuals from our 3-D models for the DSS region compared to comparable errors from other regions.

calibration effort and is based on the residuals for events in the Group 2 region relative to the CUB velocity model. Our "Original DSS" model is a summary based on the travel time residuals for our PNE ground truth dataset of about 1000 P-wave observations relative to our initial DSS velocity model; and the "Tomographically Refined DSS" curve is a similar plot for the residuals after tomographic refinements to the 3-D model. In general, the three regional models all show reduced error in the regional distance range relative to the errors from the IASPEI91 model (i.e. Original IDC). For our Original DSS model the associated travel time errors show no particular dependence on distance over this regional distance range, and the overall level is comparable to that for the uncalibrated teleseismic travel times, which is basically the level of the Original IDC curve over the flat portion for $\Delta > 25°$. So, considering the comparable levels of the errors, the regional P-wave travel times with the corrections from the Original DSS

model should be equally weighted with the teleseismic observations in seismic event location algorithms. Furthermore, the corresponding statistics for our Tomographically Refined DSS model show again essentially no distance dependence and an average σ level substantially lower than the nominal teleseismic σ (i.e. about 1.0 seconds or less for the refined regional model versus ~1.4 seconds for teleseismic). It should be noted that this result may be a little too optimistic, since the data from which the errors were derived were also used in the tomographic refinement process. However, it seems likely that the true travel time prediction error from our regional model for the DSS region of the FSU should lie between the "Original DSS" and the "Tomographically Refined DSS" curves. In any case, there seems to be no strong evidence of distance dependence in the regional P-wave travel time error estimates from our regional 3-D model, and the σ values are comparable to or less than those for the uncalibrated teleseismic observations. So, it appears that application of these regional travel time corrections should lead to better determination of seismic event locations.

Of course, a critical test of performance for the 3-D velocity model for events from the FSU is the accuracy of event location. We analyzed the location accuracy for 14 GT0 PNE events from the FSU recorded by 4 to 6 regional IMS stations (cf. Figure 3-13).

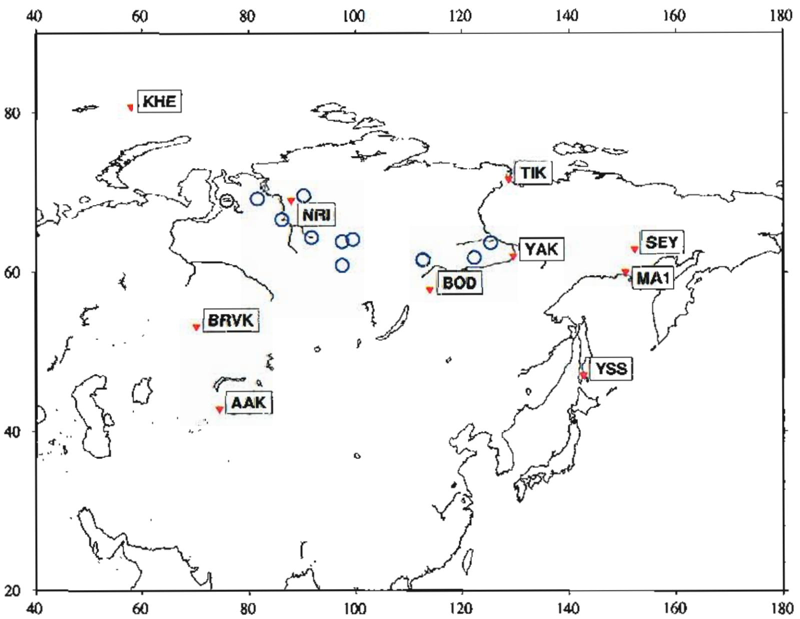

Figure 3-13. Map locations of 14 FSU PNE events (circles) used in analyzing location accuracy for the 3-D regional velocity model. Each explosion was recorded at 4-6 regional IMS station locations (triangles) in the Group 1 study area.

Figure 3-14 shows a comparison of the location errors for these events based on locations using nominal IASPEI91 travel times versus the locations using our 3-D velocity model for the region. We see that in nearly all cases the mislocations are reduced using the 3-D model. For the 14 PNEs the average mislocation for the 3-D model is only 6.9 km compared to an average mislocation of 20.4 km using the IASPEI91 travel times.

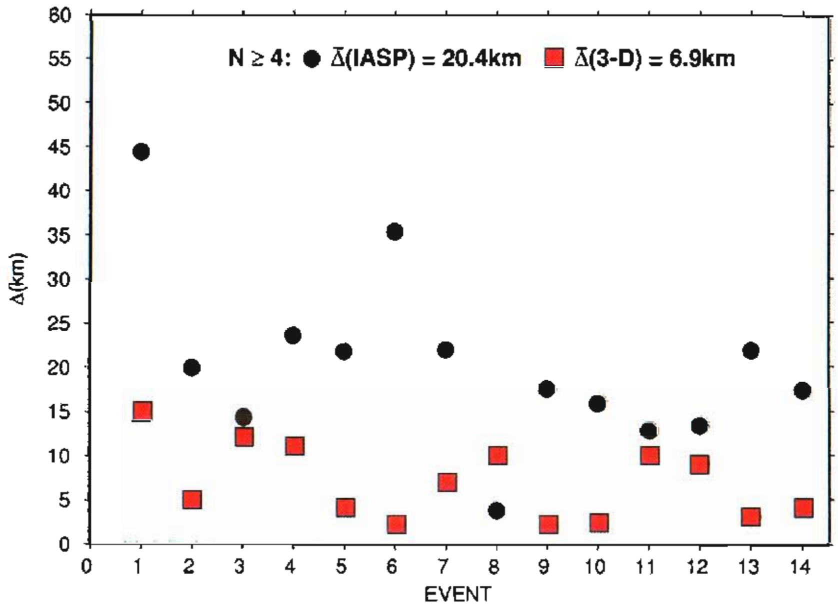

Figure 3-14. Comparison of regional seismic event location accuracies for 14 GT0 PNEs from the FSU based on observations from 4-6 IMS or surrogate IMS stations using the IASPEI91 travel times and using travel times from the regional 3-D velocity model.

We further tested the location accuracy for our 3-D regional velocity model in the northern portion of the DSS region of the FSU using observations from a sample of approximately 20 northern NZ explosions, which were observed at four Group 1 regional stations, as shown in Figure 3-15. The 3-D DSS velocity model results again produce big reductions in the average mislocations (15.8 km versus 43.8 km), as illustrated by the mislocation vectors in Figure 3-16. As seen in this figure, the event locations have a systematic bias, because of using only Group 1 stations, which are all located east of NZ. Adding data from a single Group 2 IMS station (viz. OBN), located to the west, reduces the bias and provides average location accuracy of better than 10 km, as can be seen in Figure 3-17.

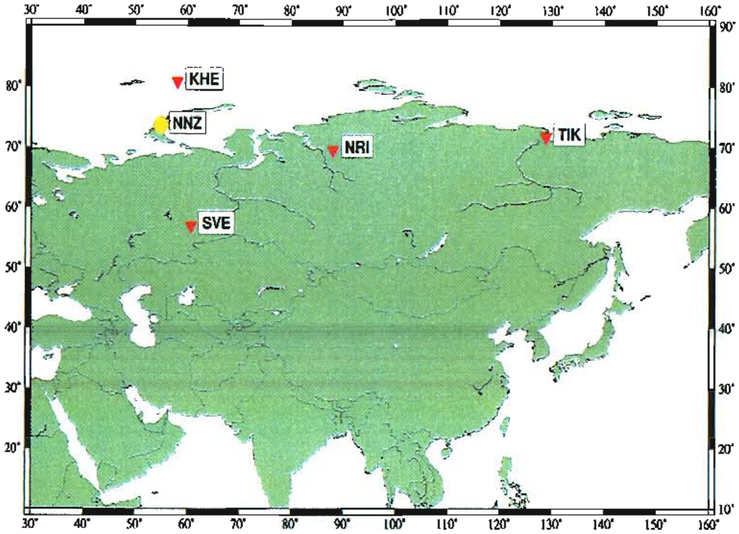

Figure 3-15. Map locations of Group 1 area regional stations (triangles) which have reported initial P wave travel times from various underground nuclear tests conducted at the Russian northern Novaya Zemlya (NNZ) test site. A sample of NNZ explosions recorded at 3 or more of these stations has been used for regional seismic location analysis to further test the applicability of our preliminary 3-D velocity model in this portion of the Group 1 study area.

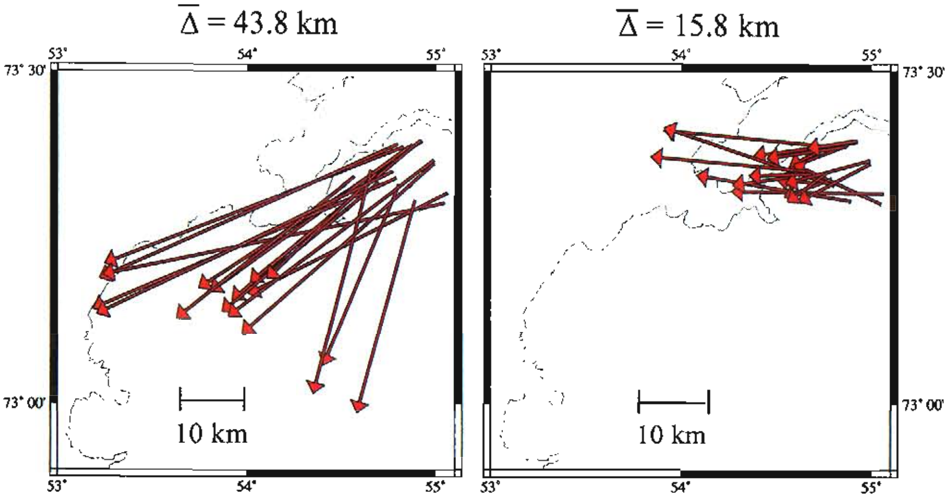

Figure 3-16. Comparison of mislocation vectors for selected northern Novaya Zemlya explosions computed with respect to seismic locations determined with (right) and without (left) corrections to the observed regional travel times with respect to IASPEI91 predicted by the preliminary 3-D velocity model of the Group 1 study area. The arrows point from the JED locations of Lilwall and Marshall (1986) to the corresponding seismic locations. Note that the use of the 3-D velocity model results in a very significant reduction in the average mislocations ($\overline{\Delta}$) relative to IASPEI91 and that both sets of mislocation vectors are oriented predominantly west/southwest, consistent with the uneven azimuthal distribution of the regional stations employed in the relocation analysis.

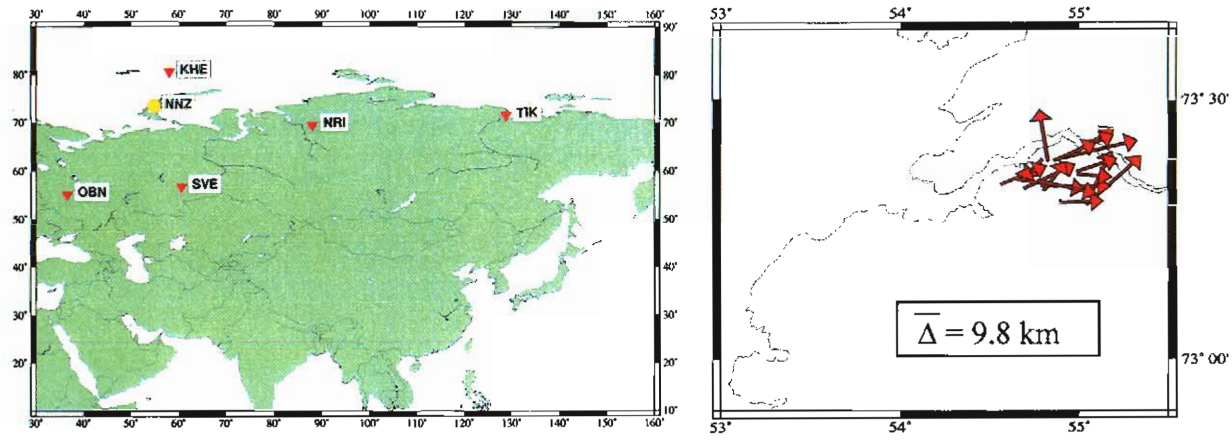

Figure 3-17. Addition of data from a single regional station (OBN) located in the Group 2 region (top) to the west of NZ produces a further significant reduction in the average mislocation ($\overline{\Delta}$) of these NZ explosions (bottom) to a value of less than 10 km.

So, the results presented here for our 3-D regional velocity model from the FSU show significantly better seismic location estimates than for the IASPEI91 nominal model. We regard this as validation of the model and the associated regional travel time predictions for the stations from the DSS region of the FSU. Therefore, we are confident that the SSSCs predicted for the Group 1 IMS stations within this region for the 3-D regional velocity model will enable more accurate event locations.

3.2 CHINA VALIDATION

As described in Section 2 above, our final velocity model for the China/Mongolia region was developed from a formal tomographic inversion of observed travel times from a large sample of events in the Annual Bulletin of Chinese Earthquakes. We have conducted a number of analyses to validate this refined China/Mongolia velocity model. One powerful means for assessing accuracy of the various velocity models for China is provided by the recently published GT locations of selected Lop Nor explosions reported by Fisk (2002). Figure 3-18 shows a comparison of Chinese Bulletin locations with the GT locations reported by Fisk et al. It can be seen that the average mislocation is about 7.3 km, with a bias dominantly to the north, which reflects sparse station coverage to the south of the Lop Nor test site. Although the Lop Nor epicenters are very well constrained

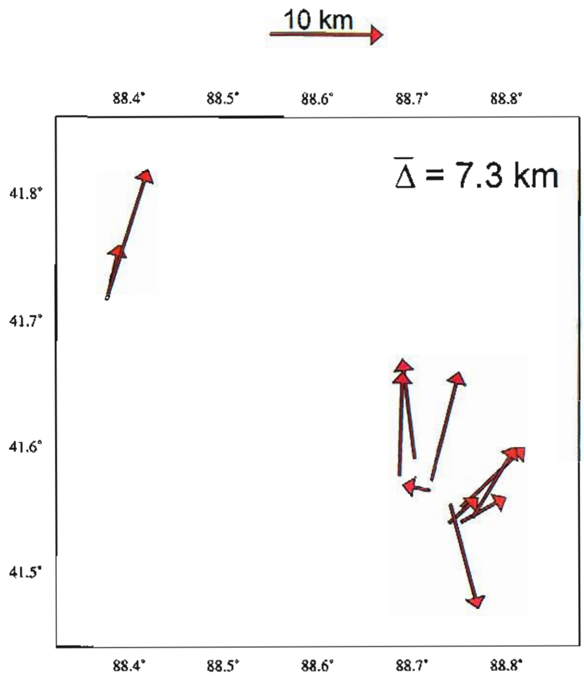

Figure 3-18. Mislocation of Chinese Bulletin epicenters with respect ground truth (GT1-GT2) locations for selected Lop Nor nuclear explosions.

by seismic and satellite image data, it is necessary to assess the accuracy of the corresponding seismic origin times in order to use the seismic data from the these explosions to definitively test various velocity models. Consequently, we conducted an analysis of the reported CSB bulletin arrival times of these Lop Nor explosions from seven reporting regional stations within 6°. The stations and their locations with respect to the Lop Nor test site are illustrated in Figure 3-19.

Figure 3-20 shows a typical result comparing the P-wave travel time residuals, relative to the origin times reported by Fisk et al., for a Lop Nor explosion of 06/08/96. The residuals on the left are for the IASPEI91 travel times compared to the residuals on the right calculated from our 3-D velocity model for the region. In these plots the symbol size is proportional to the size of the travel-time residuals, and they are plotted at the epicenter locations of the corresponding events. We find a consistent bias of from 1 to 2 seconds at these stations for the IASPEI91 model, but the residuals for our 3-D model are

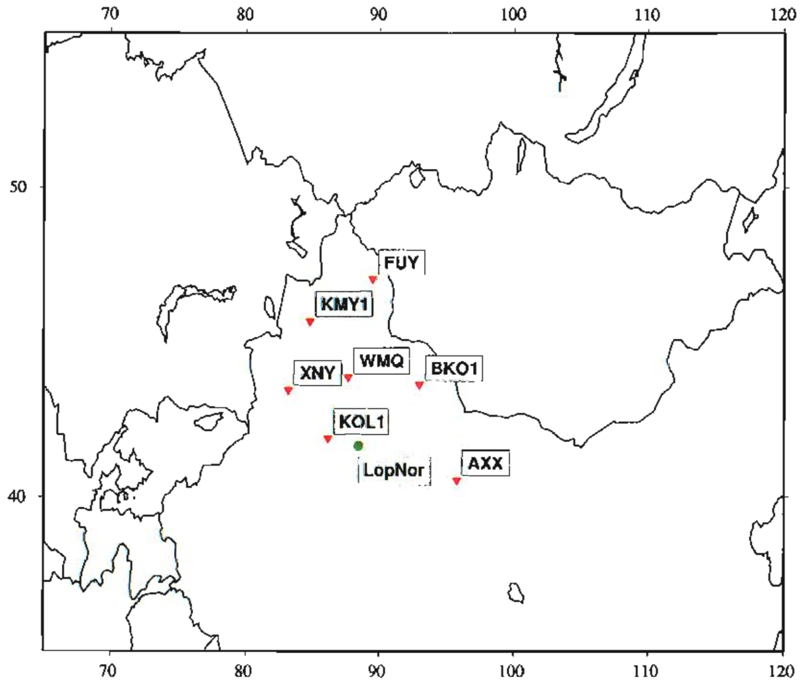

Figure 3-19. CSB stations close to Lop Nor ($\Delta \leq 6°$) with travel times reported in the CSB bulletin for Lop Nor explosions.

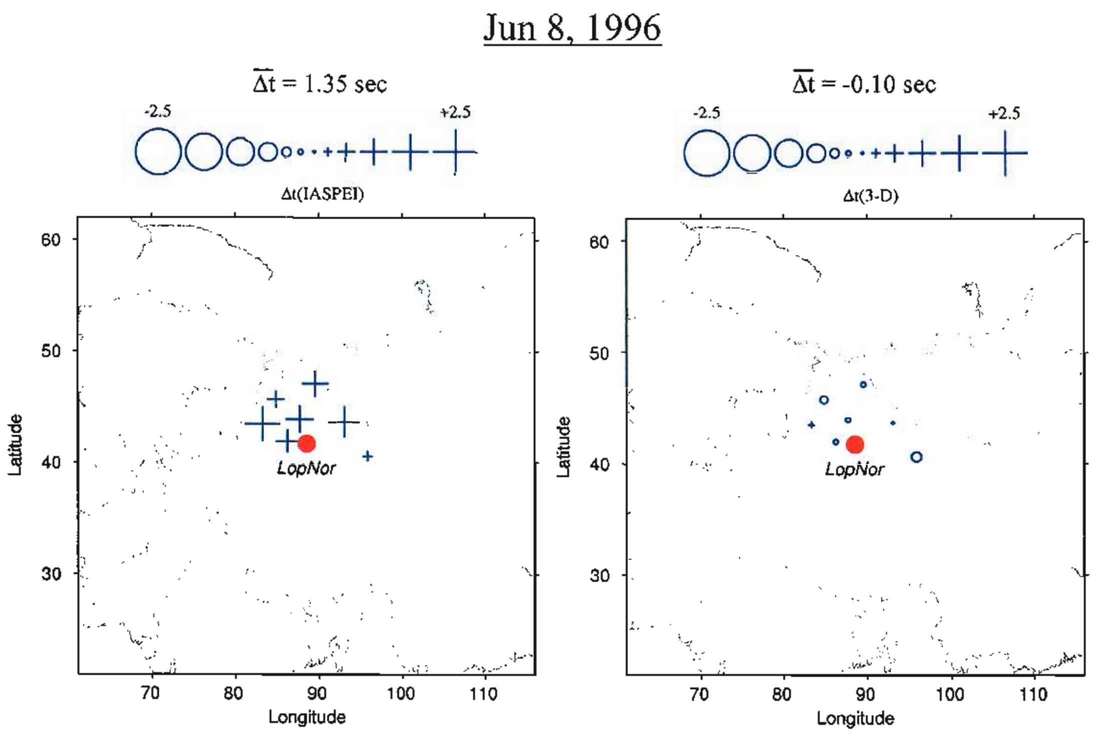

Figure 3-20. P-wave travel-time residuals at close Chinese stations for June 8, 1996 Lop Nor explosion for IASPEI91 travel times (left) and our 3-D regional velocity model (right).

close to zero. More complete results for 12 Lop Nor explosions are shown in Figure 3-21. This comparison shows that the average P-wave travel time residuals for these Lop Nor explosions with respect to IASPEI91 travel times is about + 1.25 seconds, but the corresponding average residual for our 3-D model is less than – 0.2 seconds. The scatter for both sets of observations is about the same with $\sigma \approx 0.3$ seconds. We conclude that the Fisk et al. origin times for the Lop Nor events are probably good to about ± 0.5 seconds. So, our 3-D model appears to account very well for the observed P-wave travel times in this region close to Lop Nor.

We decided to look more closely at the model validation for the China region using the observations from Lop Nor explosions recorded at 35 regional stations with travel times reported in the CSB for multiple explosions. The P-wave residuals for these events are plotted in Figure 3-22. Although the predictions from the 3-D model look very good out to about 12°, the results appear to significantly deteriorate at greater distances. At the larger distances the predicted travel times are generally too large, so the model velocities

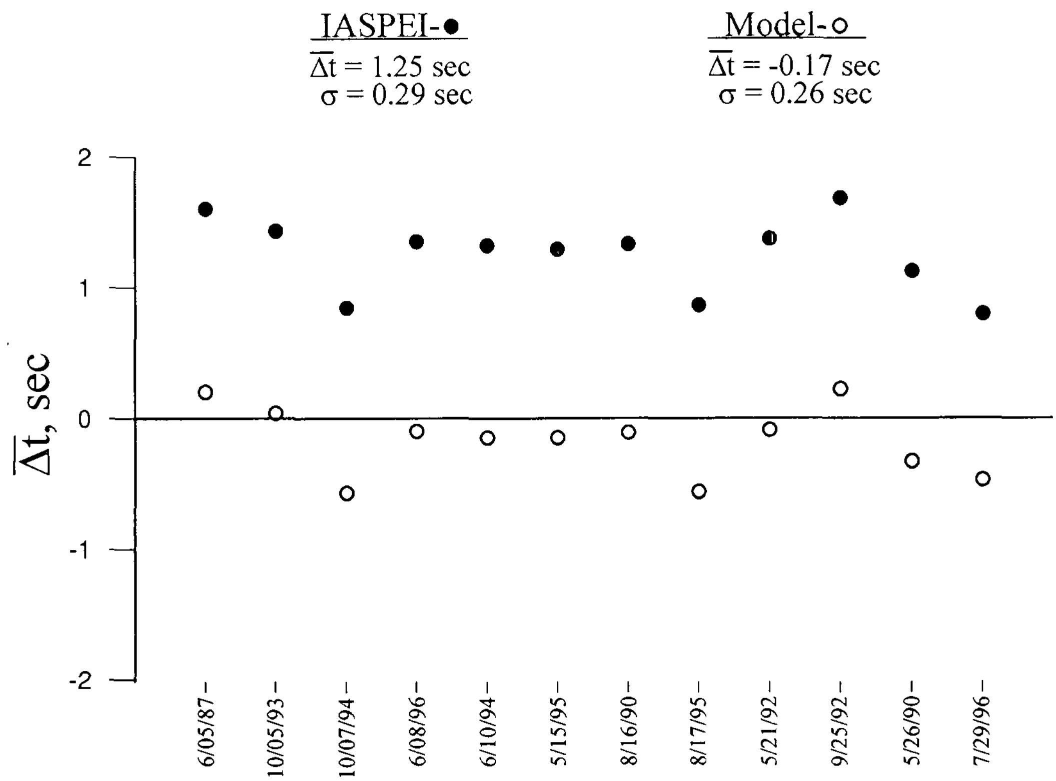

Figure 3-21. Comparison of average P-wave travel time residuals for 12 Lop Nor explosions for IASPEI91 (solid symbols) and for regional velocity model (open symbols).

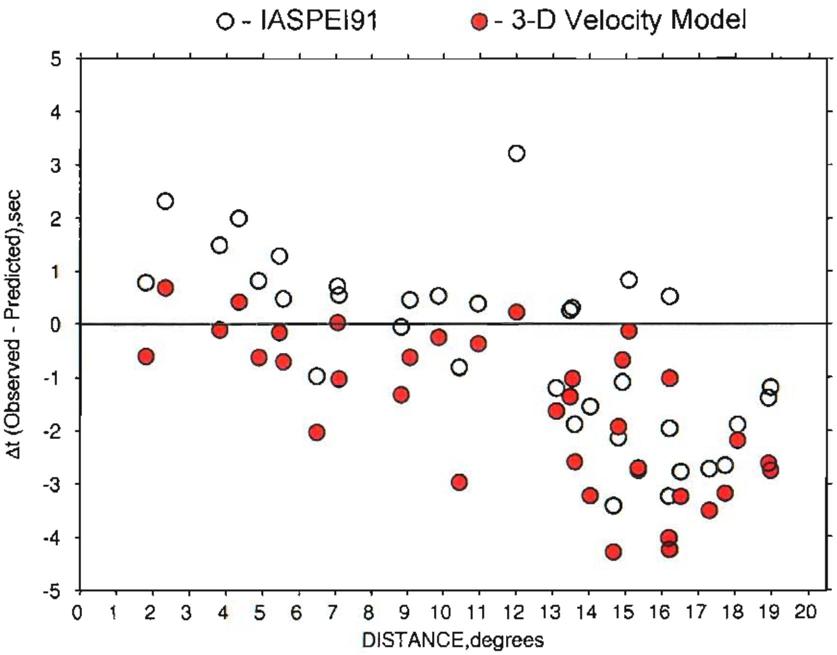

Figure 3-22. Average Lop Nor travel time residuals at CSB stations as a function of distance with respect to IASPEI91 and 3-D velocity models.

affecting this distance range are apparently too slow. This same behavior appears to be corroborated by regional earthquake travel time residuals from the CSB bulletin (cf. Figure 3-23). In this plot we have binned the data into 0.5°-distance intervals and computed the average P-wave residuals. We find a very similar trend to the Lop Nor explosion data, again apparently indicating that the upper mantle velocities in the model (below the lid) may be too low.

We have subsequently revised the China/Mongolia upper mantle velocities in our model to help compensate for this deficiency. In particular, we analyzed the travel time data from the events in the vicinity of Lop Nor and determined that significantly higher velocities would be required to match the apparent Pn velocities out to larger regional distances. We found that this problem was apparently introduced by the relatively low sub-lid velocities in our base model for the region (derived originally from surface-wave analyses) being carried through the inversion process. To correct the problem we reran the tomographic inversion starting with more uniform, higher velocities in the upper mantle for the China/Mongolia base model. In particular, for our base model we imposed

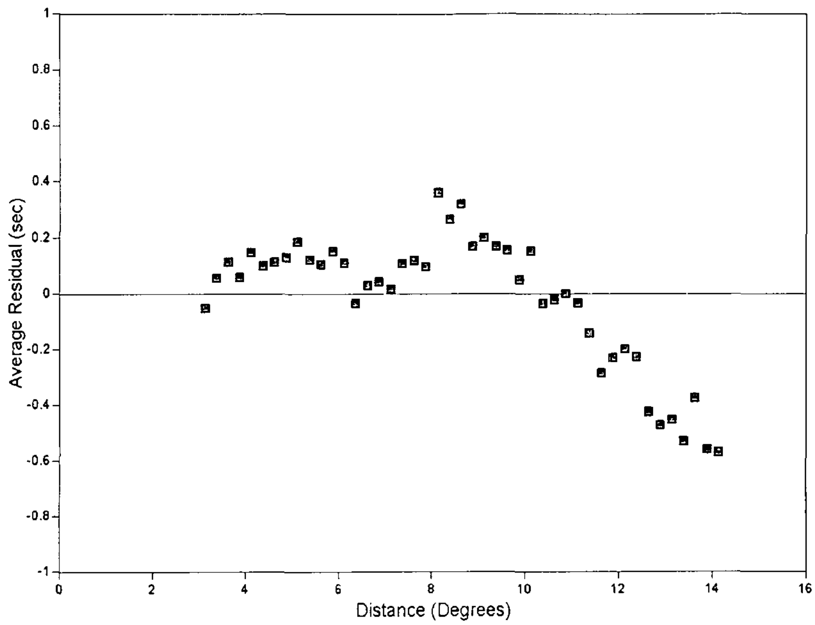

Figure 3-23. Average CSB earthquake travel-time residuals as a function of distance with respect to our China regional 3-D velocity model.

a velocity of 8.12 km/sec (as indicated by the data around Lop Nor) for the upper mantle lid (50 – 120 km), underlain by a uniform velocity increase from 8.12 to 8.3 km/sec between 120 and 165 km, velocity increasing from 8.3 to 8.43 km/sec between 165 and 210 km, and transitioning to the IASPEI91 P velocity at the 410 km upper mantle discontinuity. We reran the tomographic inversion using the same Chinese earthquake bulletin data described above with this new starting base model and determined a new refined model for China/Mongolia. The new model has very similar P velocities for the upper mantle lid (i.e. Pn) as we saw above in Figure 2-9. However, the new model has significantly higher sub-lid P velocities throughout most of the region. As a check on this model, we recomputed the P-wave travel time residuals for the Lop Nor explosions at the same 35 stations shown in Figure 3-22. These results are shown in Figure 3-24 based on the predictions from the new refined China/Mongolia model. The predictions in this case clearly match the observations much better, and the tendency toward longer predicted times at larger regional distances ($\Delta \geq 12°$) is greatly reduced. So, we have concluded

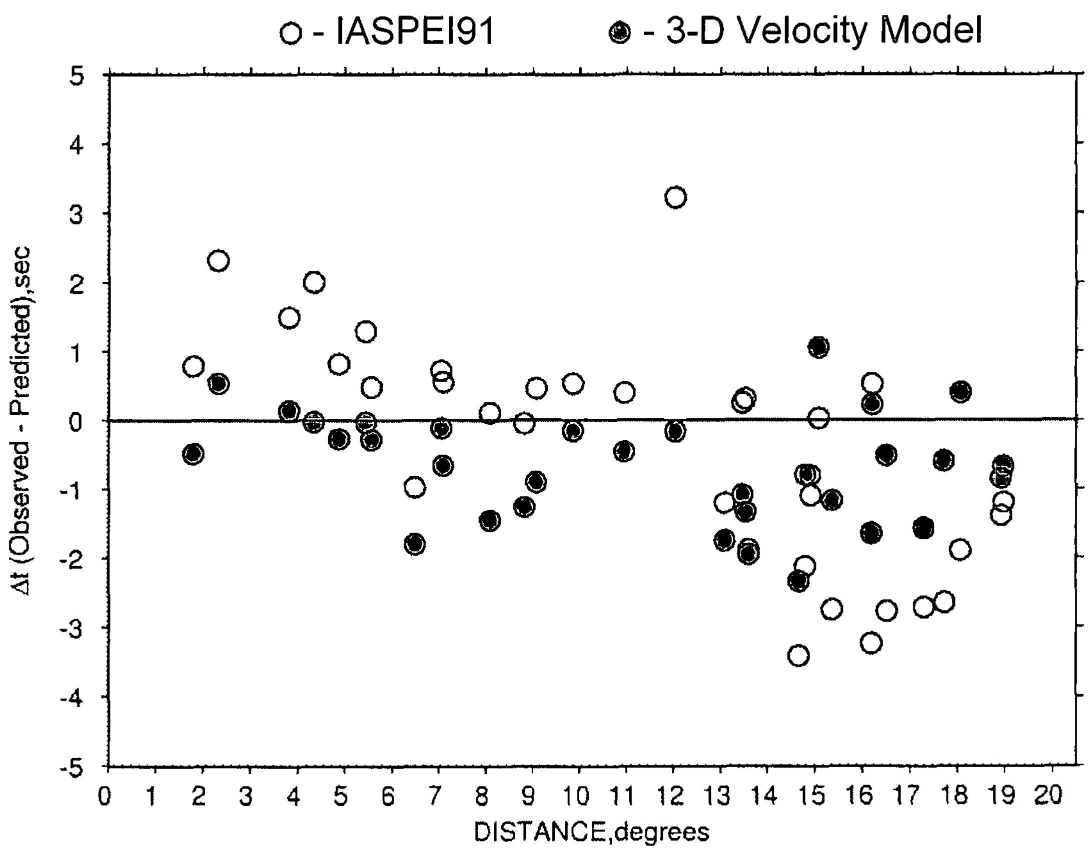

Figure 3-24. Average Lop Nor travel time residuals at CSB stations as a function of distance with respect to IASPEI91 and the revised 3-D velocity model.

that the refined China/Mongolia model developed from this later tomographic inversion better represents the observations; and we have substituted this new version into our overall 3-D velocity model for the Group 1 region.

3.3 WINPAK VALIDATION

There is very little ground truth data currently available in the India-Pakistan region that can be used to validate our WINPAK3D model. However, on 14 February 1977, a magnitude 5.2 earthquake occurred in the region near Nilore, Pakistan that was well recorded by the Tarbela and Chasma local networks. Based on data from these networks, Seeber and Armbruster (SA) (1979) found a hypocenter for the event and conducted a detailed study of the aftershock sequence. Using teleseismic as well as regional data,

both the ISC and the USGS (NEIC) located the event within about 5 km of the epicenter reported by SA, who used only the local network data. The ISC calculated the depth of the event to be 27 km, and the USGS fixed the depth at 33 km. However, the hypocenters of the main shock (14.5 km) and the 50 accurately located aftershocks determined by SA indicate a rupture surface between 12 and 18 km depth.

Because of the regional station coverage and the further constraint on the hypocentral region derived from the aftershock study, the 14 February 1977 event (denoted the VDAY event) has one of the best constrained locations in the region. Therefore, we began preliminary testing of the location capability of our updated velocity model using a subset of regional stations from this event. Figure 3-25a shows the regional stations that were used to locate the VDAY event; the maximum azimuthal gap is 140°. We used 3-D travel time tables from both our initial and final WINPAK3D models to locate the VDAY event and compared the results with the location using the 1-D IASPEI91 tables. Figures 3-25b and 3-25c show the hypocenters from the VDAY event, calculated using data from 11 regional stations, for the updated WINPAK3D model (blue *), initial WINPAK3D model (red *), and the 1-D IASPEI91 model (green *). We compare these solutions with the SA location for this event (black star). The surface and depth projections of the respective three-dimensional confidence regions determined by Monte Carlo simulation (Rodi and Toksöz, 2000) show the 95% confidence levels for each model's hypocenter. The epicenter mislocation of the updated WINPAK3D model from the SA event location is 3.5 km, while the initial model's epicenter mislocation is 9.3 km and the IASPEI91 epicenter mislocation is 31.7 km. In addition, the 95% confidence regions for both the initial and updated WINPAK3D model epicenters encompass the SA epicenter while the 95% confidence region for the IASPEI91 epicenter does not.

Also shown in Figures 3-25b and 3-25c are the hypocenters determined by both the ISC and the USGS (NEIC) (open circles) using teleseismic data as well as regional data. Note that by using regional data alone, the 3-D model is able to estimate the hypocenter of this event as well as the teleseismically-derived estimates. The results of this focused study for an individual event show that our WINPAK3D regional velocity model can provide

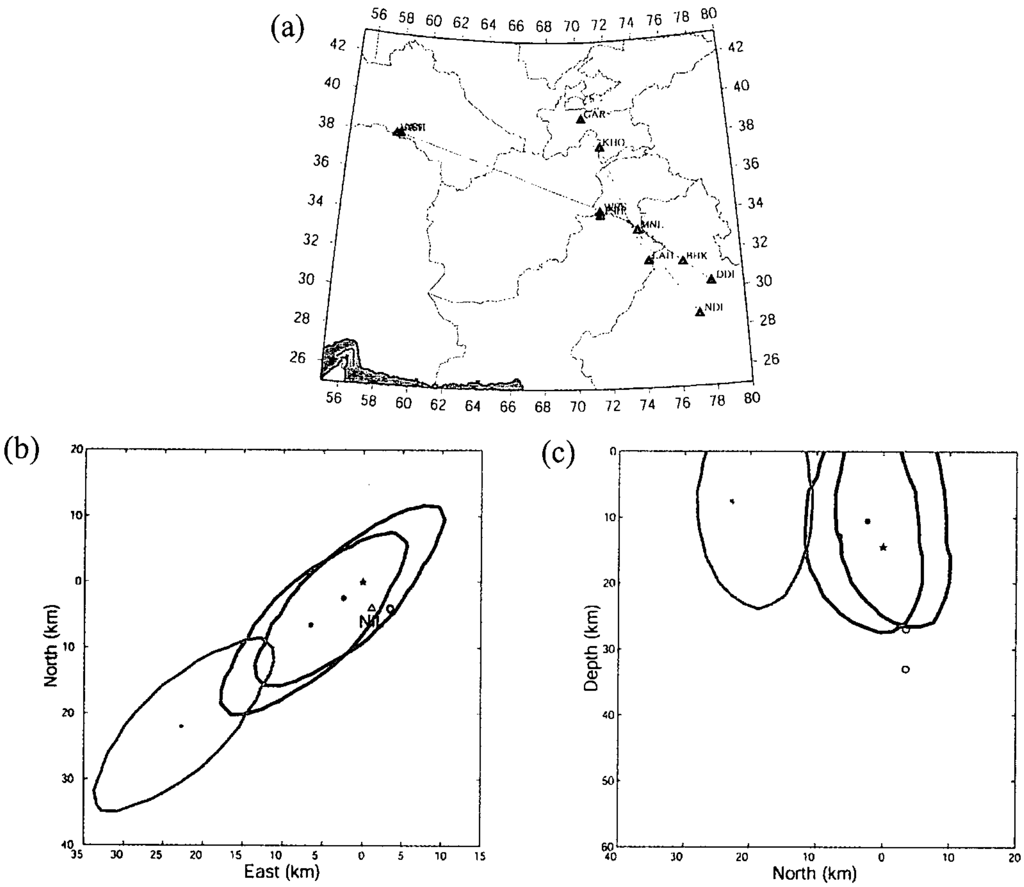

Figure 3-25. (a) Eleven regional stations used to locate the Valentine's Day event. Hypocenter solutions calculated with the updated WINPAK3D model (blue *), the initial WINPAK3D model (red *), and the 1-D IASPEI91 model (green *) are shown in b) map view and c) depth vs. latitude plots. The Seeber and Armbruster location for this event is denoted by the black star. Also shown are the hypocenters determined by both the ISC and the USGS (NEIC) (open circles) using teleseismic data as well as regional data.

more accurate locations of small events, that are not recorded teleseismically. To further investigate these capabilities and validate our model, we performed a series of location analyses on a set of ground-truth events. Our multi-event validation tests were performed using a set of 17 reference events shown in Figure 3-26 with GT5 accuracy or better. Almost all of the earthquake reference event locations were selected from both the Engdahl and Bergman (2001) cluster analysis database and from the earlier data sets resulting from studies by Engdahl et al. (1998). There are three earthquake clusters in the validation data set: Koyna, Garm, and Chamoli. In addition to the earthquake clusters, we include the Valentine's Day event, discussed above, and the Bhuj, India mainshock.

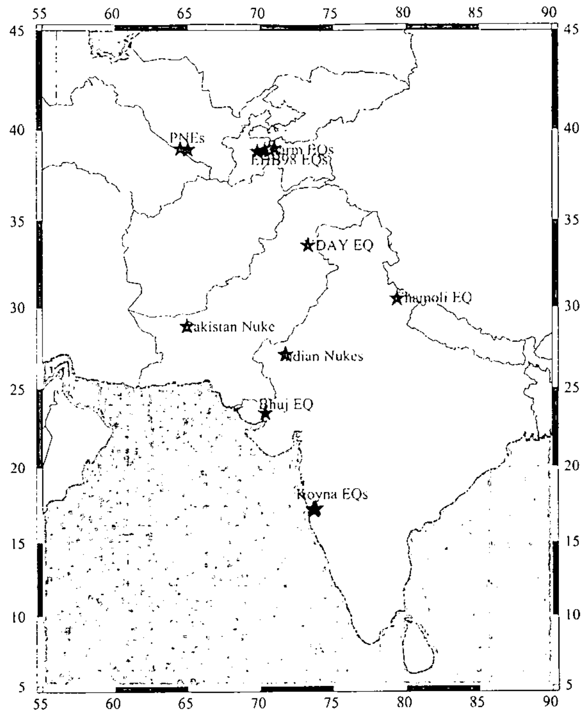

Figure 3-26. Distribution of the set of GT5 reference events used for validation of the WINPAK3D model.

We also include some explosion events in our validation data set. These are limited to the two Indian nuclear explosions, one Pakistani nuclear explosion, and two Peaceful Nuclear Explosions located in the Former Soviet Union, all of which are considered to be known to within 1 km. The reference event data set was intentionally excluded from our inversion database to allow for an independent validation analysis.

Our model validation approach included relocation of our set of reference events and analysis of the results for three cases: fixed hypocenter, fixed depth, and no constraints. We present the results in Figures 3-27 through 3-29, identifying the number of events improved versus the number of events deteriorated relative to IASPEI91. The graphs show percentage improvement (epicenter, depth, RMS travel time residuals) over IASPEI91 versus number of events. When we fixed the hypocenters to the GT5 locations (see Figure 3-27), we found that while the mean travel time residuals for both the IASPEI91 model and the WINPAK3D model were approximately zero, the standard deviation was 1.85 sec for the WINPAK3D model and 2.48 sec for the IASPEI91 model.

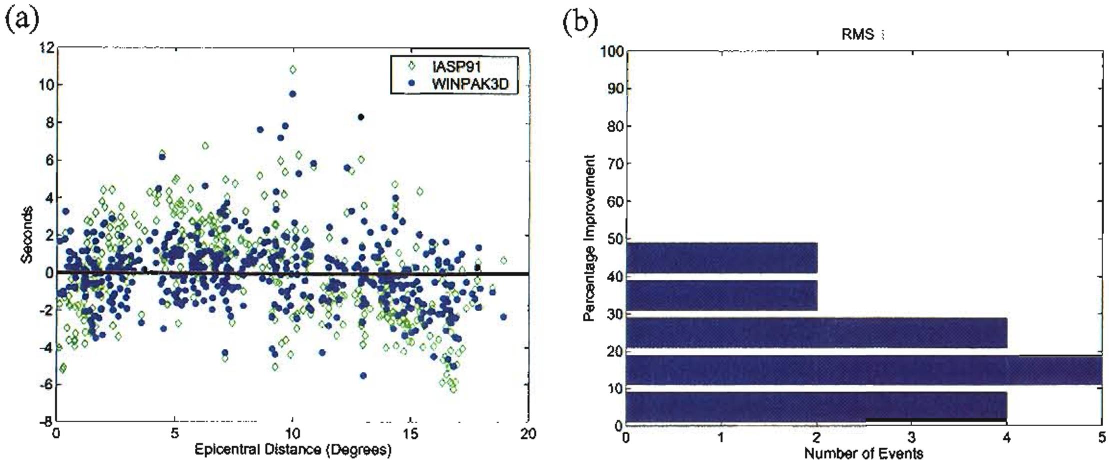

Figure 3-27. Validation results for the case where reference events are fixed to their known locations: (a) Travel time residuals for IASPEI91 (green diamonds) and the WINPAK3D (blue dots) models. (b) Percentage improvement in RMS travel time error compared with IASPEI91 versus number of events.

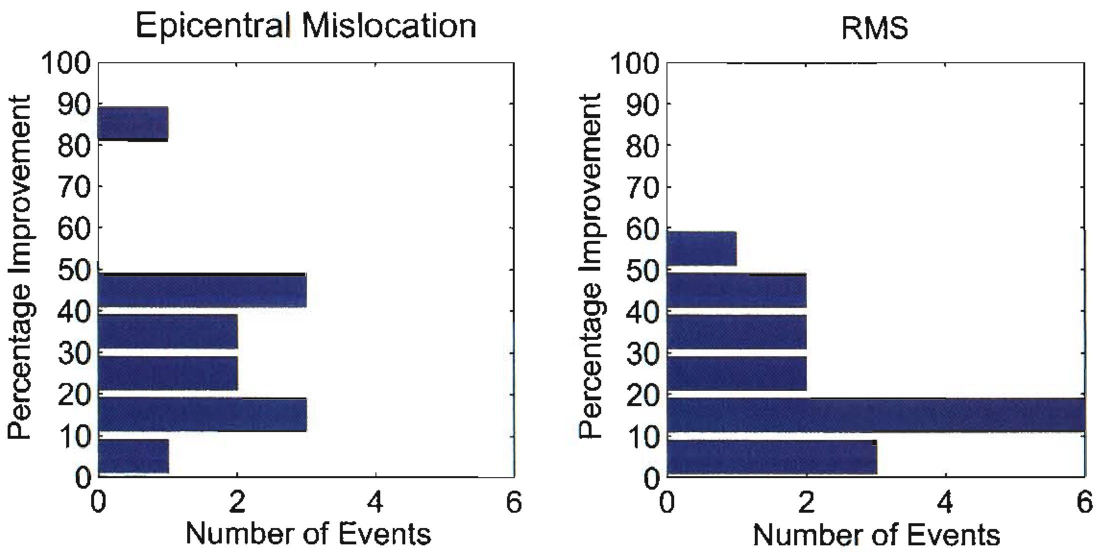

Figure 3-28. Validation results for the case where epicentral location is determined, but the depths of reference events are fixed. Percentage improvement compared to IASPEI91 for (a) epicentral mislocation and (b) RMS travel time error.

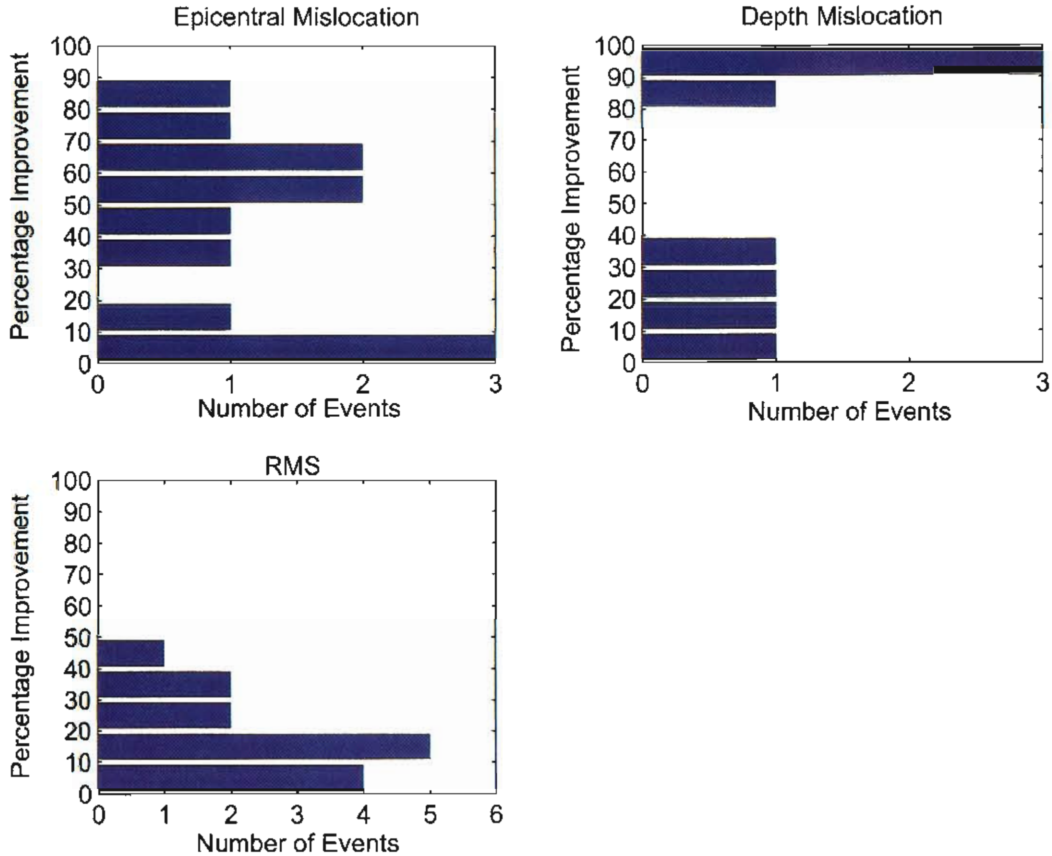

Figure 3-29. Validation results for free hypocenter relocations. Percentage improvement compared to IASPEI91 in (a) epicentral mislocation, (b) depth mislocation, and (c) RMS travel time error.

In general, the IASPEI91 residuals exhibit a greater bias towards positive residuals out to 10 degrees in this region, with a negative bias beyond 10 degrees. Additionally, the WINPAK3D model reduced RMS travel time error for all 17 events by a mean of 21.2%.

In the second case, we fixed the event depths and solved for epicentral locations. The results are shown in Figure 3-28. While WINPAK3D improved the RMS travel time residuals for 16 out of 17 events, it improved epicentral mislocation for only 12 out of 17 events, or 70% of the events. Mean percent improvement in epicentral mislocation was 33.6%. For those events where event locations were degraded, IASPEI91 mean percent improvement was 38.7%. With regard to RMS travel time residuals, mean percent

improvement was 23.7% for WINPAK3D. For the one event that had a lower RMS error based on the IASPEI91 model, its mean percent improvement over the WINPAK3D model was only 9.7%.

In the last case, we performed a free hypocenter relocation. These results are shown in Figure 3-29. Epicentral mislocation was improved for 12 of 17 events with a mean improvement of 38.7%. For the 5 events where the IASPEI91 model found more accurate locations, its mean improvement over the WINPAK3D model was 39.4%. Depth mislocation, in this case, demonstrates the most dramatic improvement. The WINPAK3D model improved depth accuracy for 13 of 17 events by a mean improvement of 68.5%. On the other hand, the mean improvement was only 18.0% for the 4 events where IASPEI91 found a more accurate event depth. Finally, RMS travel time error was improved for 14 of 17 events by a mean of 24.5%. The IASPEI91 model had smaller RMS residuals for 3 events with a mean improvement over WINPAK3D of 30.8%.

These results demonstrate that the WINPAK3D model is a significant improvement over the IASPEI91 model for regional location calibration. For this set of 17 reference events, travel times calculated through the WINPAK3D model were more accurate than those calculated with the IASPEI91 model for at least 80% of the data. As a result, event locations determined using the WINPAK3D model were found to be more accurate, in both depth and epicenter, for at least 70% of the data set. We are confident that the WINPAK3D sub-model is a substantial improvement in regional calibration for the Group 1 IMS stations in and around the India-Pakistan region.

SECTION 4

EXTENSION TO SECONDARY SEISMIC PHASES

4.1 CONVERSION TO S-WAVE VELOCITY MODELS

In addition to the primary (P) phases, secondary seismic phases may be especially useful in locating small regional seismic events. For example, traditional methods of locating regional events often utilize S – P times to provide preliminary estimates of source-to-station distance. More sophisticated seismic location algorithms can use a variety of secondary seismic phase times to achieve more reliable location estimates. However, just as with primary phases, the secondary phase travel times need to be calibrated on a regional basis to be helpful in reducing location error. To help in regional calibration of secondary seismic phases, we have conducted preliminary analyses of model-based methods, following procedures similar to those described above for the regional P waves. In particular, to test this approach we have derived and conducted initial validation of a 3-D S-wave velocity model for the Group 1 region by converting from the P-wave model using relationships based on Poisson's ratio values. This 3-D S-velocity model can then be used to predict regional travel times and corrections (SSSCs) for S and possibly other secondary phases (e.g. Lg), which may be useful for event location.

We assume that the S velocity model has the same general description as our 3-D P velocity model represented by the UMP velocity-versus-depth profiles at the geographic grid elements spaced uniformly in latitude and longitude. The S velocities at each node in the model are simply obtained from the relationship:

$$V_S = V_P \left[\frac{1-2\sigma}{2(1-\sigma)} \right]^{1/2} \tag{4-1}$$

where σ is the Poisson's ratio and V_P the P velocity at any node in the model.

4.2 POISSON'S RATIOS FOR THE CRUST AND UPPER MANTLE

Values of Poisson's ratio for rocks in the earth's crust and upper mantle are generally in the range of $\sigma \approx 0.25$. Rocks in the earth's crust generally have somewhat lower Poisson's ratios than rocks in the upper mantle. Thus, for the IASPEI91 model Poisson's

ratios fall in the range from about 0.24 to 0.29 over depths from the earth's surface down to the upper mantle velocity discontinuity near 410 km. Although this range does not appear to be very large, it should be noted that small differences in the Poisson's ratios can produce large differences in the corresponding S velocities within the earth model and in the associated S-wave travel time calculations.

Toksöz and his colleagues at MIT reviewed published reports for the existing P- and S-wave velocity models for China and analyzed the relationship between P and S velocities for the crust and upper mantle. In general, they found differences in the velocity ratios between the crust and upper mantle. In particular, they found that V_P/V_S ratios in China increase with depth and were in the range from 1.74 to 1.83 at crustal depths and in the range from 1.83 to 1.85 in the upper mantle. The corresponding Poisson's ratios have values near 0.21 for crustal rocks with P velocities near 5.50 km/sec and increase to values near 0.29 for crustal and upper mantle rocks with P velocities near 7.80 km/sec and higher. The MIT group results indicate that the relationship between the P and S velocities for China crust and upper mantle rocks can be expressed in the form of a simple relationship:

$$V_P^2 / V_S = 2.04\, V_P - 1.655 \tag{4-2}$$

So, within China we use this relationship to derive the S velocities from the P velocities in our 3-D model.

For the model outside of China, we adopted a constant Poisson's ratio of $\sigma = 0.26$, which implies $V_P/V_S = 1.7559$ everywhere. Under this assumption the S-wave raypaths through the 3-D model are exactly the same as the corresponding P-wave raypaths, and $T_S/T_P = 1.7559$. We can use this to derive a simple relationship between the S-wave SSSCs and the P-wave SSSCs, as follows. By definition

$$\mathrm{SSSC(P)} = T_P\,(3-\mathrm{D\,Model}) - T_P\,(\mathrm{IASPEI91}) \tag{4-3}$$

$$\mathrm{SSSC(S)} = T_S\,(3-\mathrm{D\,Model}) - T_S\,(\mathrm{IASPEI91}) \tag{4-4}$$

$$= 1.7559\, T_P\,(3-\mathrm{D\,Model}) - T_S\,(\mathrm{IASPEI91}) \tag{4-5}$$

$$= \quad 1.7559\left[T_P(3-\text{D Model}) - \frac{T_S(\text{IASPEI91})}{1.7559}\right] \tag{4-6}$$

$$= \quad 1.7559\left[\text{SSSC}(P) + T_P(\text{IASPEI91}) - \frac{T_S(\text{IASPEI91})}{1.7559}\right] \tag{4-7}$$

So, for this constant Poisson's ratio, the S-wave SSSCs can be expressed simply in terms of the P-wave SSSCs as:

$$\text{SSSC}(S) \quad = \quad 1.7559\,\text{SSSC}(P) + \left[1.7559\,T_P(\text{IASPEI91}) - T_S(\text{IASPEI91})\right] \tag{4-8}$$

For areas where this constant Poisson's ratio is applicable, we can then use the calculated P-wave SSSCs to generate the corresponding S-wave SSSCs by applying the simple correction involving the IASPEI91 P and S travel times.

We illustrate this S-wave travel time prediction capability for a path in the FSU platform region to the northeast of station Borovoye in Figure 4-1. This plot compares the S-wave

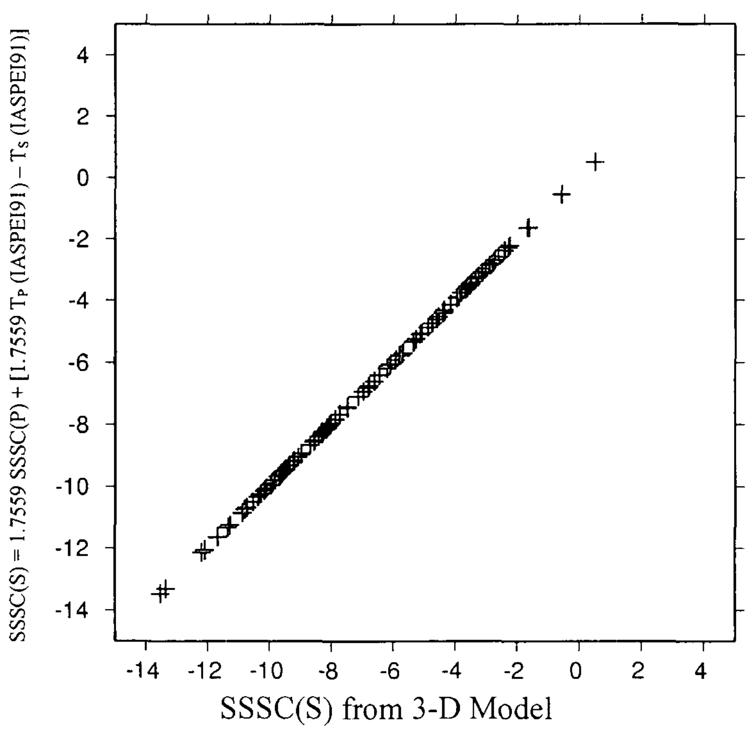

Figure 4-1. Comparison of the prediction of S-wave SSSCs for the region northeast of Borovoye based on the relationship of Equation 4-8 for a constant Poisson's ratio with those determined by raytracing through the 3-D velocity model.

SSSCs predicted by the relationship in Equation 4-8 with the S-wave SSSCs calculated using the raytracing algorithm through the 3-D S-wave velocity model along the 45° azimuth from station BRVK. The plot shows the SSSC predictions from Equation 4-8 on the vertical axis compared to the model-based SSSCs on the horizontal axis over the distance range from $3° \leq \Delta \leq 10°$. The comparison shows that the predicted SSSCs using the simple relationship based on a constant Poisson's ratio match almost exactly the times predicted by raytracing through the 3-D model over this distance range for this region. So, in regions where we can make this simple assumption on Poisson's ratio, we have a very simple alternative to predict the S-wave SSSCs. In particular, we do not need to do the additional raytracing for the S-waves; but instead we can use the P-wave SSSCs with the modification from Equation 4-8.

4.3 PRELIMINARY VALIDATION OF S-WAVE MODELS

We have conducted a number of preliminary analyses and tests to demonstrate the reasonableness and validity of the 3-D S-wave velocity models for several areas within the Group 1 study region. One such validation test was for the region around station Borovoye (BRVK). Figure 4-2a illustrates two great circle paths extending out to 20° at azimuths due east and northeast (45°) from BRVK. We used the PL raytracing algorithm and our 3-D S-wave velocity model to calculate the S-wave travel times along these profiles. The results are shown in Figure 4-2b. We see some differences in the travel times along the two profiles with apparent average S velocities (estimated by linear fits to the calculated travel times) of 4.44 km/sec along the due east profile and 4.66 km/sec along the northeast profile. In general, such differences look reasonable considering that we would expect somewhat slower S velocities along the east profile which runs partially through tectonically active areas.

In addition, we plotted S-wave travel times assembled by the IDG from FSU bulletin data for PNEs recorded at various stations of the Soviet permanent network. These are plotted in Figure 4-3 over the regional distance range out to 20°. We again fit a simple linear straight line relationship to these data and obtained an apparent Sn velocity of 4.65 km/sec. This is almost exactly equal to the apparent S velocity seen above in our model for the profile northeast from BRVK. So, the regional S-wave observations from the

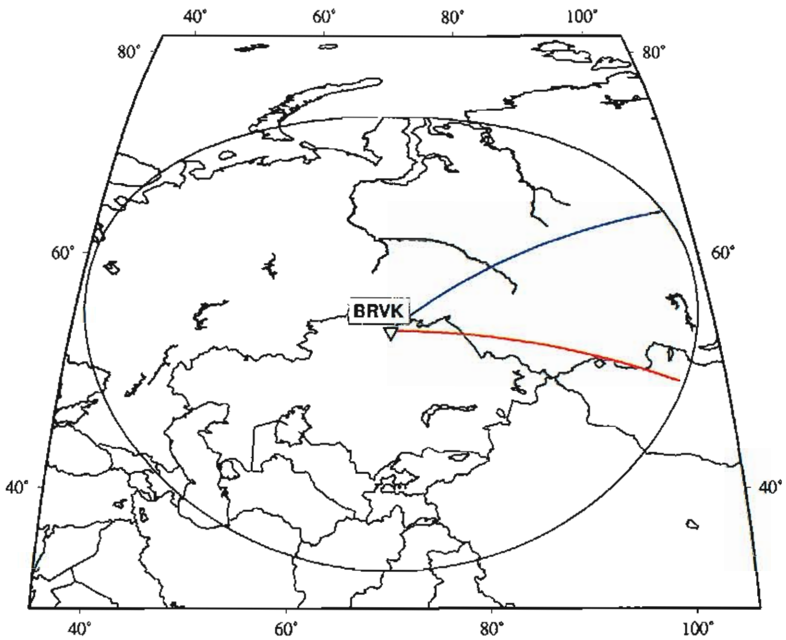

Figure 4-2a. Great circle paths extending out to 20° to the east (red) and to the northeast (blue) from the Borovoye station used for computing the S-wave travel times from the 3-D regional model.

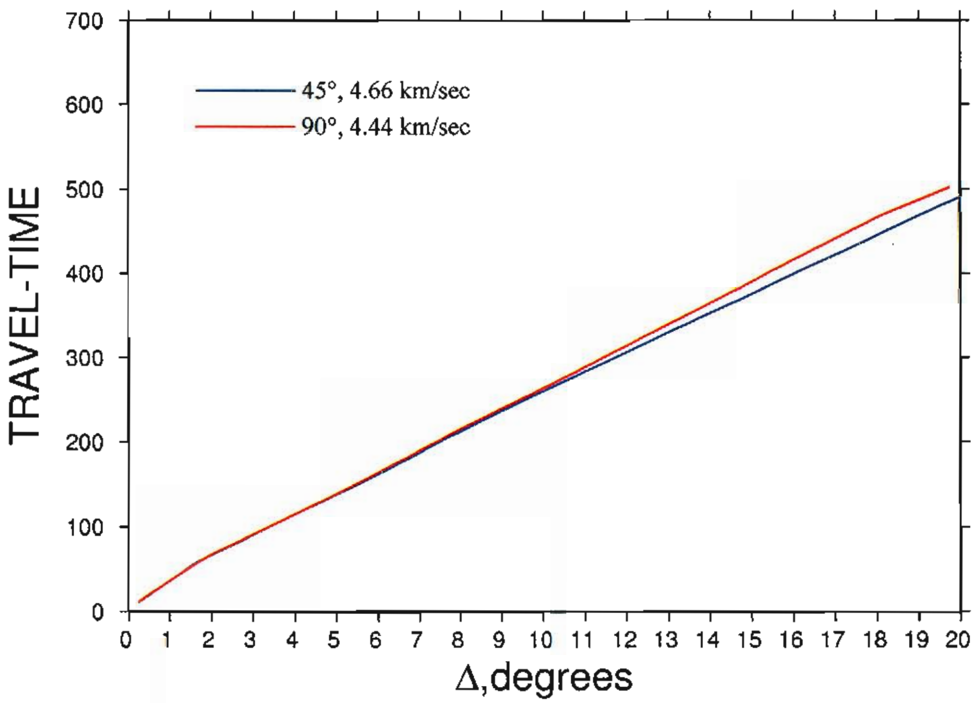

Figure 4-2b. S-wave travel time curves computed using the PL algorithm for profiles to the east (red) and northeast (blue) from the Borovoye station through the 3-D velocity model.

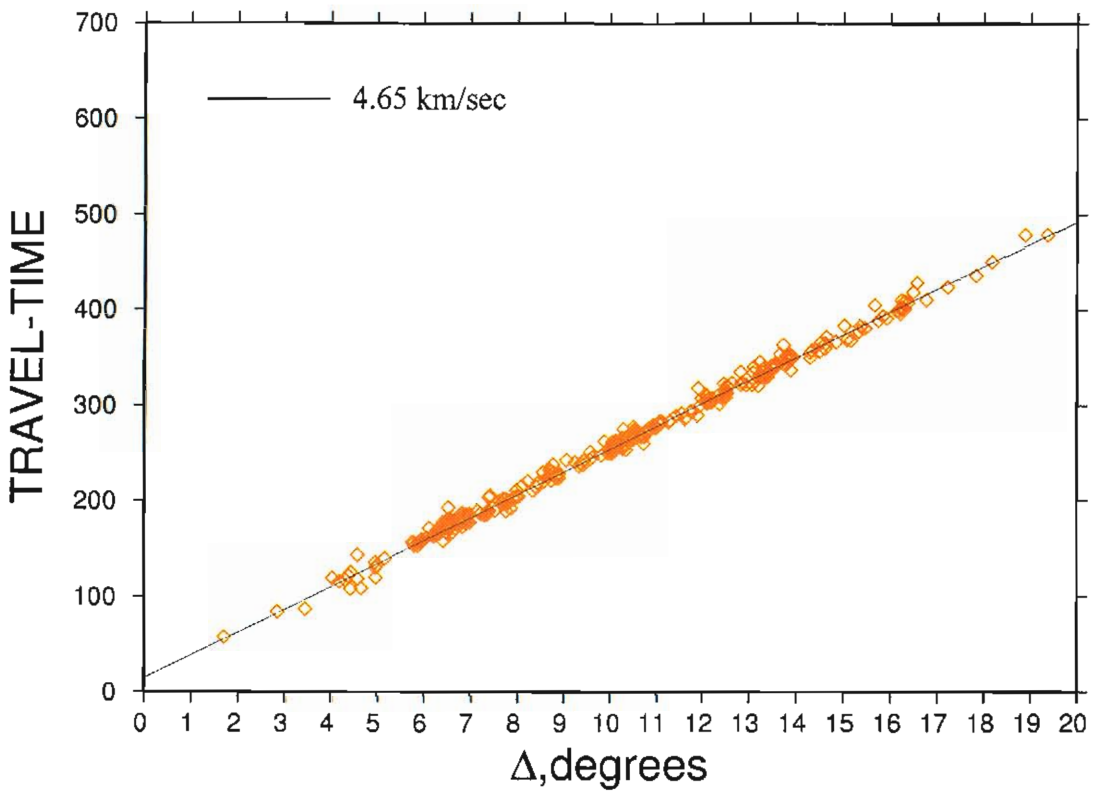

Figure 4-3. Observed Sn travel times versus distance for events recorded in the FSU from GT0 PNEs.

FSU PNEs appear to generally corroborate the Sn velocities predicted by our model from the region around BRVK.

In Figure 4-4 we show a more detailed comparison for the S-waves observed at Borovoye from FSU PNEs. We compare here the S-wave residuals with respect to IASPEI91 (on the left) and with respect to our 3-D S velocity model (on the right). We see that there is a very large negative bias ($\overline{\Delta t} = -8.83$ sec) for the observed S residuals relative to the IASPEI travel times. The bias is essentially removed ($\overline{\Delta t} = 1.54$ sec) by the 3-D S velocity model results seen in the right-hand figure. Although these data are limited, there do appear to be some systematic trends in the residuals with respect to the 3-D model which suggest that a more complete analysis, including a tomographic inversion to recover a spatially dependent Poisson's ratio, might be useful.

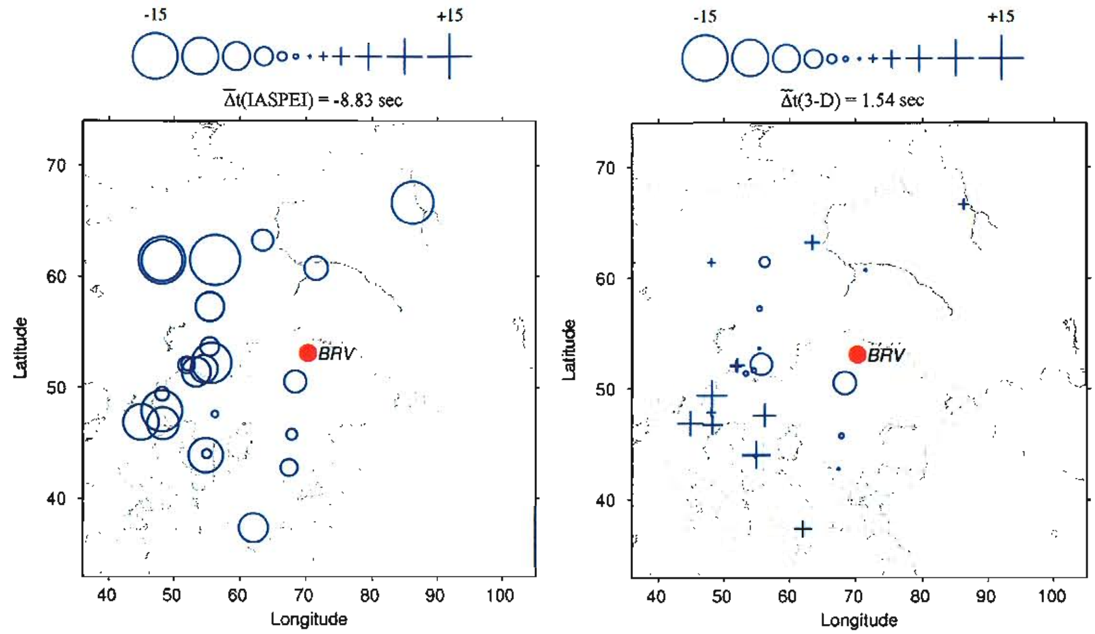

Figure 4-4. Comparison of S-wave travel time residuals at station Borovoye for PNEs measured with respect to IASPEI91 travel times (left) and with respect to our 3-D S-wave velocity model.

One thing that does seem clear at this point is that the variance in the S-wave arrival times will be significantly larger than that for P, even for a very good S-wave velocity model. For example, for this Borovoye sample, if we estimate the best-fitting average value of Poisson's ratio by averaging the observed ratios of S-to-P travel times and use this ratio to predict S-wave travel times from the observed P-wave travel times (as described above), the standard deviation of the difference between the predicted and observed S times is about 4 seconds, as opposed to about 1 second for the P-wave times predicted by our 3-D P-wave velocity model. This is the best that can be expected from a constant Poisson's ratio conversion from our P-wave model, and it suggests that S-wave arrival times should be significantly downweighted in the location process, at least for explosions.

A related problem common to all secondary phases is the ambiguity in determining onset times. This fact is illustrated in Figure 4-5, which shows a comparison of S-wave onset picks from regional PNE events recorded at Borovoye by very experienced analysts at

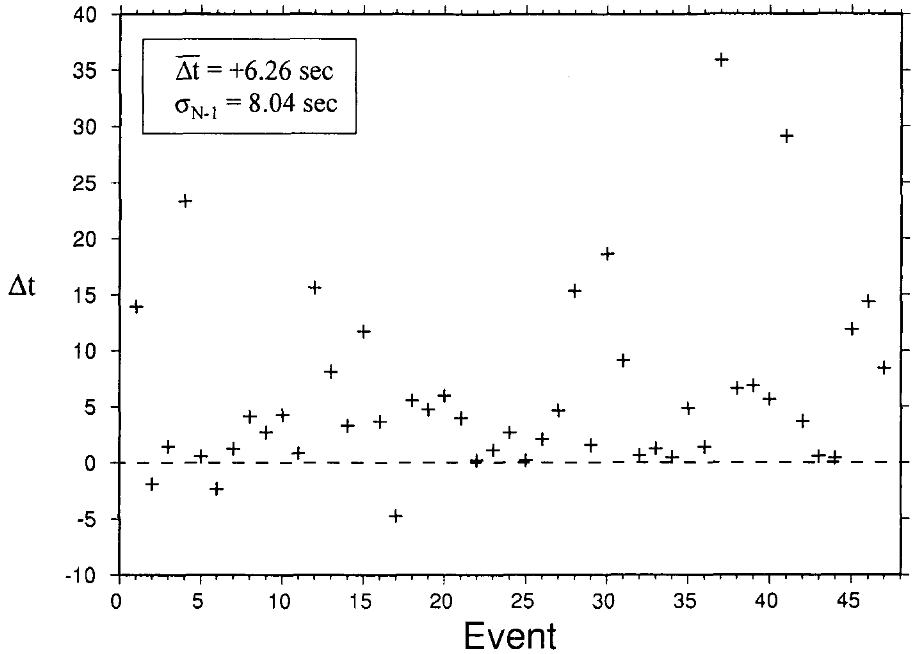

Figure 4-5. Comparison of differences in S-wave onset time estimates at station Borovoye by analysts from Lamont and from IDG for FSU PNEs.

Lamont and at the Russian IDG. Despite the fact that these are very senior analysts working with high-quality digital data, it can be seen that there are very significant differences, averaging more than 6 seconds, between the two sets of picks. This suggests that secondary phase travel time corrections will have to be very carefully calibrated to automatic processing and analyst procedures at the processing center of interest (e.g. IDG).

4.4 OTHER SECONDARY PHASES

As noted above, other secondary regional phases, including Pg and Lg, can also be useful for determining better seismic locations for small events, provided they are properly calibrated. For example, Figure 4-6 shows Pg and Lg travel times from FSU PNEs which would be useful in calibrating regional travel times for these phases at IMS stations from events in our Group 1 study region. As part of this project, we investigated the possibility of defining the travel-time corrections for these secondary regional phases by mapping the travel times of the first crustal arrivals through our P and S wave models

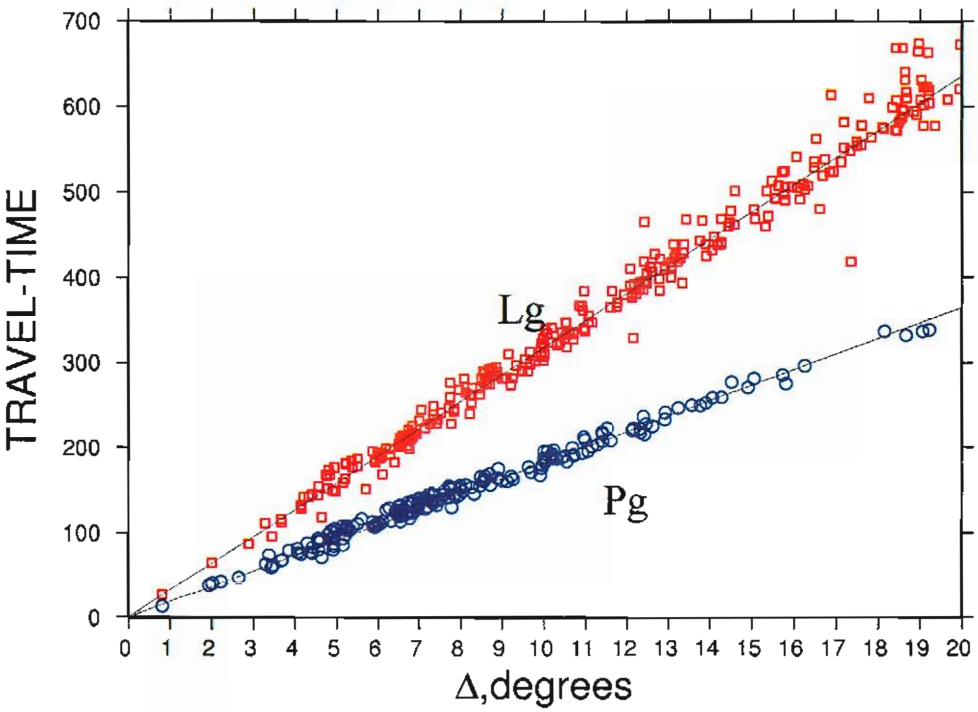

Figure 4-6. Observed secondary phase, Pg and Lg, travel times versus distance for GT0 PNEs from the FSU.

using the PL algorithm and "masking" out the upper mantle arrivals. Unfortunately, our initial studies found that the arrivals isolated by this approach appear to correspond to deep crustal refractions, which had group velocities inconsistent with the nominal observed Pg and Lg velocities and, consequently, were not obviously applicable to the definition of the travel time corrections for these phases.

We also looked at an alternate approach based on published results from various regional synthetic seismogram studies, which have indicated that the onset of the Pg and Lg arrival groups correspond to the Moho reflections PmP and SmS, respectively. Since the vertical P and S wave travel times through the IASPEI91 crustal model imply average P- and S-wave crustal velocities of about 6.1 and 3.5 km/sec, respectively, the predicted group velocities for these phases are consistent with the IASPEI91 travel time curves for

Pg and Lg. We believe that it should be feasible to adapt the PL algorithm to the estimation of PmP and SmS travel times through our 3-D model for use in the definition of SSSC surfaces for secondary phases, Pg and Lg. Such calibration corrections could make these regional phases much more valuable for seismic location of small events detected by limited numbers of regional stations. However, additional research will be required before such corrections can be reliably applied to observed Pg and Lg arrival time data.

It is also noteworthy that, as with the Sn discussion above, careful calibration will be needed to tailor any such Pg and Lg travel time corrections to specific applications. That is, the corrections proposed above strictly refer to the theoretical Pg and Lg onset times, which may be quite different from the Pg and Lg "arrival times" normally determined by analysts who typically focus on later, higher amplitude portions of the envelope of arrivals which define these phase observationally. This secondary phase pick uncertainty is illustrated in Figure 4-6 above which shows considerably greater scatter about the average lines than was seen for the Sn (cf. Figure 4-3), and even more clearly compared to the P-wave times.

SECTION 5

SSSCs FOR P AND S AT GROUP 1 IMS STATIONS

5.1 DETERMINATION OF SSSCs

The defined deliverables for this project are travel time corrections for each of the identified Group 1 IMS stations, implemented in the form of SSSCs, where the SSSC represents the difference (as a function of source location) between the travel times predicted by the derived earth model for the region and those predicted by the default IASPEI91 model. As part of our program efforts over the past year, we have recomputed the SSSCs based on our final 3-D velocity model for all 30 IMS seismic stations from the Group 1 study region. We have now computed and delivered digital versions of the SSSCs corresponding to both the P- and the S-wave travel time corrections (relative to IASPEI91) extending out to 20° from each station. These correction tables have been specified for surface focus plus 10 other focal depths (viz. 5, 10, 20, 30, 40, 50, 70, 100, 150, and 200 km).

Plots of the surface-focus SSSCs for all 30 Group 1 IMS stations are presented in the appendix to this report. In the subsections which follow, we describe some examples of the P- and S-wave SSSCs for selected Group 1 IMS stations. We also look at the depth dependence of the SSSCs and discuss the application of these corrections for use in event location in the Group 1 region.

5.2 EXAMPLES OF P-WAVE SSSCs FOR SELECTED GROUP 1 IMS STATIONS

At the conclusion of the second year of this research program, we prepared estimates of P-wave SSSCs for all 30 of the Group 1 IMS stations based on the existing 3-D velocity model for the region. As noted in the discussion above, there have been a number of revisions and refinements to the velocity model throughout this region as a result of continuing calibration efforts with additional ground truth data. In particular, the new model incorporates major changes to the China region, based on our formal tomographic analysis of the earthquake data from that region, as well as a number of minor changes in some other areas (e.g. WINPAK3D refinements and increased upper mantle velocities in some of the continental areas to the far east in the FSU, which had been formerly

represented by surface-wave models). The final 3-D regional velocity model for the entire Group 1 region of eastern Asia was assembled using the QUILT algorithm to compose the revised submodels, as described above. We then used the PL algorithm to compute the P-wave travel times through this composite 3-D model for distances out to 20° surrounding each of the IMS station sites for each of the assumed focal depths. The final SSSCs are then generated as the difference between these computed values and the corresponding P-wave travel times from the IASPEI91 tables.

Figures 5-1 through 5-5 show representative examples of the P-wave SSSCs for surface focus events at five selected IMS station sites in the Group 1 region of eastern Asia. We have plotted all of the SSSC values on a common color scale to facilitate comparisons. The first example is for station Borovoye (cf. Figure 5-1). The P-wave SSSC values at Borovoye vary from – 9.2 seconds to + 2.9 seconds. As one might expect, the corrections tend to be small close to the station; and the absolute values show a tendency to increase (i.e. corrections become more negative) with distance. In general, the corrections over much of the region surrounding Borovoye tend to be negative, which indicates that the 3-D model travel times are shorter than the corresponding IASPEI91 times. This means that the velocities in our 3-D model are generally higher than IASPEI91 1-D model velocities for much of this region. Some of the largest negative corrections occur at north and northwesterly azimuths (magenta colors in the plot). In general, the correction map for Borovoye appears quite reasonable and represents the expected behavior, in that the largest negative corrections are for paths which cross continental platform areas which tend to have higher than normal seismic velocities. In contrast, it also appears reasonable in Figure 5-1 that the corrections coming from the active tectonic area along the southern border of the FSU with China/Mongolia tend to be near zero or positive, because these path segments would tend to have velocities lower than normal. Although the SSSC corrections are strictly only valid out to 20°, the plots in this and subsequent figures extend to somewhat greater distances in the corners; and we see in these areas that the travel time corrections at larger distances tend to return to more nominal values (i.e. corrections closer to zero). This behavior also appears consistent with what we expect from the model, since at larger distances the travel times

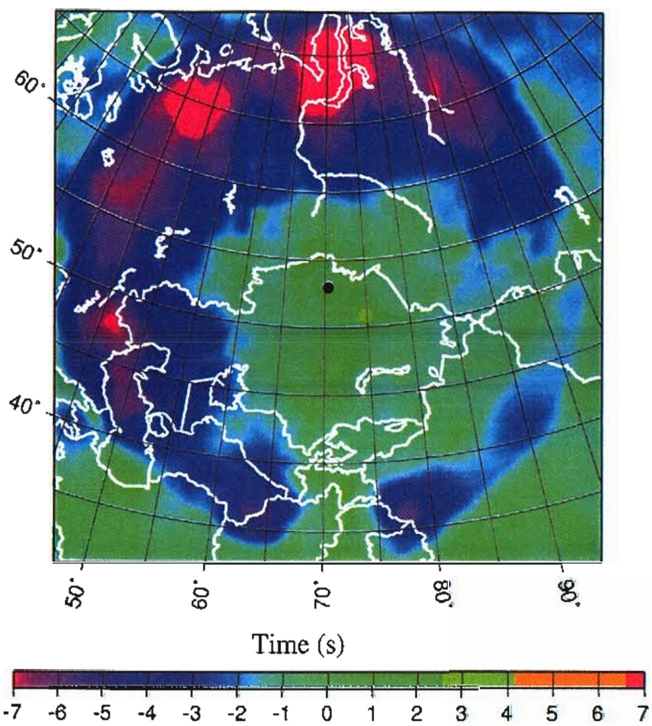

Figure 5-1. Estimated surface-focus P-wave SSSCs for the BRVK station site range from –9.2 seconds to +3.0 seconds.

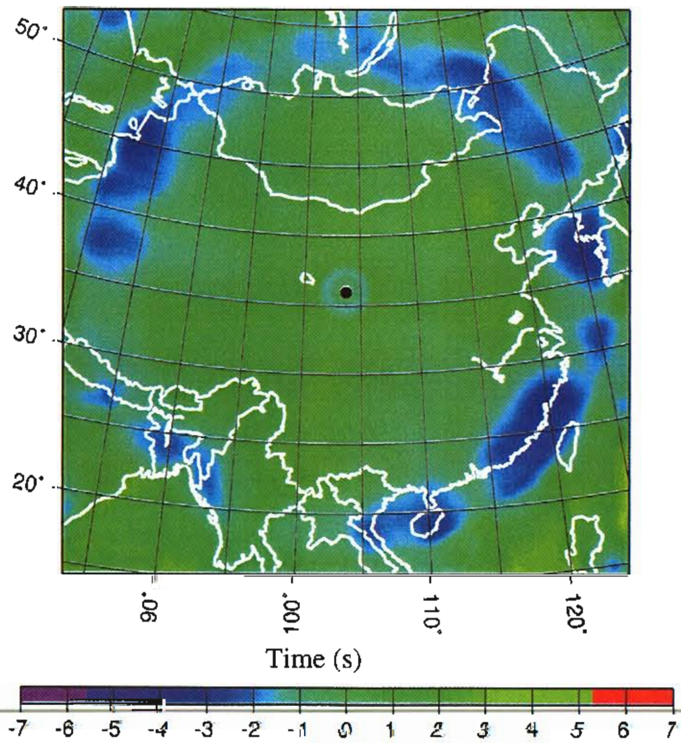

Figure 5-2. Estimated surface-focus P-wave SSSCs for the LZDM station site range from –3.2 seconds to +3.3 seconds.

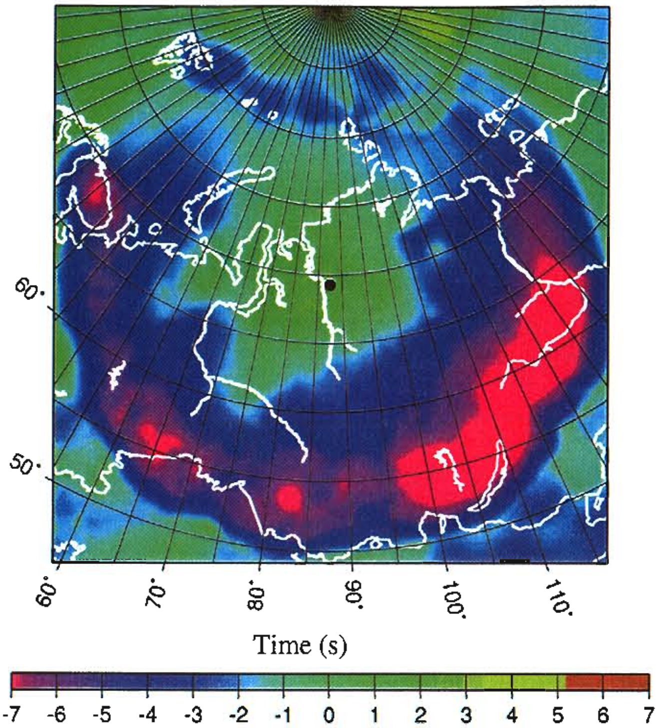

Figure 5-3. Estimated surface-focus P-wave SSSCs for the NRIK station site range from –8.9 seconds to +3.3 seconds.

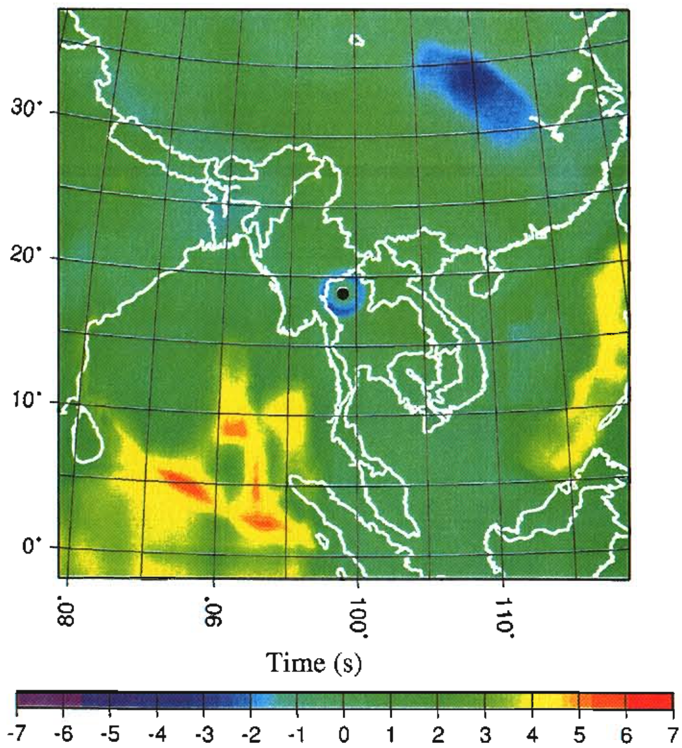

Figure 5-4. Estimated surface-focus P-wave SSSCs for the CMTO station site range from –2.9 seconds to +5.8 seconds.

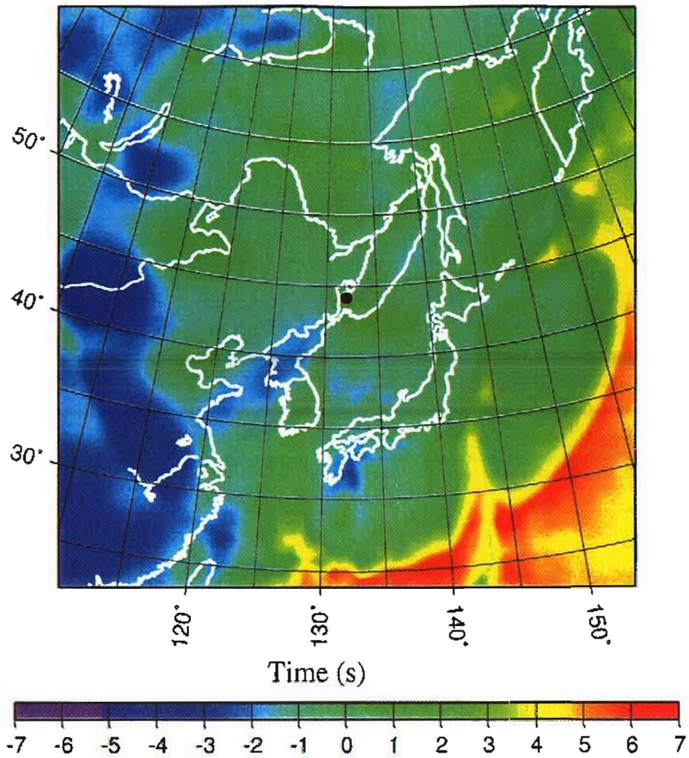

Figure 5-5. Estimated surface-focus P-wave SSSCs for the USK station site range from –4.6 seconds to +7.3 seconds.

are most affected by deeper parts of the model, which tend to return to IASPEI91 1-D values for rays bottoming near the 410-km discontinuity (i.e. below 410 km our 3-D model matches the IASPEI91 model).

Figure 5-2 shows a rather different behavior for the P-wave SSSC values from the region around the LZDM station site in central China. The predicted P-wave SSSC values for LZDM range only from – 3.2 seconds to + 3.3 seconds. We again see that values near the station are about zero and the absolute corrections again generally increase with distance over the range out to 20°. Largest negative corrections occur near the maximum regional distance. In general, the corrections around LZDM appear to be rather uniform and do not show great differences on average with respect to IASPEI91 (i.e. correction values tend to average near zero over much of the region). However, there again appears to be some evidence of a swath across the southwestern border of China where the

correction values near 20° appear to be less negative. This again would seem to be consistent with generally lower velocities for paths across this tectonically active zone.

Figure 5-3 shows the surface-focus P-wave SSSCs from the region around station Norilsk (NRIK) in northern Russia. In this case the SSSC values range from – 8.9 seconds to 3.3 seconds. Values near the station are again near zero with some positive values in the nearer regional distance ranges. The largest negative corrections occur near the farther limits of the regional distance range to the southeast and south. In general, most of the raypaths from sources in these areas tend to be across the platform areas of the FSU; so the model velocities in these areas tend to be higher than IASPEI91 in these areas producing the expected negative SSSCs. In this case, the tendency for the tectonic areas along the FSU southern border with Mongolia to have less negative correction values is not apparent, perhaps because the corresponding zone of lower velocities, which we expect in this area, is too close to the far extreme of the paths from this area and producing only a minor effect on the travel times. One result, which gives some confidence in these SSSC predictions, can be seen by comparing Figure 5-3 with Figure 5-1 for the path between the two station locations. First, looking at the SSSC value in Figure 5-3 for station NRIK from a potential event at the earth's surface near the location of station BRVK, the correction value is approximately – 6 seconds (i.e. violet in the color scale). Next, looking at Figure 5-1 for station BRVK from a potential event near the location of station NRIK, the correction value is again approximately – 6 seconds. So, the SSSC corrections calculated from the models for these two reciprocal paths are about the same, as we would expect from the prediction scheme.

Figure 5-4 and 5-5 show two additional examples of the surface-focus P-wave SSSCs predicted by the model for stations CMTO in Thailand and USK in eastern Russia. For CMTO the SSSCs are in the range from – 2.9 seconds to + 5.8 seconds, and for USK the SSSCs are in the range from – 4.6 seconds to + 7.3 seconds. Values close to the stations in both cases are again near zero. The corrections with the most negative values for both of these stations are for continental paths at the largest regional distances. In particular, most negative values in Figure 5-4 occur in a relatively limited area to the northeast of station CMTO at 17° to 20°; and in Figure 5-5 the most negative values occur in a wide

arc to the west of USK again at regional distances from about 17° to 20°. A significant difference in the SSSC plots in Figures 5-4 and 5-5 is the occurrence of relatively large positive values from events with paths through the oceanic areas surrounding these stations. Thus, for station CMTO we see large positive SSSC values from locations in oceanic areas to the southwest and to the far east; and for station USK there are large positive SSSC values from location in the oceanic areas to the far southeast. These SSSC prediction results again would appear to be consistent with what we expect from our general 3-D model, which we know to have low velocities relative to IASPEI91 in oceanic areas.

5.3 EXAMPLES OF S-WAVE SSSCs FOR SELECTED GROUP 1 IMS STATIONS

In Section 4 we described the procedures used to generate the 3-D S-wave velocity model from the P-wave model. The final S-wave 3-D velocity model was then used as input to the PL algorithm again to calculate the S-wave travel times out to 20° from each of the 30 IMS station sites in the Group 1 area for each of the assumed focal depths. The S-wave SSSCs for each station were then computed as the difference between the travel times from the 3-D regional model and the corresponding S-wave travel times from the IASPEI91 tables.

In Figures 5-6 through 5-8, we show some representative examples of the S-wave SSSCs for surface focus events at three selected IMS station sites from the Group 1 region of eastern Asia. Again all of the plots are on a common color scale to facilitate comparisons, although the scale for the S waves is different from that shown above for P waves to show the greater range in the S-wave corrections. The first plot is for station Borovoye (cf. Figure 5-6). The S-wave SSSCs predicted by our model have values at Borovoye from – 29.5 seconds to + 5.4 seconds. As seen in the plot, the values are close to zero near the station and the absolute values generally increase with distance away from the station. The most negative corrections occur to the north and northwest at far regional distances. The plot for the S-wave SSSCs in Figure 5-6 again shows evidence of the low-velocity tectonic zone along the southern border of the FSU with China/Mongolia in the form of a swath of somewhat more positive correction values.

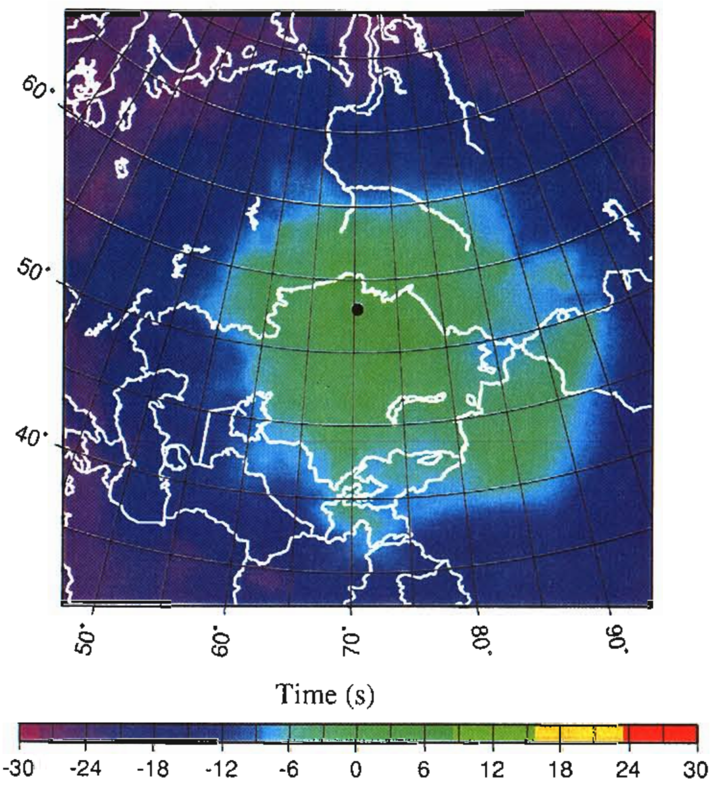

Figure 5-6. Estimated surface-focus S-wave SSSCs for the BRVK station site range from –29.5 seconds to +5.4 seconds.

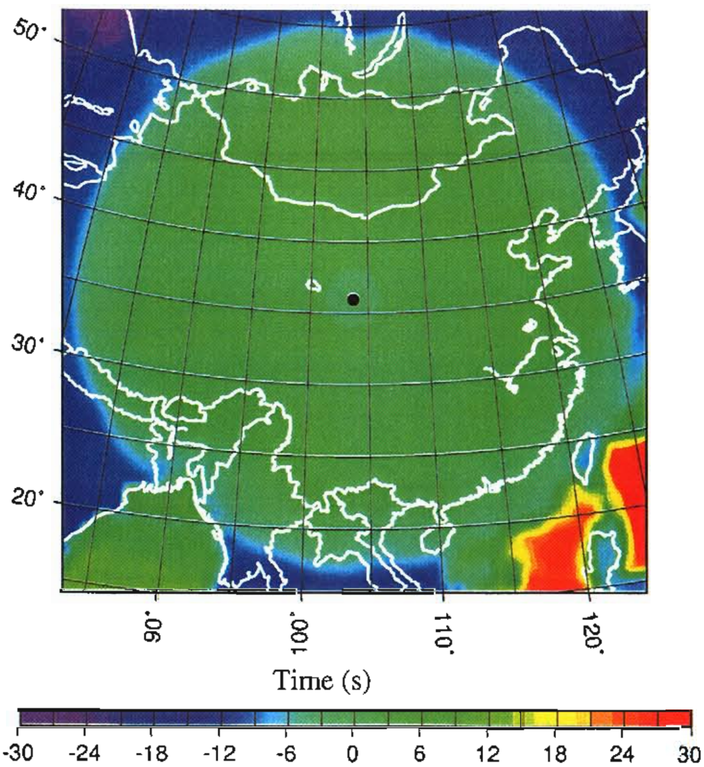

Figure 5-7. Estimated surface-focus S-wave SSSCs for the LZDM station site range from –25.6 seconds to +46.9 seconds.

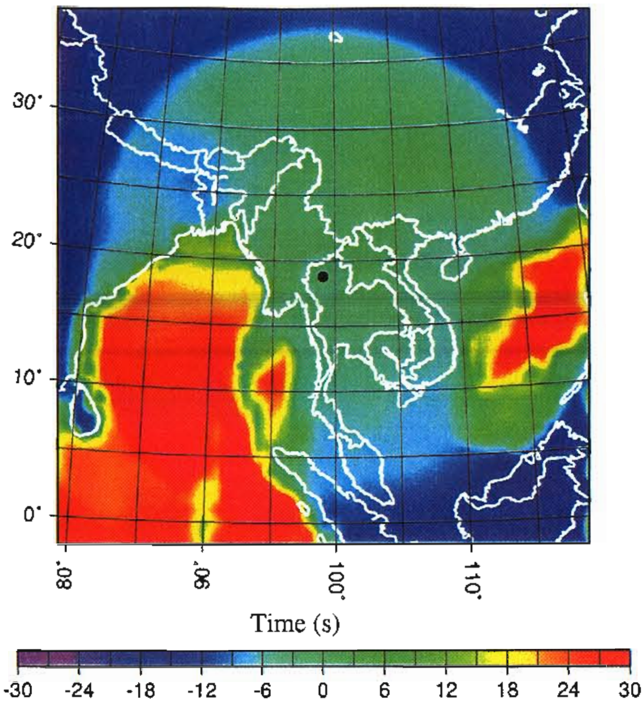

Figure 5-8. Estimated surface-focus S-wave SSSCs for the CMTO station site range from –24.1 seconds to +42.1 seconds.

The S-wave SSSC plot in Figure 5-7 for station LZDM in central China exhibits much the same kind of uniformity that we saw above for the P-wave SSSCs at this station. Although the predicted surface-focus S-wave SSSCs for LZDM range from – 25.6 seconds to + 46.9 seconds, the extreme positive and negative values all come from the corners of the plot beyond the 20° regional distance range. In fact, within the 20° range we see that the predicted S-wave SSSCs are quite moderate (in the range from about – 9 seconds to + 9 seconds) and there are only minor fluctuations.

Figure 5-8 shows the surface-focus S-wave SSSCs for station CMTO in Thailand. The correction values range from – 24.1 seconds to + 41.2 seconds. The values are near zero at the station and show greater differences as we get to greater regional distances. The SSSCs tend to have zero or more negative values for locations in the continental areas to the north and from the shallow oceanic areas directly south. Large positive SSSCs occur for locations from the oceanic areas to the southwest and to the far east. These again

appear to be reasonable for these regions because of the low model velocities in these oceanic regions, where velocities are significantly lower than the IASPEI91 1-D model velocities.

5.4 DEPTH DEPENDENCE OF SSSCs

As noted above, a significant advantage of our model-based approach over purely statistical methods for predicting SSSCs is that we can develop the travel time corrections over a range of potential focal depths for sources in the region. For each of the 30 IMS stations, we have used our SSSC prediction scheme to predict the SSSCs for not only focal depths at the earth's surface but also for 10 additional depths within the crust and upper mantle (0 km ≤ h ≤ 200 km).

Plots of the SSSCs at stations in some of the platform regions do not show very strong depth dependence, while greater dependencies are seen at several of the stations for events with sources near tectonic boundaries with sharp velocity contrasts. We illustrate the behavior of the depth dependence of the SSSCs for sample plots at selected source depth intervals as determined for the P waves at station PRPK at Nilore in Pakistan. The region surrounding station PRPK includes some fairly strong tectonic boundaries, such as the tectonic plate convergence zone in the Pamir-Hindu Kush area just to the north of the station.

Figures 5-9 through 5-12 show the P-wave SSSCs at PRPK for source depths of 0 km, 10 km, 30 km, and 100 km, respectively. The P-wave SSSCs at PRPK for regional surface focus sources vary from – 7.3 seconds to + 5.3 seconds. As with the other SSSC plots, the correction values for source locations closest to the station are small. The correction values tend to be negative or zero over large parts of the region surrounding PRPK, and some of the largest negative corrections occur out near the regional distance margins (e.g. strong negative anomaly in the area to the east of the Caspian Sea in Turkmenistan). Over these paths the 3-D model travel times are shorter than the corresponding IASPEI91 times, and the corresponding velocities in our 3-D model are generally higher than IASPEI91 1-D model velocities. However, a remarkable feature of the PRPK SSSCs in Figure 5-9 is the strong positive corrections (with values near 5

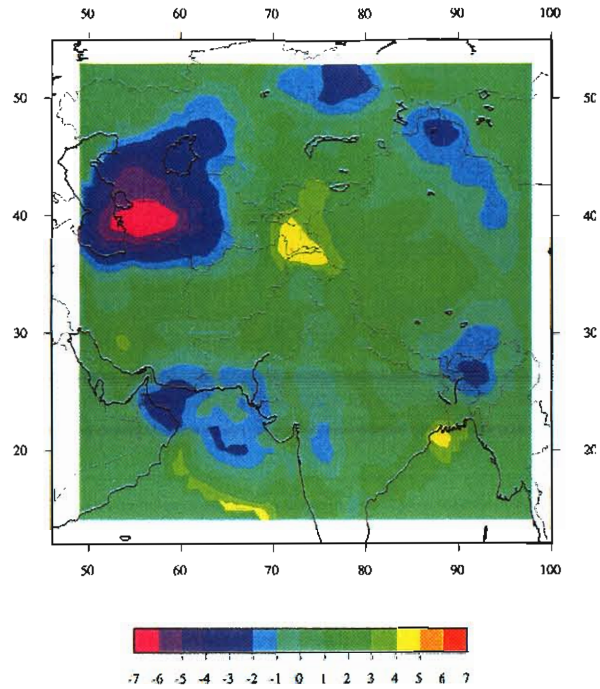

Figure 5-9. Estimated P-wave SSSCs at the PRPK station site for regional events with focal depths at the earth's surface range from –7.3 seconds to +5.3 seconds.

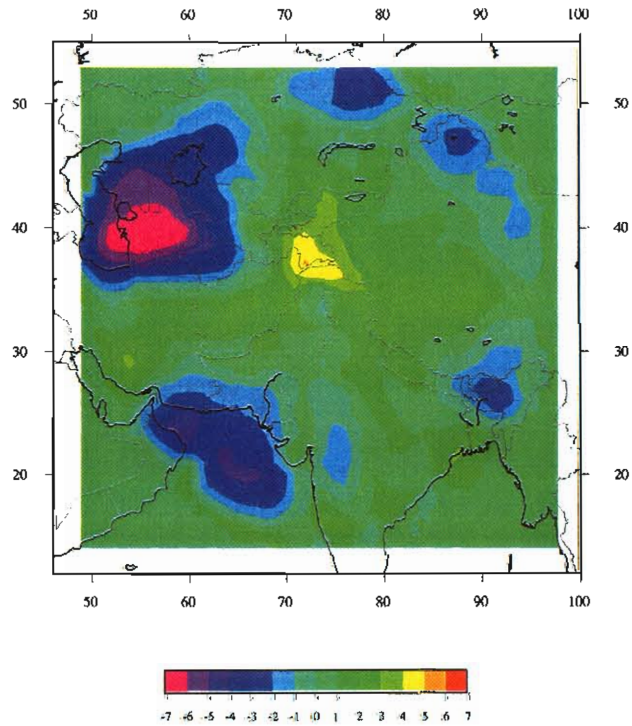

Figure 5-10. Estimated P-wave SSSCs at the PRPK station site for regional events with focal depths of 10 km range from –7.4 seconds to +5.1 seconds.

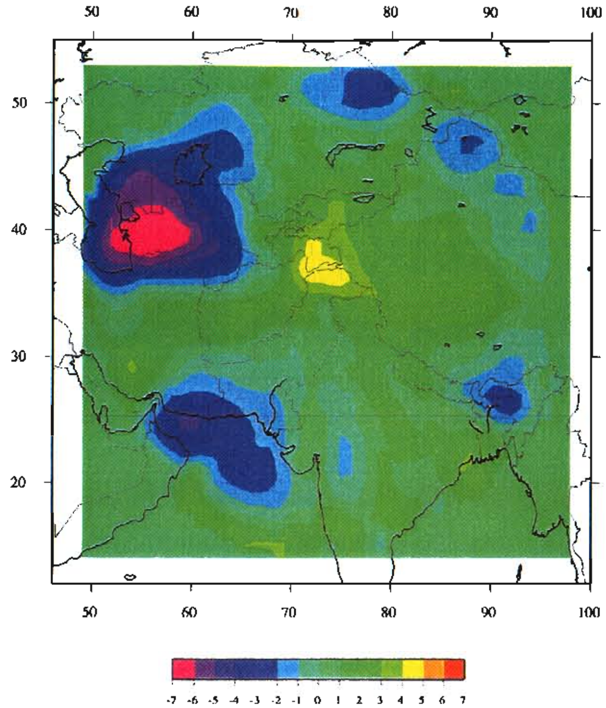

Figure 5-11. Estimated P-wave SSSCs at the PRPK station site for regional events with focal depths of 30 km range from –7.2 seconds to +4.9 seconds.

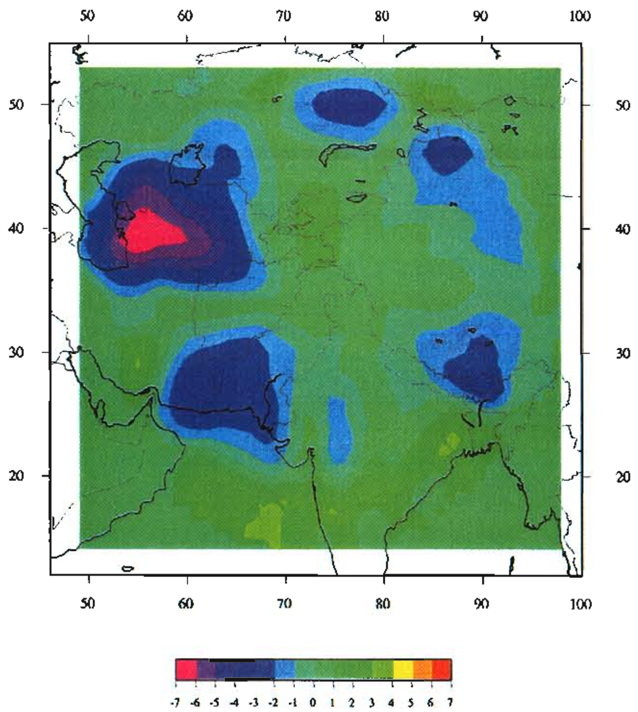

Figure 5-12. Estimated P-wave SSSCs at the PRPK station site for regional events with focal depths of 100 km range from –7.1 seconds to +3.6 seconds.

seconds) to the north in the Pamir-Hindu Kush region of Tadzhikistan. For these regions the travel times predicted by our 3-D model are significantly larger than the IASPEI91 times, and the velocities in our model are thus much slower than in the IASPEI91 model. Furthermore, we note in comparison to the SSSC plots at other source depths that there are some strong variations in the predicted corrections for sources in the Pamir-Hindu Kush region and in the vicinity of the India/Pakistan coast. Although the maximum and minimum SSSCs are about the same in the plots for sources with focal depths of 10 km and 30 km in the earth's crust, there are some significant differences in the correction values at specific locations. In particular, across the region surrounding PRPK differences in the predicted SSSCs between focal depths of 0 km and 10 km are as great as 2.5 seconds in some places. For sources with subcrustal depths, the positive correction anomaly in the Hindu Kush area has nearly vanished. In general, the difference in the SSSCs between a surface focus event and one with a subcrustal focal depth in the Hindu Kush area would be expected to be as great as 2-3 seconds.

Comparisons like those in Figures 5-9 through 5-12 indicate that application of SSSC correction terms from a fixed or incorrect focal depth could lead to substantial errors in the travel time measurements at the stations where they are applied. Such erroneous travel times can lead to significant location errors particularly for smaller events located with limited station networks. This is also important because erroneous travel times at stations in the near-regional distance range can also produce significant errors in estimates of event focal depth (cf. Murphy et al., 2000, 2002), which often plays a key role in event identification. Therefore, we believe that additional work is warranted to establish and refine SSSC correction and location procedures to account for these potential effects of focal depth differences.

SECTION 6

APPLICATION OF A NEW KRIGING ALGORITHM TO ESTIMATE EMPIRICAL SSSCs AT IMS STATIONS

6.1 JOINT LOCATION/CALIBRATION INVERSE PROBLEM

Our approach to seismic calibration determines two types of travel-time functions: a model-based function and an empirical correction function. The model-based travel-time function depends on three variables: the event location, $\mathbf{x}$, the station location, $\mathbf{y}$, and a vector of model parameters that describe the velocity structure of the Earth, which we will denote $\mathbf{m}$. Thus, we can write model-based times as $T(\mathbf{x},\mathbf{y};\mathbf{m})$. Empirical corrections, in general, depend on $\mathbf{x}$, $\mathbf{y}$ and a parameter vector $\mathbf{a}$: $C(\mathbf{x},\mathbf{y};\mathbf{a})$. The role of $\mathbf{a}$ is analogous to that of $\mathbf{m}$, except how T depends on $\mathbf{m}$ is determined by ray theory and is not a matter of choice, whereas the function C is ad hoc and so the definition of $\mathbf{a}$ and how C depends on $\mathbf{x}$, $\mathbf{y}$ and $\mathbf{a}$ are a matter of choice.

The problem of seismic calibration is that of determining $\mathbf{m}$ and $\mathbf{a}$. Our approach has been to find both vectors by solving an inverse problem involving arrival time data from multiple events and stations, including where possible the IMS station we wish to calibrate. To describe our approach, we consider here the basic version of this problem with first P arrival times observed for a subset of paths between m events and n stations:

$$d_{ij} = t_i + T(\mathbf{x}_i,\mathbf{y}_j;\mathbf{m}) + C(\mathbf{x}_i,\mathbf{y}_j;\mathbf{a}) + e_{ij}. \qquad (6\text{-}1)$$

In this equation

- d_{ij} is the observed arrival time for the (i,j)th path.
- t_i and $\mathbf{x}_i$ are origin parameters (time and hypocenter, respectively) of the ith event.
- $\mathbf{y}_j$ is the location of the jth station.
- e_{ij} is an observational (picking) error in d_{ij}.

If any of the m events in this inverse problem are earthquakes, or explosions with imperfect origin information, then the origin parameters of these events are additional unknowns of the inverse problem. Therefore, Equation 6-1 in general describes a joint

inverse problem whose unknowns are **m**, **a**, and $(\mathbf{x}_i, t_i)$, $i = 1, \ldots, m$. As part of this problem we include appropriate constraints that embody whatever ground-truth information is available on the event origin parameters.

We have solved this inverse problem geographic area by area, and for a given area, in two steps. The first step is tomography, in which **a** is fixed (or the empirical corrections are ignored altogether), and the Earth model, **m**, is fit to the data. In India-Pakistan, we have also allowed earthquake location parameters to vary (i.e., earthquake tomography). In the second (post-tomography) step, we solve Equation 6-1 for **a** with **m** and the event locations fixed to their tomographic results. In this second step, it is useful to replace the arrival time data with corresponding post-tomography residuals, defined as

$$r_{ij} = d_{ij} - t_i - T(\mathbf{x}_i, \mathbf{y}_j; \mathbf{m}) \tag{6-2}$$

and write the inverse problem for **a** as

$$r_{ij} = C(\mathbf{x}_i, \mathbf{y}_j; \mathbf{a}) + e_{ij}. \tag{6-3}$$

The remainder of this section focuses on the choice of **a** and the estimation of **a** from Equation 6-3.

6.2 STATION-SPECIFIC EMPIRICAL CORRECTIONS

6.2.1 PARAMETERIZATION

The traditional approach to empirical travel-time corrections defines a separate correction function for each station. That is, there is no functional dependence on the station location. The simplest parameterization of station-specific corrections comprises a time term, a_j, for each station, such that

$$C(\mathbf{x}, \mathbf{y}_j) = a_j. \tag{6-4}$$

This choice eliminates the dependence on event location as well, which is not an adequate parameterization for spatially well-distributed events. However, it is the parameterization used in many multiple-event location methods (e.g., Jordan and

Sverdrup, 1981), which apply to small clusters of events, and we mention it for this reason.

Schultz et al. (1998) developed an empirical calibration approach in which a station-specific correction function is assigned to each station:

$$C(\mathbf{x},\mathbf{y}_j) = a_j\,(\mathbf{x}). \tag{6-5}$$

In this case, the inverse problem of equation (6-3) becomes

$$r_{ij} = a_j(\mathbf{x}_i) + e_{ij}\,. \tag{6-6}$$

This problem decouples by stations since no connection is assumed between the correction functions for different stations. For any given station, the problem is one of spatial interpolation, whereby the function $a_j(\mathbf{x})$ is fit to samples observed at various points, $\mathbf{x}_i$ (the event locations). Schultz et al (1998) solved this interpolation problem using the method of kriging. Kriging finds an optimal fit to the sample values under prior constraints in the form of statistical properties of the function a_j, as expressed by a correlation function.

6.2.2 APPLICATION TO POST-TOMOGRAPHY DSS RESIDUALS

We have applied station-specific kriging to the final travel-time residuals resulting from Pn tomography in the DSS region of eastern Asia. Tomography was performed in two sub-areas: one centered on station BRV, which we will refer as the "western DSS" area, and the other centered 35 degrees longitude east of BRV ("eastern DSS"). We applied kriging to the post-tomography residuals from each area separately, even though many stations were involved in both tomographies.

We used the 2-D "block kriging" program KB2D from the free software library GSLIB (Deutsch and Journel, 1998) to obtain the station-specific travel-time correction function for each station. Each correction function is 2-D, i.e. a function of geographic position (event epicenter) but not event depth. Since KB2D works in a Cartesian geometry, event

latitudes and longitudes were, for each station, converted to a station-centered Cartesian system. The KB2D input parameters we used were

- An exponential type correlation function: $\sigma_0^2 \exp(-|\mathbf{x}|L)$
- Correlation distance: $L = 400$ km
- Prior standard deviation: $\sigma_0 = 1.5$ sec
- Data standard deviations:
  - 0.5 sec for residuals from PNE events
  - 1.0 sec for residuals from earthquakes

We show the station-specific kriging results for the five stations for which the most data were available: BRV, ELT, NVS, SVE and OBN. Figure 6-1 shows two correction functions for station BRV. The result on the left of the figure used the 227 residuals at BRV (from 48 PNE's and 179 earthquakes) obtained from the western DSS tomography.

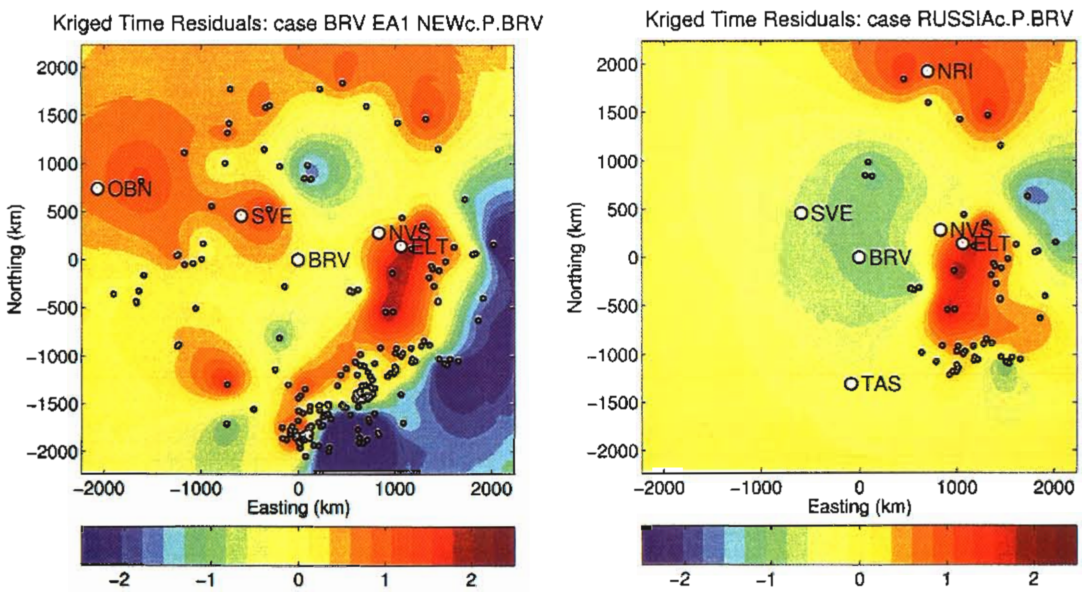

Figure 6-1. Correction functions for station BRV, obtained by station-specific kriging with GSLIB. A correction function was determined from the residuals from the western DSS tomography (left) and eastern DSS tomography (right). Locations of the events in each data set are shown as small circles. Five stations in the region are shown for reference.

The result on the right used the 59 BRV residuals (46 PNEs, 13 earthquakes) from the eastern DSS tomography. The results are similar except the western DSS correction function (Figure 6-1 left) has an area of large negative values in the southeast, not present in the eastern DSS version (right of figure). This is probably due to the fact that the eastern DSS data set excluded most of the earthquakes, some of which had negative residuals as large as - 5.0 sec.

For the other four stations we show only the correction functions obtained from the western DSS residuals. Figure 6-2 shows the travel-time correction functions for ELT (left) and NVS (right), which are to the east of BRV. The correction functions for these two stations are similar, which is expected since the stations are separated by only 267 km. However, it is difficult to know whether the differences that we do see (e.g. approximately 1 sec near station SVE) are significant, or whether they are artifacts of the different event sets used (35 PNEs for ELT, 26 PNEs for NVS) or, for the events in common, differences between the observational errors at the two stations. Figure 6-3 shows the kriged correction functions for stations SVE and OBN, two stations to the west of BRV. These results are less similar to each other, but the separation between SVE and OBN is much greater than ELT/NVS.

Another difficulty, apparent by comparing the correction functions for all five stations, has to do with source-receiver reciprocity. If the travel-time corrections embodied in these functions are the result of Earth structure effects absent from our tomographic models, the correction functions should be source-receiver reciprocal. Thus, the correction predicted for station ELT from a shallow event located where NVS is should be the same as the correction for NVS from an event located at ELT. We see from Figure 6-2 that this is nearly the case. Comparing Figures 6-1 (left) and 6-2, we also see that BRV/NVS reciprocity is obeyed within about 0.5 sec. However, BRV/ELT reciprocity is violated by more than 1.5 sec. Reciprocity between BRV and SVE is also violated by more that 1.5 sec (Figure 6-1 versus 6-3). Finally, we point out that the SVE correction function predicts a correction of about - 1.5 sec at the location of SVE itself. This too is non-physical.

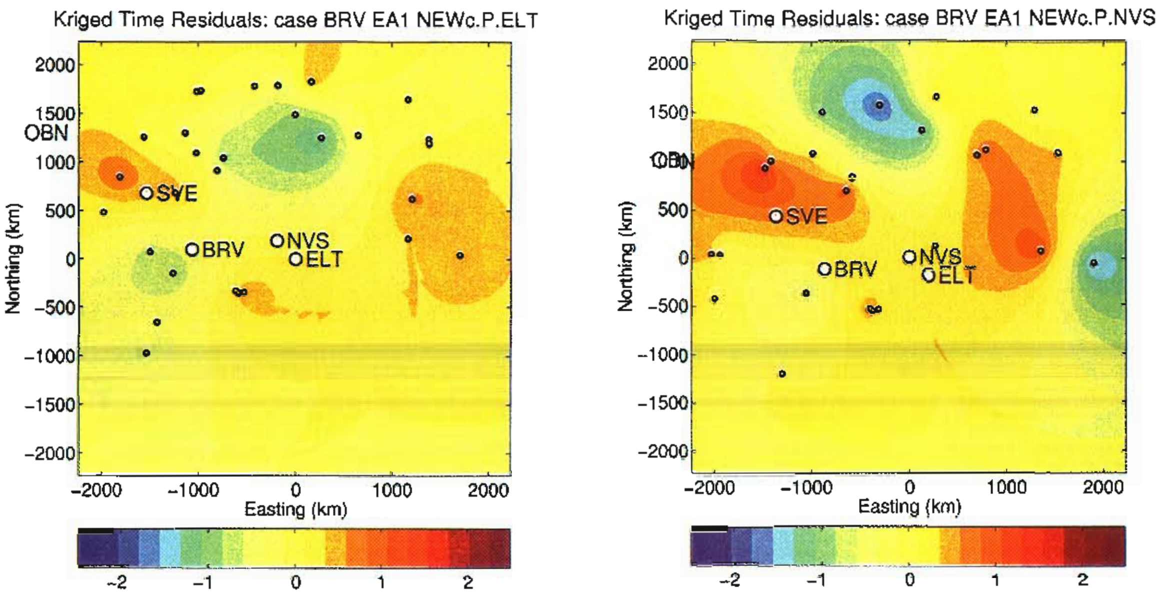

Figure 6-2. Correction functions for stations ELT (left) and NVS (right), each obtained by station-specific kriging of the western DSS residuals.

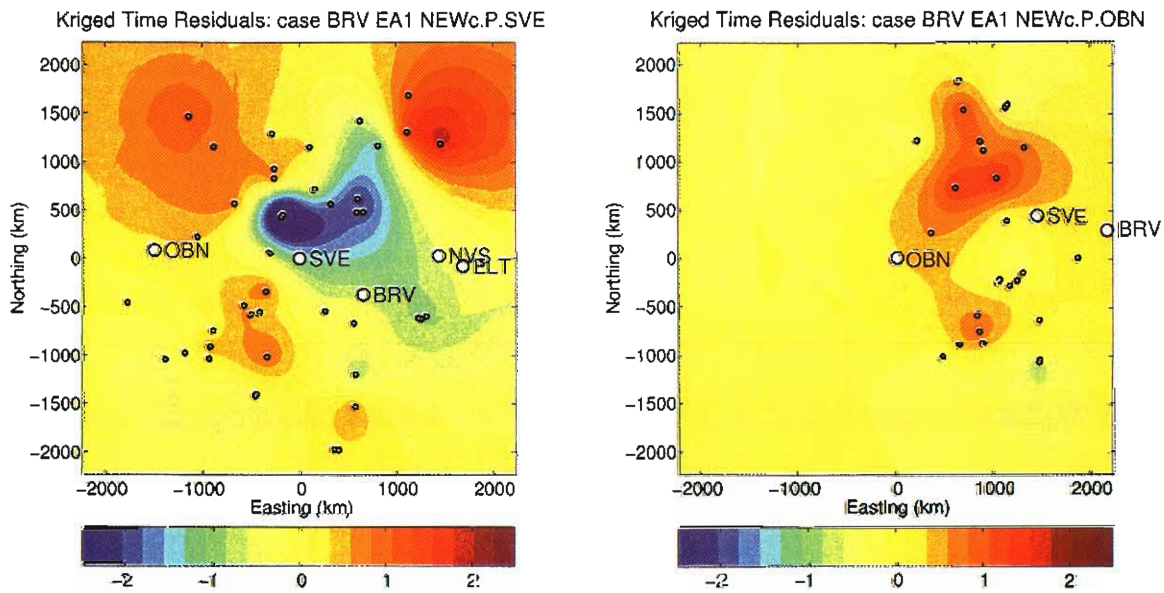

Figure 6-3. Correction functions for stations SVE (left) and OBN (right), each obtained by station-specific kriging of the western DSS residuals.

Table 6-1 compares statistics of the travel-time residuals at the 5 stations, before (prior) and after (posterior) kriging. We see that, in all cases, the posterior mean residual at each station (with either data set) is essentially zero, and the posterior standard deviation (RMS) has been reduced significantly from its prior value.

Table 6-1: Residual Statistics for Station-Specific Kriging of DSS Residuals

Station	No. Data	Mean (s)		Std. Deviation (s)	
		Prior	Posterior	Prior	Posterior
		—Western DSS—			
BRV	227	−0.059	−0.023	1.456	0.629
ELT	35	0.005	0.003	0.714	0.326
NVS	26	0.098	−0.001	1.070	0.367
SVE	49	−0.148	0.003	1.473	0.494
OBN	29	0.289	−0.002	0.840	0.382
		—Eastern DSS—			
BRV	59	0.138	−0.038	1.218	0.513
ELT	35	0.022	0.003	0.700	0.330
NVS	26	0.174	0.003	0.982	0.320
SVE	11	−0.179	0.000	1.597	0.396

6.3 MULTIPLE-STATION EMPIRICAL CORRECTIONS

6.3.1 PARAMETERIZATION

Rodi et al. (2002, 2003) have developed a new approach to empirical calibration that fits correction functions to a multiple-event, multiple-station data set, such as is used in tomographic model development. The key new element of the approach is the parameterization of path corrections with a universal underlying function (or set of functions), analogous to the velocity model in tomography. Such parameters are not specific to any particular station or event, and generate a correction for an arbitrary path.

For application to calibration in eastern Asia, we have considered three such parameterizations. One is a time-term function, a, which yields the correction for a path between event location $\mathbf{x}$ and station locations $\mathbf{y}$ as

$$C(\mathbf{x},\mathbf{y}) = a(\mathbf{x}) + a(\mathbf{y}). \tag{6-7}$$

The parameter vector, **a**, appearing in Equations 6-1 and 6-3, would in this case be synonymous with the function a or, in practice, samples of this function on a dense grid. It is clear that the time-term function generates reciprocal travel-time corrections, since **x** and **y** can be interchanged in Equation 6-7.

Another parameterization we have considered is a time-factor function, whereby

$$C(\mathbf{x},\mathbf{y}) = [a(\mathbf{x}) + a(\mathbf{y})]\ T(\mathbf{x},\mathbf{y}) \tag{6-8}$$

where $T(\mathbf{x},\mathbf{y})$ is the model-based travel-time for the path. In this case, the correction is proportional to the travel-time itself. This parameterization also yields reciprocal path corrections, and it obeys another physical property of travel-times in that the correction for a path goes to zero as its length goes to zero:

$$\lim_{|\mathbf{x}-\mathbf{y}| \to 0} C(\mathbf{x},\mathbf{y}) = 0. \tag{6-9}$$

The third, and last, parameterization we have considered is a mislocation-vector function, $\mathbf{a}(\mathbf{x})$, for which

$$C(\mathbf{x},\mathbf{y}) = \mathbf{p}(\mathbf{x},\mathbf{y}) \cdot \mathbf{a}(\mathbf{x}) + \mathbf{q}(\mathbf{x},\mathbf{y}) \cdot \mathbf{a}(\mathbf{y}). \tag{6-10}$$

Here, **p** is the gradient of the model-based travel-time with respect to the event location, while **q** is the gradient with respect to the station location:

$$\mathbf{p} = \nabla_1 T(\mathbf{x},\mathbf{y}) \tag{6-11}$$

$$\mathbf{q} = \nabla_2 T(\mathbf{x},\mathbf{y}). \tag{6-12}$$

(∇_k means gradient with respect the kth argument of a function.) Each is a slowness vector pointed in the direction of the raypath, and each depends on both **x** and **y** since the raypath depends on the location of both its endpoints. The interpretation of **a** as a mislocation vector follows from the fact that Equation 6-10 is the first order change in

travel-time that results from perturbing the event location by $\mathbf{a}(\mathbf{x})$ and the station location by $\mathbf{a}(\mathbf{y})$.

Since T is a reciprocal function of its arguments, we have

$$\mathbf{p}(\mathbf{x},\mathbf{y}) = \mathbf{q}(\mathbf{y},\mathbf{x}). \tag{6-13}$$

Therefore, the mislocation-vector parametrization also generates travel-time corrections that are source-receiver reciprocal. Further, as the raypath shrinks to zero the correction goes to zero since $\mathbf{p} + \mathbf{q}$ goes to zero.

Station-specific correction functions can be defined from these universal parameter functions. In the case of Equation 6-10, for example, they are simply

$$a_j(\mathbf{x}) = \mathbf{p}(\mathbf{x},\mathbf{y}_j) \cdot \mathbf{a}(\mathbf{x}) + \mathbf{q}(\mathbf{x},\mathbf{y}_j) \cdot \mathbf{a}(\mathbf{y}_j). \tag{6-14}$$

This points up an important advantage of universal parameterizations such as those above. They define a correction function for a station at any location, whether or not the station has observed travel-time residuals to constrain the function. This is accomplished by allowing correlations between the corrections among stations and between stations and events.

6.3.2 MAXIMUM-LIKELIHOOD KRIGING

The estimation of universal parameter functions from observed travel-time residuals is an inverse problem which is a generalization of the interpolation problem encountered in the station-specific approach. For example, with the time-term parameter function, the inverse problem of Equation 6-3 becomes

$$r_{ij} = a(\mathbf{x}_i) + a(\mathbf{y}_j) + e_{ij}. \tag{6-15}$$

This problem (and those for the other parameter functions) can be solved with geo-statistical constraints, as used in conventional kriging. We do so by adopting a maximum-likelihood (ML) approach to the inverse problem, instead of the minimum-variance approach used in conventional kriging. For Gaussian data errors, the ML

approach takes the solution of Equation 6-15 to be the function a that minimizes the objective function given by

$$\Psi = \sum_{ij} | r_{ij} - a(\mathbf{x}_i) - a(\mathbf{y}_j) |^2 / \sigma_{ij}^2 + \int a(\mathbf{x})[Da](\mathbf{x}) d\mathbf{x} \tag{6-16}$$

where σ_{ij} is the assigned standard deviation of e_{ij} and D is a specified differential operator. This is very similar to our approach to solving the tomography problem, but now we choose D differently. The maximum-likelihood inversion approach is equivalent to conventional kriging with a given correlation function when D is the inverse of the covariance operator that corresponds to the correlation function (see Rodi et al, 2003).

In our applications to date, we have used the following operator for kriging in N spatial dimensions (N = 1, 2 or 3):

$$D = \frac{\text{const}}{\sigma_0^2} \left[\delta(\mathbf{x}) - \frac{1}{2\ell - N} \left(L_x^2 \frac{\partial^2}{\partial x^2} + L_y^2 \frac{\partial^2}{\partial y^2} + L_z^2 \frac{\partial^2}{\partial z^2} \right) \right]^\ell \tag{6-17}$$

where σ_0^2 is a prior variance of the parameter function and L_x, L_y and L_z are correlation lengths in the x, y and z directions of a local Cartesian coordinate system. Various choices of the operator order, ℓ, correspond to correlation functions that are commonly used in conventional kriging, e.g. the exponential correlation function (ℓ = 1 in 1-D, ℓ = 2 in 3-D) and Gaussian correlation function $(\ell \to \infty)$. While we have expressed this operator in Cartesian coordinates, we have actually implemented it as a difference operator in a global, spherical coordinate system. We solve the maximum-likelihood criterion (Ψ = minimum) for a sampled version of the function a on a latitude/longitude/depth grid. Numerically, the minimization is performed with a conjugate gradients technique.

6.3.3 APPLICATION TO POST-TOMOGRAPHY DSS RESIDUALS

We applied the multiple-station kriging approach to the travel-time residuals resulting from the two DSS tomographic applications. This time, unlike the station-specific application, we pooled the data from the two sub-areas (western and eastern DSS),

yielding a data set with 1026 travel-time residuals from 261 events and 70 stations. We applied the multiple-station kriging method to these data to estimate parameter functions of the three types described above: time-term, time-factor and mislocation-vector functions. We estimated 2-D (no depth dependence) and 3-D versions of each. The geo-statistical parameters we used were similar to those used for station-specific kriging:

- Correlation order: $\ell = 2$ (exponential correlation in 3-D).
- Lateral correlation distance: $L_x = L_y = 400$ km.
- Vertical correlation distance: $L_z = 40$ km (for 3-D functions).
- Prior parameter errors:
  - Time terms: $\sigma_0 = 1.5$ sec
  - Time factors: $\sigma_0 = 0.01$
  - Mislocation vectors: $\sigma_0 = 5$ km

These prior errors are roughly equivalent when mapped to travel-time corrections. The picking errors we assumed were the same as before: 0.5 sec for PNE data and 1.0 sec for earthquake data.

Figure 6-4 shows the 2-D time-term (top) and time-factor (bottom) parameter functions derived with multiple-station kriging of the DSS residuals. We recall that a travel-time correction for any path is defined from the time-term function (top of figure) by summing the value of the function sampled at the event and station locations. The time-factor function (bottom) is similarly sampled at two points, but the sum is multiplied by the model-based travel-time to obtain a travel-time correction. We see that these two parameter functions have a similar spatial dependence when fit to the DSS residuals. Figure 6-5 shows the three components of the 2-D mislocation-vector function. These define a travel-time correction for a path in terms of the first-order travel-time perturbation that results by moving the end-points of the path by the amount and direction indicated by the mislocation vector.

Figures 6-6 and 6-7 through 6-9 show 3-D versions, at three depths, of the time-term and mislocation-vector parameter functions derived from the DSS residuals.

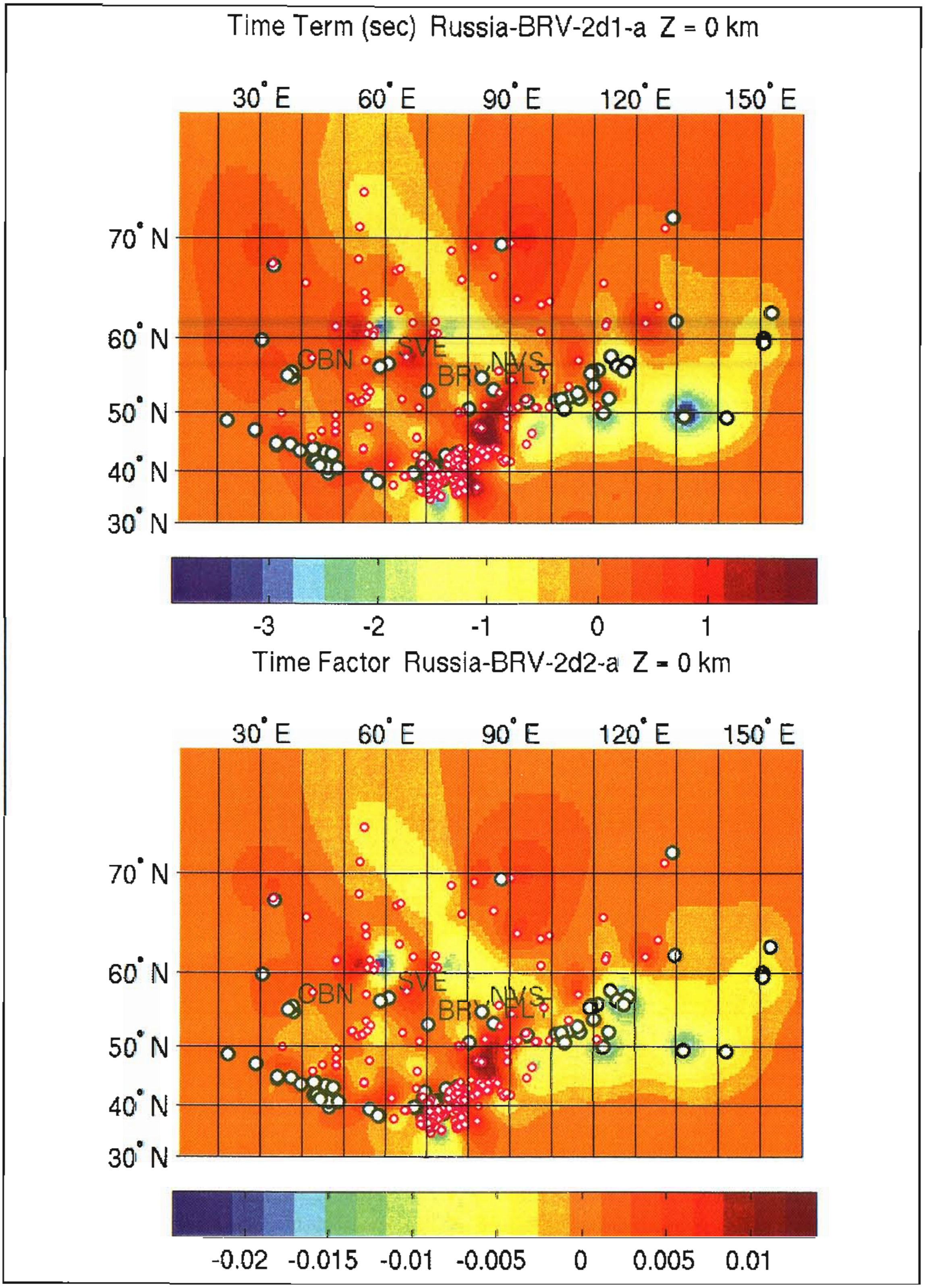

Figure 6-4. 2-D time-term (top) and time-factor (bottom) parameter functions for DSS, obtained by multiple-station kriging. Small circles mark event locations in the DSS data set and large circles mark the station locations (five are labeled).

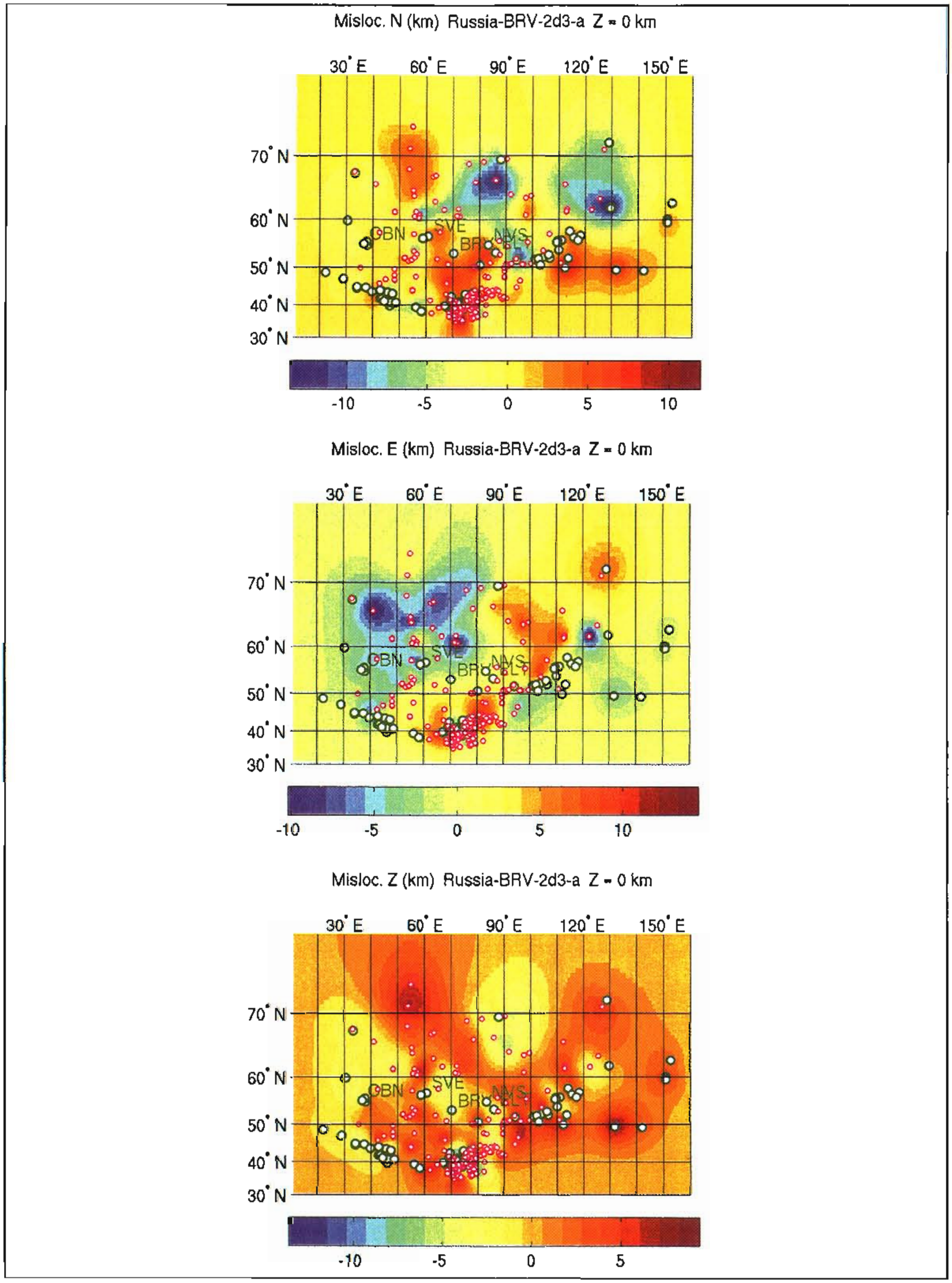

Figure 6-5. 2-D mislocation-vector function for DSS: north (top), east (middle), and depth (bottom) components.

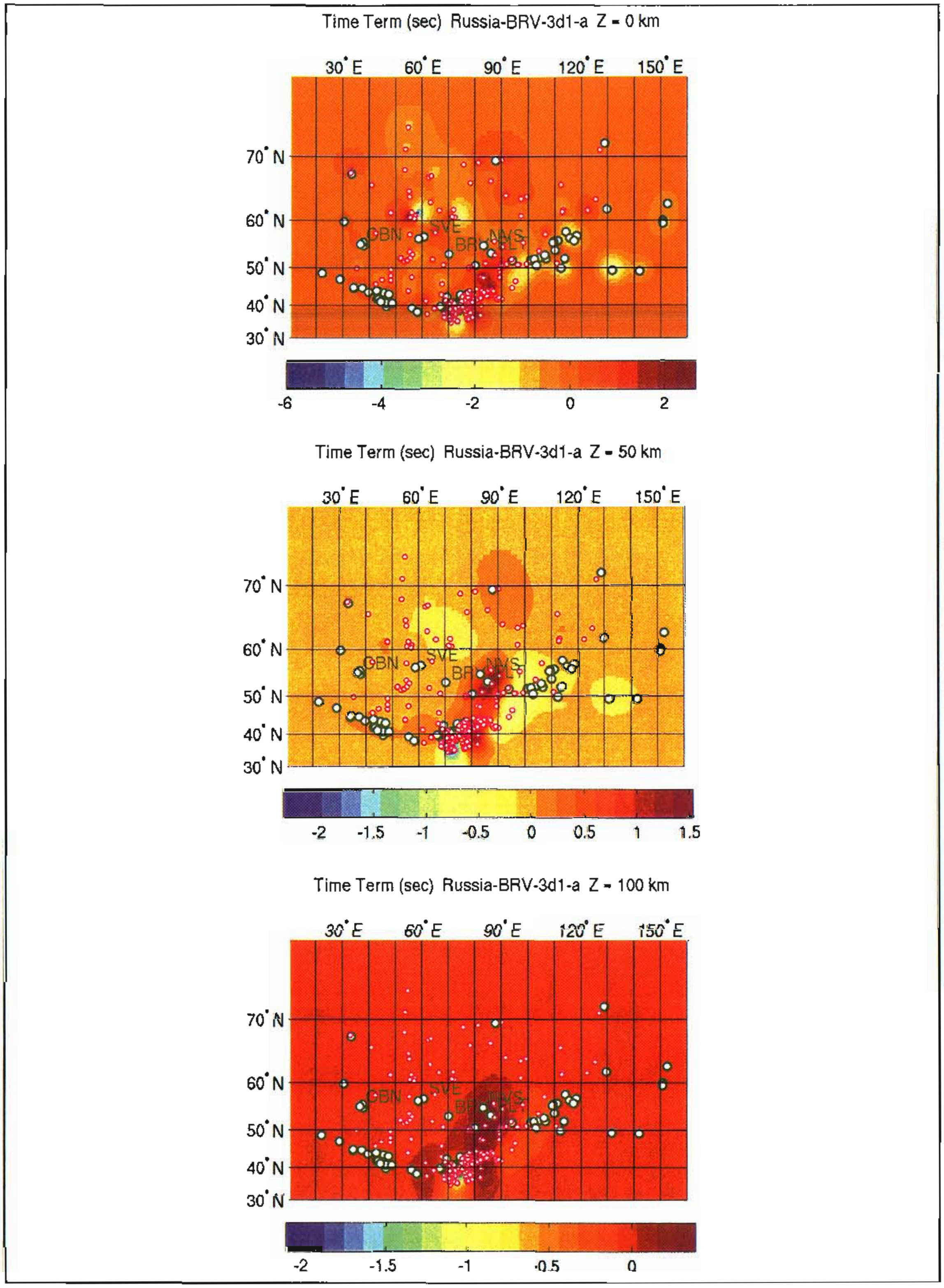

Figure 6-6. 3-D time-term function for DSS, at depths of 0 km (top), 50 km (middle), and 100 km (bottom).

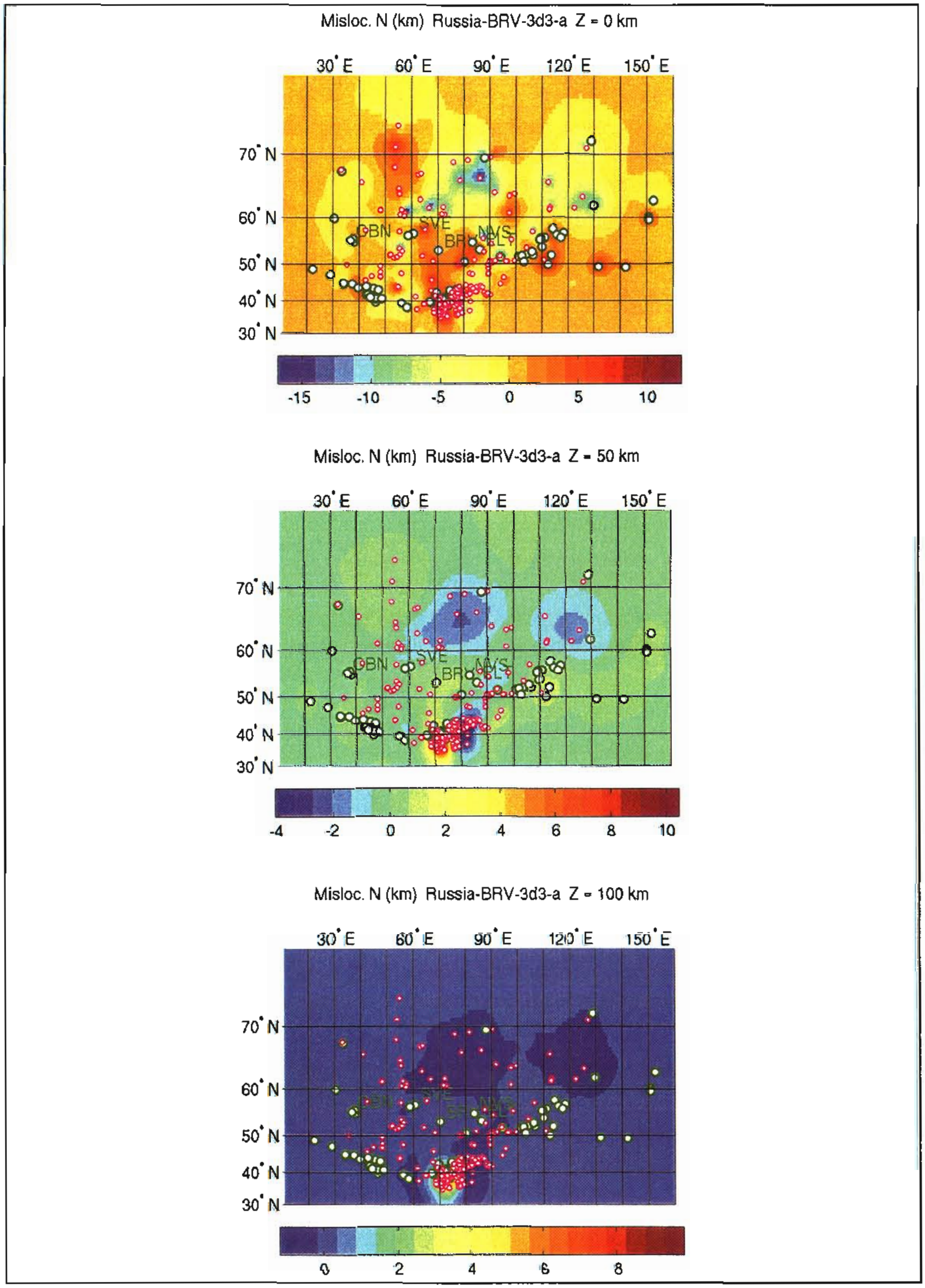

Figure 6-7. 3-D mislocation-vector function for DSS: north component at depths of 0 km (top), 50 km (middle), and 100 km (bottom).

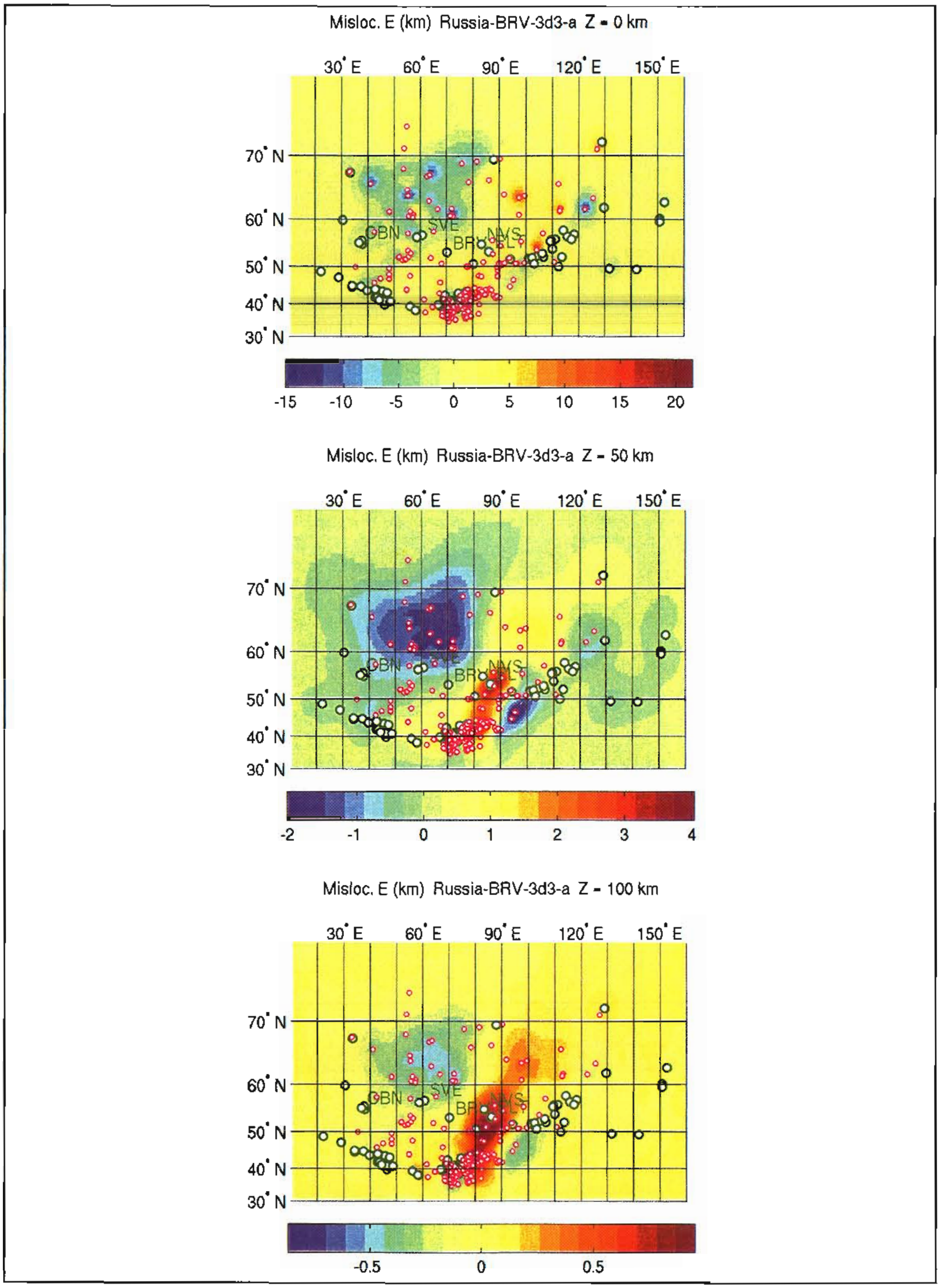

Figure 6-8. 3-D mislocation-vector function for DSS: east component at depths of 0 km (top), 50 km (middle), and 100 km (bottom).

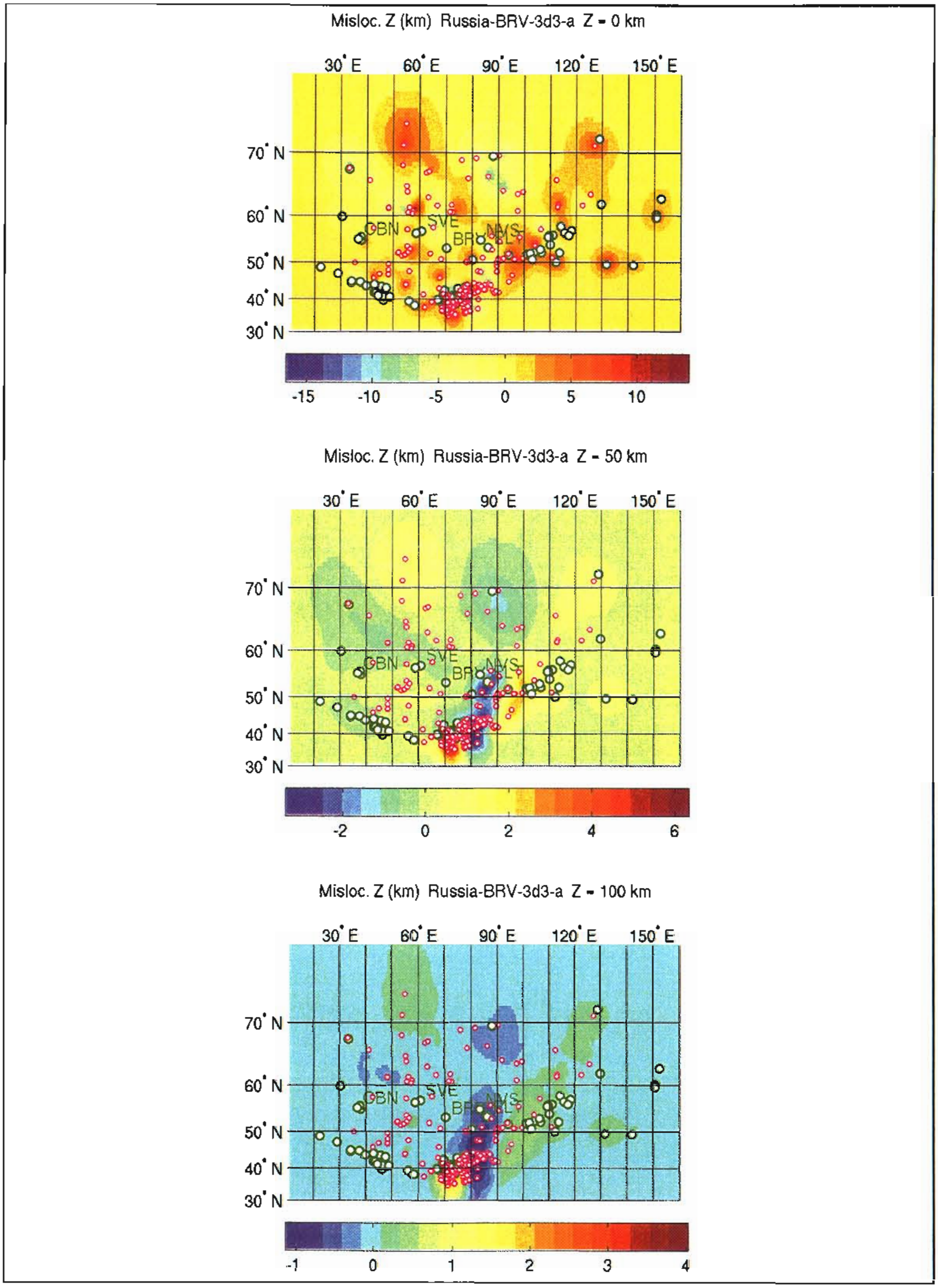

Figure 6-9. 3-D mislocation-vector function for DSS: depth component at depths of 0 km (top), 50 km (middle), and 100 km (bottom).

Table 6-2 shows the posterior standard deviations (RMS) achieved by each of the parameter functions. These can be compared to the prior RMS for the pooled DSS residuals, which is 1.223 sec. The time-term and time-factor functions, both the 2-D and 3-D versions, yield relatively large posterior RMSs, especially when compared to station-specific kriging (Table 6-1). This is not unexpected because, in these cases of multiple-station kriging, there is one parameter function fitting the data from all stations, rather than one per station as in station-specific kriging. Even when the universal function is 3-D, there are insufficient degrees of freedom to reduce variances significantly. The mislocation-vector parameterization, on the other hand, fits three functions to the data (the vector components) and we see from Table 6-2 that this provides enough degrees of freedom to achieve a significant RMS reduction. While still not as good as the station-specific case, the multiple-station results are presumably much more stable by having fewer free parameters.

Table 6-2: Posterior RMSs for Multiple-Station Kriging of DSS Residuals

Prior RMS = 1.223 sec; Number of data = 1-26

	Time-Term	Time-Factor	Misloc.-Vector
2-D	0.934	0.932	0.791
3-D	0.904	0.898	0.692

As noted earlier, each parameter function we have derived defines a travel-time correction function for each station, i.e. the correction for all event locations and a fixed station location (see Equation 6-14) We show these for station BRV, as derived from four of the parameterizations, in Figure 6-10 We see that the different parameterizations, while they yield varying posterior RMSs, are not distinctly different. Apparently, each captures the key features of the DSS residual patterns for BRV, but with differing fidelity. Figure 6-11 compares the 2-D mislocation-vector version to the station-specific function for BRV. The one notable difference is that the area of large negative corrections southeast of BRV is absent in the multiple-station function (left). This

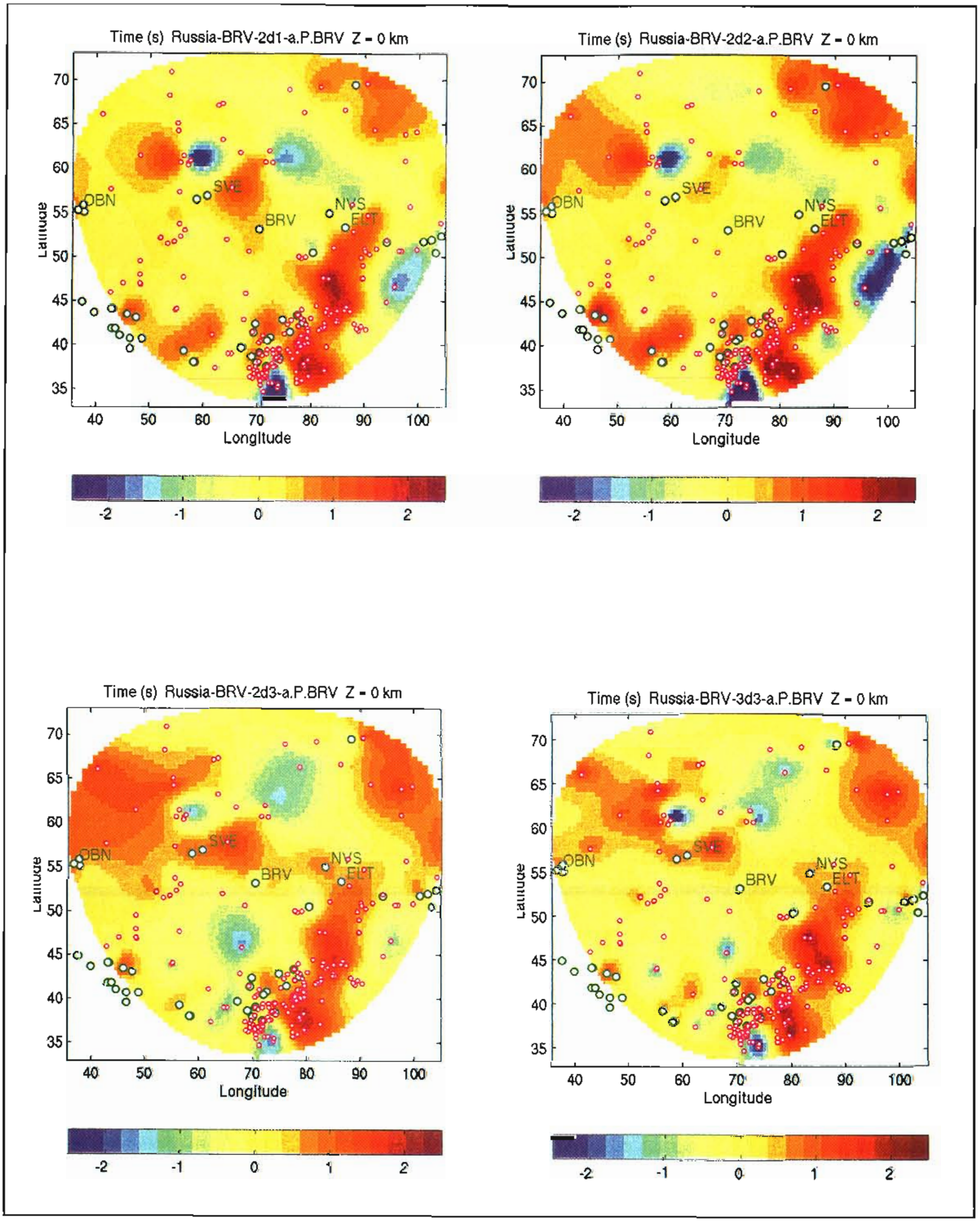

Figure 6-10. Travel-time correction functions for station BRV, generated from four different parameter functions: 2-D time-term function (top left), 2-D time factor function (top right), 2-D mislocation-vector function (bottom left), and 3-D mislocation-vector function (bottom right).

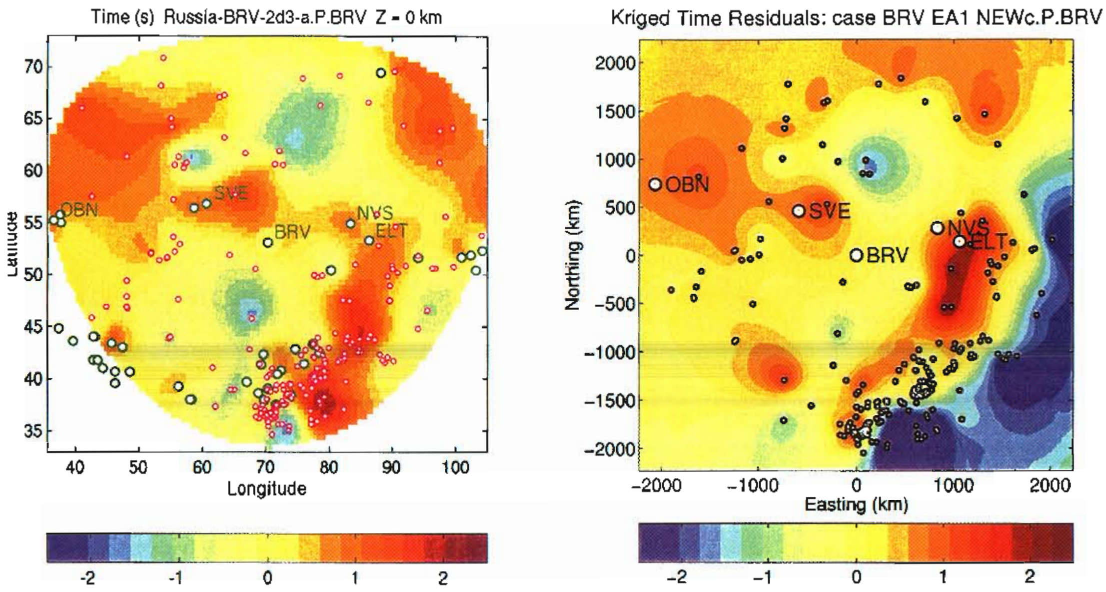

Figure 6-11. Comparison of travel-time correction functions at BRV obtained from multiple-station (left) and station-specific (right) kriging. The multiple-station function is based on the 2-D mislocation-vector parameter function.

suggests that this part of the single-station function for BRV was either not well-determined by the BRV residuals or was inconsistent with the pattern of residuals at other stations.

Finally, Figure 6-12 shows the travel-time correction functions for the other four stations considered earlier. Each is derived from the 2-D mislocation-vector parameter function. Unlike in the station-specific versions, stations ELT and NVS (top panels of figure) now have nearly identical travel-time corrections, consistent with their small separation (267 km). SVE and OBN (bottom panels) are less correlated since they have a greater separation. By design, source-receiver reciprocity is now obeyed between all station pairs.

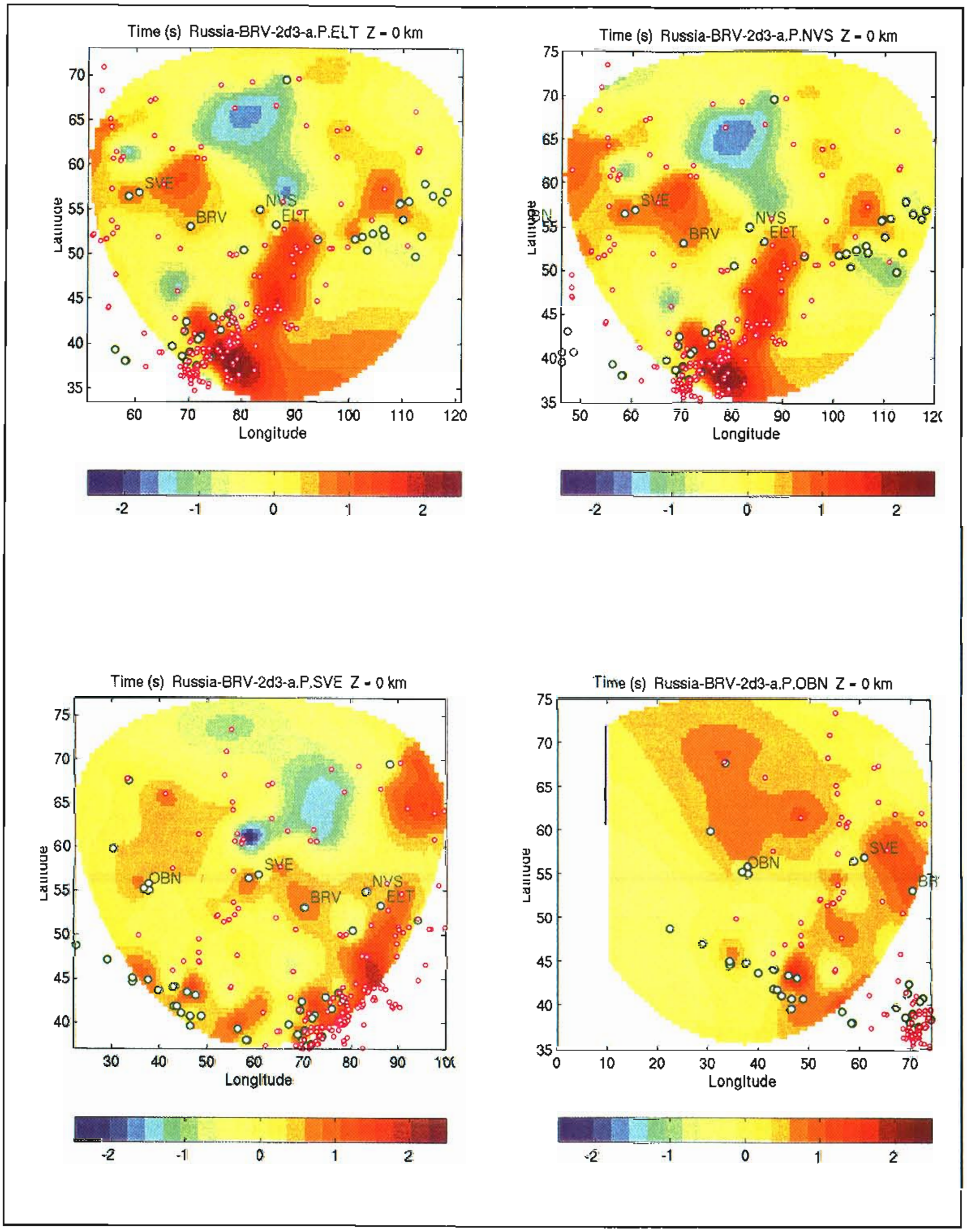

Figure 6-12. Travel-time correction functions for 4 stations, all generated from 2-D mislocation-vector parameter function: station ELT (top left), station NVS (top right), station SVE (bottom left), and station OBN (bottom right).

SECTION 7

SUMMARY AND CONCLUSIONS

7.1 PRINCIPAL FINDINGS

This report describes the results of a three-year project designed to improve capabilities to locate seismic events in eastern Asia by using regional calibration of seismic travel times. The main objective of this research project has been to calibrate the travel time characteristics of the earth's crust and upper mantle beneath this region over the depth range sampled by regional seismic ray paths to each of 30 IMS stations from all source locations of potential interest. The research reported here was performed by a Consortium of institutions led by SAIC and including scientists from Massachusetts Institute of Technology's Earth Research Laboratory, Weston Geophysical Corporation, and the Russian Institute for Dynamics of the Geospheres.

One of the principal results of this research has been the demonstration that a 3-D velocity model representative of this Group 1 region, based on prior knowledge and refined using GT calibration data, can be used to determine very accurate regional travel times for P and S waves. Such accurate travel time predictions enable implementation of source specific station corrections which improve the accuracy of seismic locations, particularly for smaller events which may be located with observations from limited numbers of stations and often include data from complex or secondary seismic phases at regional stations. The travel time predictions at each station are represented as a combination of model-based travel times plus empirical corrections. For the model-based component, we have utilized and demonstrated the capabilities of a state-of-the-art 3-D raytracing program. The latter provides efficient and accurate estimates of seismic travel times through the complex velocity structures present in this region. This raytracing algorithm has also proven to be valuable in computing sensitivities of travel times to velocity changes throughout the model, which have been used in a tomographic inversion to refine and improve the 3-D velocity model for subregions within Group 1 which have more complete calibration data.

As a part of the calibration and validation efforts for the Group 1 region, a large database of travel time observations from GT events has been assembled and archived. These data include an unique FSU explosion database including GT nuclear tests and PNE explosions covering large parts of the region. Travel times from other GT events for the India/Pakistan and China/Mongolia regions have also been included in this calibration database archive. These have all provided important data for refining the 3-D velocity models in each of the sub-areas which make up the overall Group 1 region of eastern Asia.

Validation efforts for our final 3-D velocity model for the Group 1 region have included several different comparisons and analyses of seismic travel time residuals and location errors. These validation analyses have shown that P-wave travel time errors are very small for our refined 3-D model compared to nominal IASPEI91 travel times. Therefore, the corrected travel times from these 3-D models have very small bias and the RMS scatter is greatly reduced. Furthermore, where the GT events have been available to test location accuracy in the Group 1 region, we have found significant reductions in the location errors for errors for events located with the 3-D model travel times over the IASPEI91 times.

As a part of this research program, we have also conducted preliminary investigations using this same approach to calibrate travel times for secondary seismic phases from the Group 1 region. Although this approach appears promising, some additional study will be needed to fully demonstrate its potential for routine event location. We used an analysis of Poisson's ratio in the earth's crust and upper mantle to determine a 3-D S-wave velocity model, which is based on our final 3-D P-wave velocity model for the Group 1 region. We conducted limited testing of this S-wave model and the associated travel time calculations following similar raytracing procedures to those used for P. These indicate that the computed travel times are generally consistent with S-wave travel time observations from GT events in the region. However, we have also found that the travel time variance for the corrected S waves are much larger than for the corresponding P waves. This suggests that for even a very good S-wave velocity model, the S times should be significantly down-weighted in the seismic location scheme.

Finally, as a product of this research program, the final P- and S-wave SSSCs for the 30 IMS stations in the Group 1 region have been determined and delivered. These SSSCs have been provided for distances out to 20° from each of the stations and for a range of 11 potential focal depths, from the earth's surface down to 200 km. Application of these SSSCs to regional travel time observations at these Group 1 stations is expected to result in accurate travel times which can be used with observations from teleseismic stations to provide better locations for small events from this region of eastern Asia.

7.2 SOME SPECIFIC RESULTS

In addition to the main conclusions and deliverables, this Group 1 project has produced a number of additional results which have contributed to improved understanding of seismic location calibration across this region of interest in eastern Asia. Some additional accomplishments of this program are:

- A final 3-D velocity model of the entire Group 1 area covering the region of eastern Asia has been formulated which incorporates both P and S velocity distributions at resolutions ranging from 1/3 to 1 degree across the area of interest.
- A version of the Soviet explosion ground truth database consisting of 1000 carefully validated, regional distance initial P-wave arrival time observations from distinct FSU PNE and weapons tests has been completed and delivered.
- A sophisticated, fully nonlinear tomographic inversion module has been formulated, implemented, and applied to the refinement of the upper mantle P-wave velocity distributions for the DSS, China/Mongolia, and WINPAK3D sub-regions, where the calibration data were more abundant. These sub-models have been incorporated into the overall 3-D model for the larger study region.
- Numerous features found in the tomographic refinement of the 3-D velocity models have been seen to correlate with mapped tectonic structures from geologic maps of the eastern Asia region. This supports qualitatively our conclusion that the tomographic inversion procedure is producing reasonable results.
- Further extensive testing of the tomographically refined P velocity models using the available data from ground truth events indicates that the corresponding travel time

predictions have essentially zero bias and total RMS model errors on the order of 1 second across much of the Group 1 study region.

- The estimated errors computed for the refined 3-D regional velocity model represent significant improvement over the default IASPEI91 model in the FSU region which produces an average bias of – 3.65 seconds and RMS errors of more than 2 seconds.
- Regional seismic event location accuracies for a widely distributed sample of 21 FSU PNEs with GT0, using observations at from 4 to 6 IMS or surrogate stations, show an average mislocation of only 6.9 km using the refined regional model, as compared to an average mislocation of 20.4 km for the same data using the IASPEI91 model.
- Similar analyses of 20 Novaya Zemlya explosions, with a small network of IMS or surrogate stations, also indicates an average mislocation less than 10 km for the 3-D regional velocity model compared to an average mislocation of 44 km obtained for the IASPEI91 model.
- Ground truth data from Chinese National Network stations for Lop Nor explosions and selected better located events from the India/Pakistan region have produced similar validation results supporting our final refined 3-D regional velocity models for the China/Mongolia and India/Pakistan subregions.
- Knowledge of Poisson's ratio in the earth's crust and upper mantle can be used to convert the 3-D regional P-wave velocity model to a reasonable S-wave velocity model which can be used to predict travel times of secondary seismic phases.
- Measurement errors and travel time prediction uncertainties for regional S waves and other secondary phases appear to diminish the value of such observations for event location.
- A new reciprocal kriging method for handling empirical travel time errors, left over after modeling corrections, appears promising. Application of these empirical corrections on top of the model-based corrections results in reduced RMS errors on the order of 0.7 seconds in regions of the FSU where the best calibration data are available for testing the methods.
- The small residual errors which are left after the combined model-based and empirical corrections appear to be approaching the limits of improvements to be expected from seismic travel time calibration methods.

7.3 OPPORTUNITIES FOR FUTURE DEVELOPMENT

The procedures, velocity models, and ground truth data developed under this project are valuable resources for use in locating seismic events occurring throughout eastern Asia. Application of the SSSCs developed here have been demonstrated to significantly reduce location errors and uncertainties for regional seismic events determined by observations from the relevant stations. However, there are a number of areas where these procedures and results could be improved.

Additional work is needed to improve the velocity models in several areas. In particular, information on the regional velocity structure from several of the subregions (e.g. far eastern Russia, southeastern Asia, and adjacent oceanic regions) included in this large area of eastern Asia is very sparse. Throughout this project we saw evidence that the use of velocity models based on analyses of longer period surface waves, to provide background or fill-in where more complete knowledge was lacking, produced insufficiently accurate estimates of short-period regional body-wave seismic travel times. More complete knowledge based on regional travel times would be most useful to improve the models in several of these subregions.

Equally important to better knowledge of velocity models is expanded calibration data. The most reliable travel time predictions can be generated in regions where the velocity models have been tested and validated with good observations from accurate ground truth events. We found in our tomographic analyses that the velocity models could be refined and improved in several parts of the eastern Asia study region (e.g. DSS, WINPAK, and China/Mongolia) where calibration data were more complete. Additional ground truth events and calibration data could provide better velocity models in many of the subregions of eastern Asia. Such data are particularly needed in some of the areas (such as those cited above) where there is little prior knowledge available of the velocity structure. Even some of the areas where tomographic analyses were conducted during this project could be further refined using additional and more reliable calibration data to fill in some coverage gaps. For example, more accurate ground truth from selected events in the China/Mongolia region could lead to additional tomographic refinements and model improvements over parts of that subregion.

During the course of this project, work on travel time calibration for secondary seismic phases was very limited. Although the eastern Asia model which we developed for S-wave velocities looks very promising, we performed only very limited validation tests. Additional ground truth and accurate S-wave travel time observations would be very valuable for improving the S velocity model in this region. As noted above, uncertainties in travel time picks for S waves and other secondary phases are particularly problematic for utilizing these signals in location schemes. Thus, an important element for improving utilization of these secondary seismic phases in regional location will be development of consistent timing procedures. This is especially a problem for the explosion sources, for which S signal onsets are often quite emergent. Unfortunately, it is just such explosion sources which most often provide the best ground truth. So, there is a clear need for significant additional work in data collection and analysis if secondary seismic phases are to be made useful for improving the location accuracy for regional seismic events.

Finally, the advanced kriging procedures which have been developed as part of this project appear to provide a more realistic approach to represent the empirical errors and travel time uncertainties. In this project we have mainly tested these procedures in subregions where the calibration data were more abundant. More complete analyses of these reciprocal kriging methods and their sensitivities to model and travel time measurement uncertainties throughout this Group 1 study region as well as other regions of interest would be valuable.

SECTION 8

APPENDIX. SURFACE FOCUS P-WAVE SSSCs AT GROUP 1 IMS STATIONS

P-wave and S-wave SSSCs have been computed using the procedures based on three-dimensional seismic velocity models described in this report for all 30 IMS station sites in the Group 1 calibration region of eastern Asia. The figures on the following pages show plots of the surface-focus P-wave SSSCs which illustrate the results accomplished on this project. The digital versions of these SSSCs along with those from 10 additional focal depths, covering potential focal depths throughout the earth's crust and upper mantle ($h \leq 200$ km) have been computed and delivered.

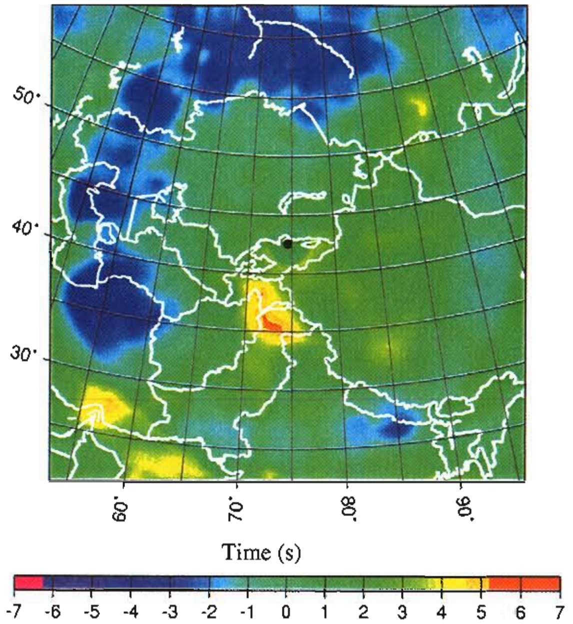

Figure 8-1. Surface focus P-wave SSSCs for station AAK range from –4.6 seconds to +5.4 seconds.

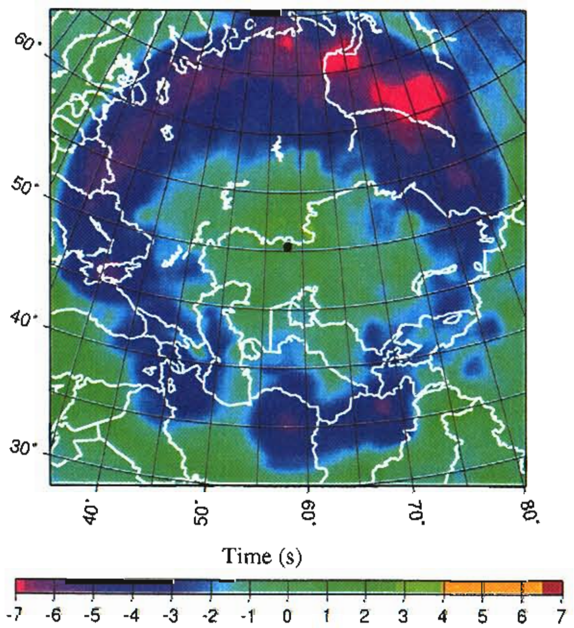

Figure 8-2. Surface focus P-wave SSSCs for station AKTO range from –8.1 seconds to +3.1 seconds.

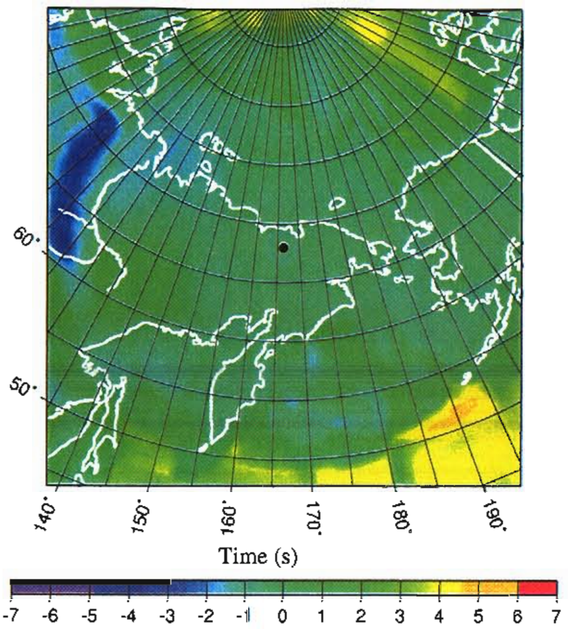

Figure 8-3. Surface focus P-wave SSSCs for station BIL range from –3.8 seconds to +5.0 seconds.

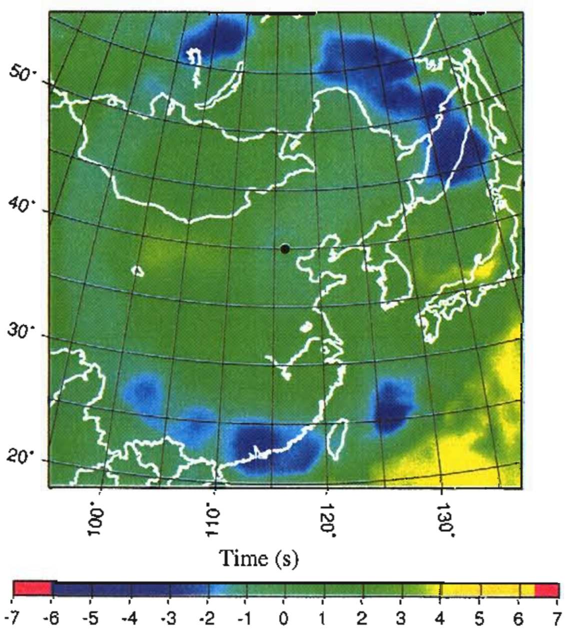

Figure 8-4. Surface focus P-wave SSSCs for station BJT range from –5.0 seconds to +4.3 seconds.

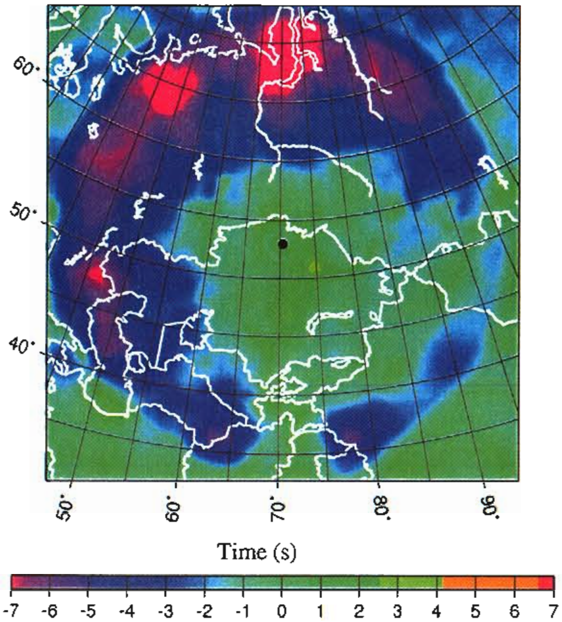

Figure 8-5. Surface focus P-wave SSSCs for station BRVK range from –9.2 seconds to +3.0 seconds.

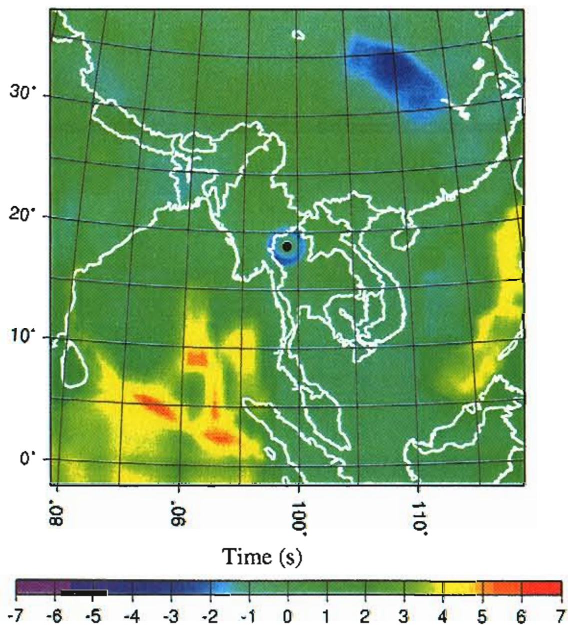

Figure 8-6. Surface focus P-wave SSSCs for station CMTO range from –2.9 seconds to +5.8 seconds.

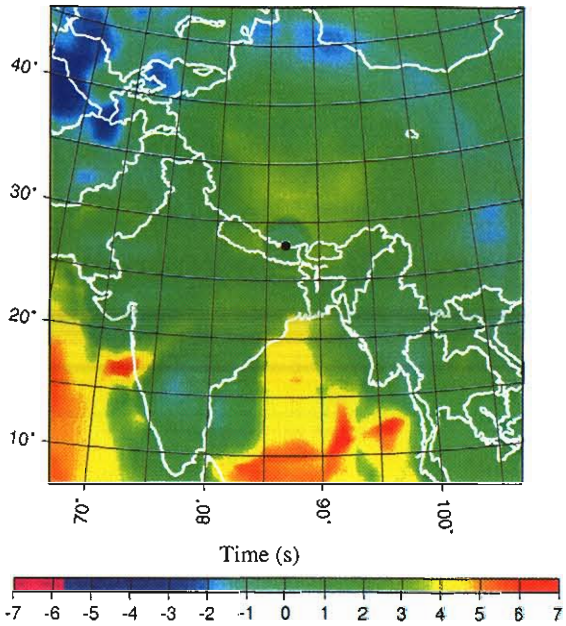

Figure 8-7. Surface focus P-wave SSSCs for station EVN range from –4.0 seconds to +6.7 seconds.

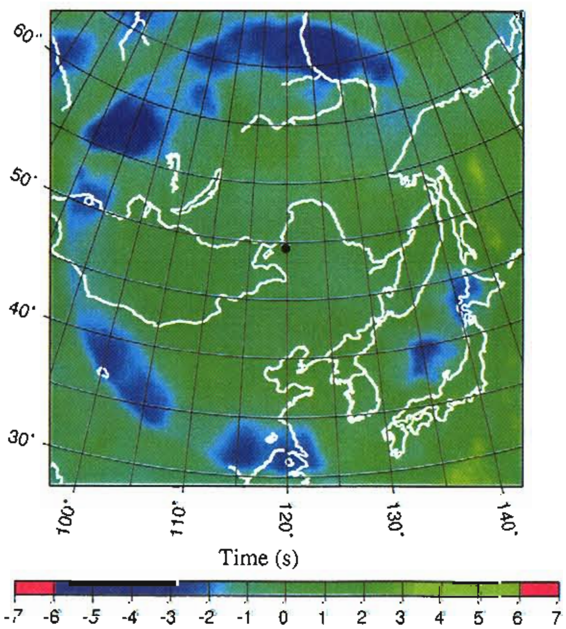

Figure 8-8. Surface focus P-wave SSSCs for station HILR range from –4.4 seconds to +3.4 seconds.

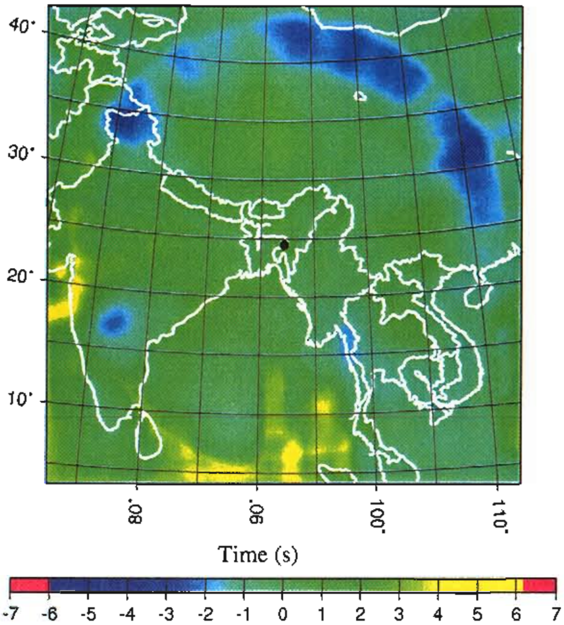

Figure 8-9. Surface focus P-wave SSSCs for station JURI range from –3.1 seconds to +5.1 seconds.

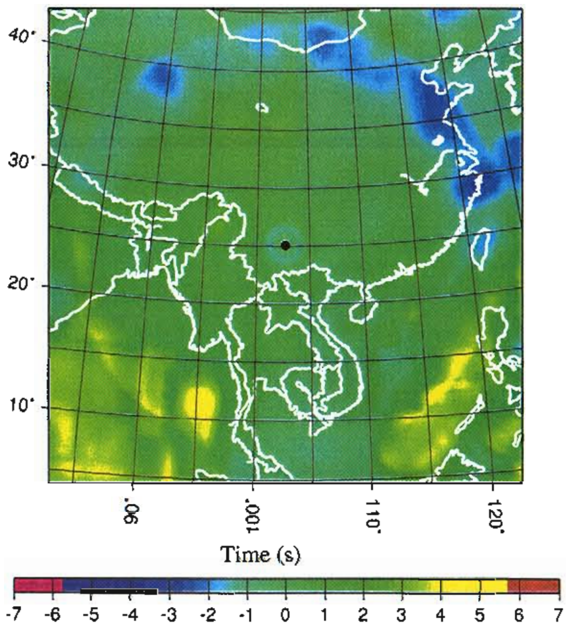

Figure 8-10. Surface focus P-wave SSSCs for station KMI range from –2.7 seconds to +4.9 seconds.

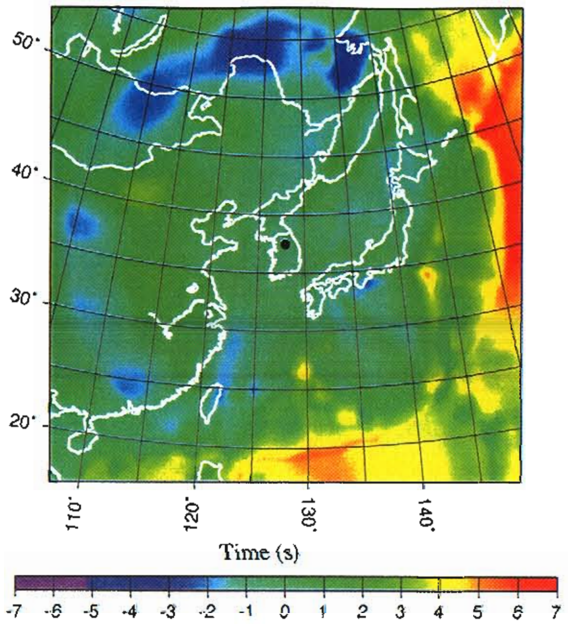

Figure 8-11. Surface focus P-wave SSSCs for station KSRS range from –3.8 seconds to +7.0 seconds.

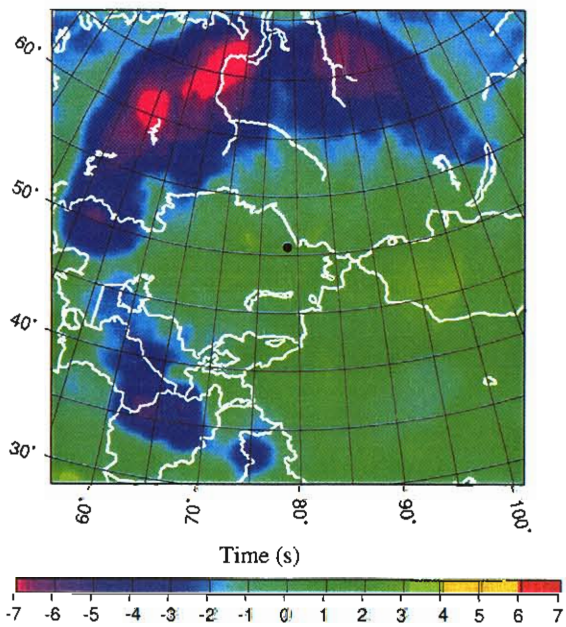

Figure 8-12. Surface focus P-wave SSSCs for station KURK range from –8.1 seconds to +3.8 seconds.

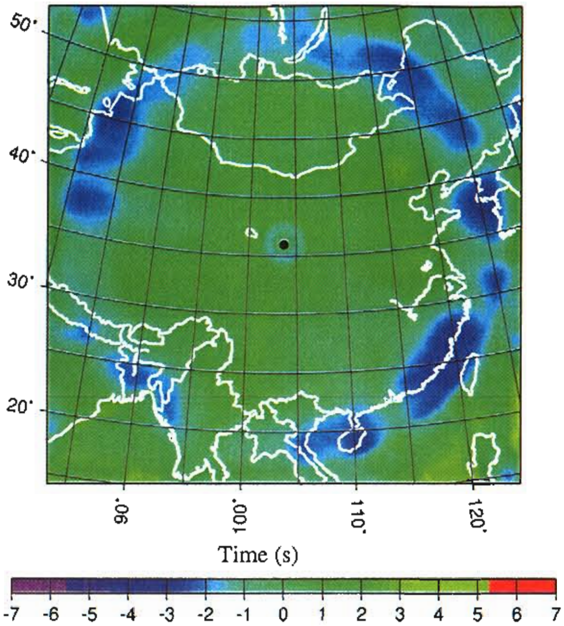

Figure 8-13. Surface focus P-wave SSSCs for station LZDM range from –3.2 seconds to +3.3 seconds.

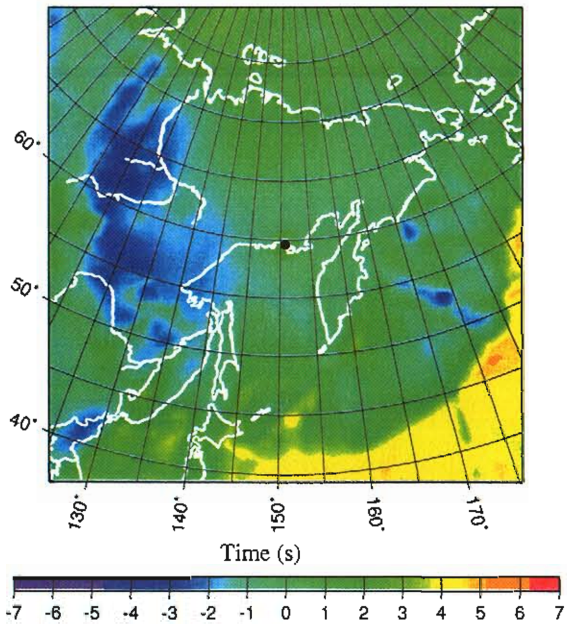

Figure 8-14. Surface focus P-wave SSSCs for station MA2 range from –3.8 seconds to +5.2 seconds.

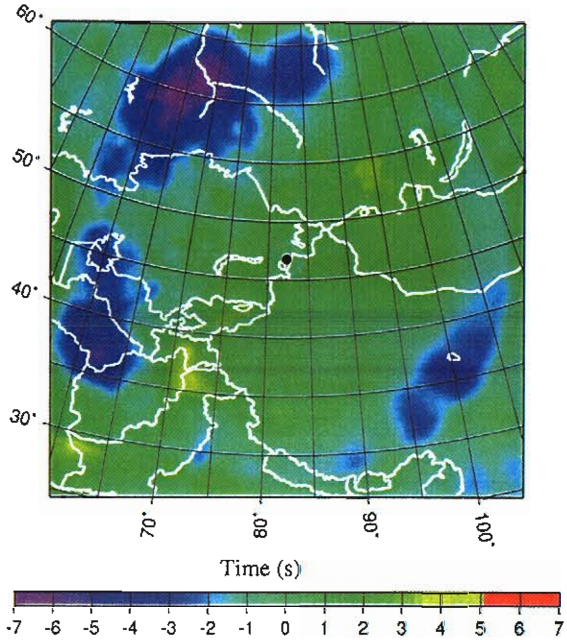

Figure 8-15. Surface focus P-wave SSSCs for station MKAR range from –6.4 seconds to +4.0 seconds.

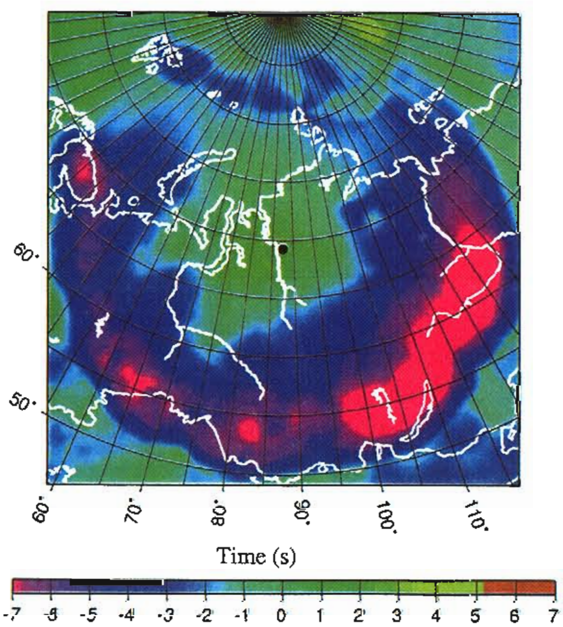

Figure 8-16. Surface focus P-wave SSSCs for station NRIK range from –8.9 seconds to +3.3 seconds.

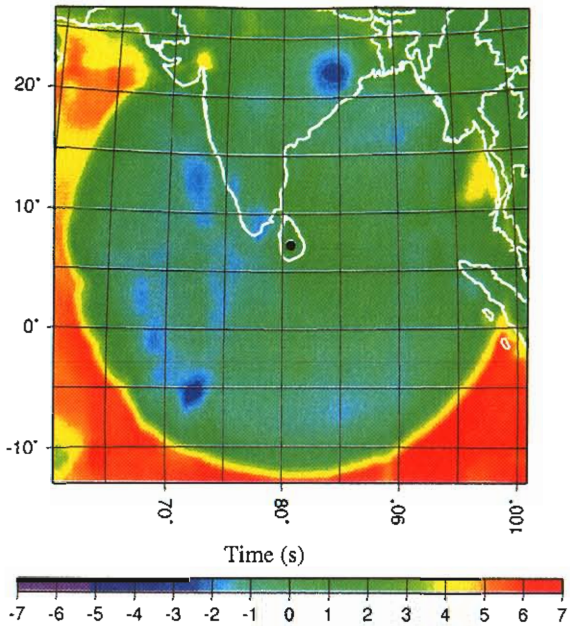

Figure 8-17. Surface focus P-wave SSSCs for station PALK range from –2.8 seconds to +6.5 seconds.

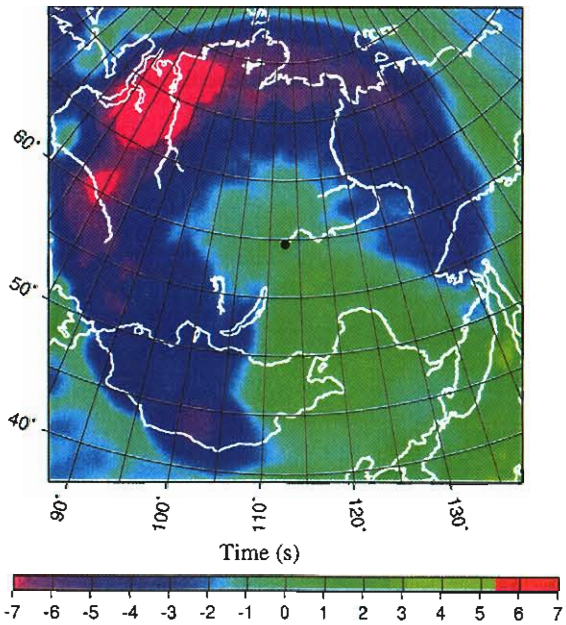

Figure 8-18. Surface focus P-wave SSSCs for station PDY range from –8.8 seconds to +3.6 seconds.

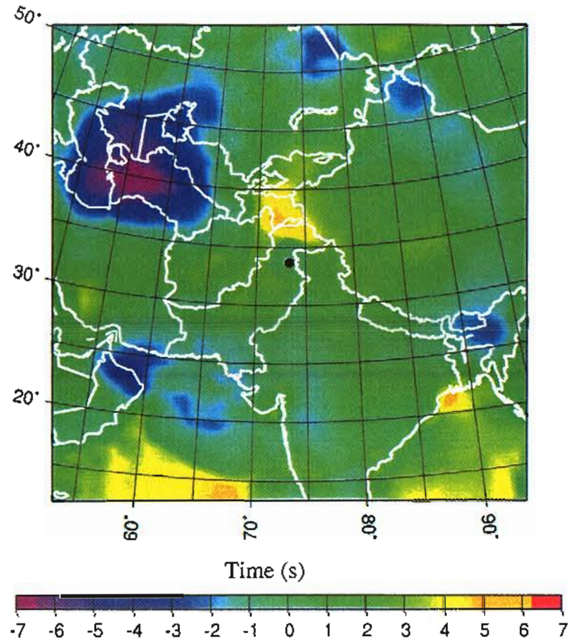

Figure 8-19. Surface focus P-wave SSSCs for station PRPK range from −7.3 seconds to +5.3 seconds.

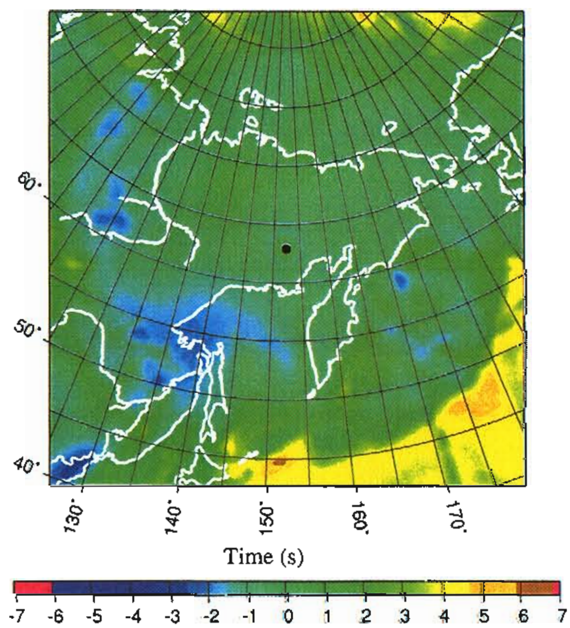

Figure 8-20. Surface focus P-wave SSSCs for station SEY1 range from −2.8 seconds to +6.7 seconds.

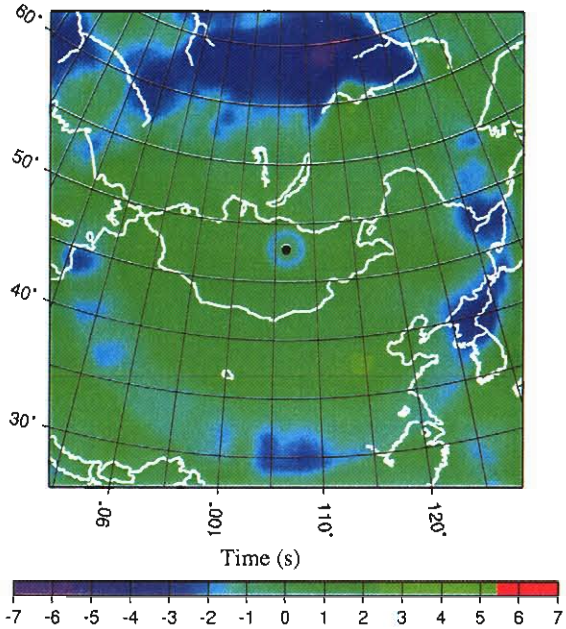

Figure 8-21. Surface focus P-wave SSSCs for station SONM range from –5.3 seconds to +2.7 seconds.

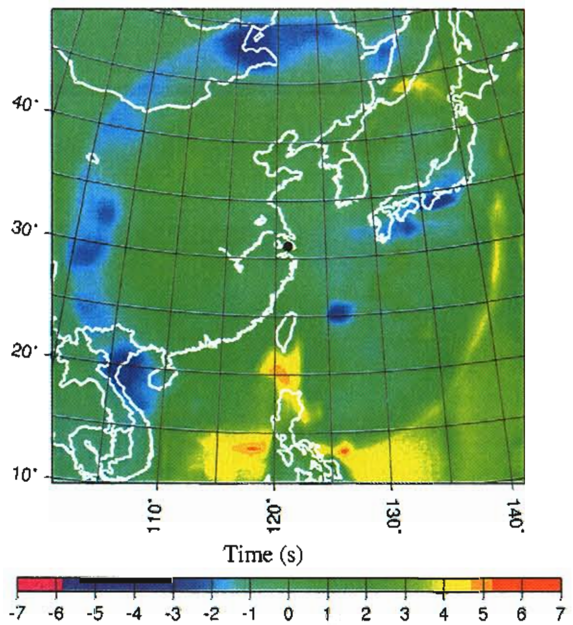

Figure 8-22. Surface focus P-wave SSSCs for station SSE range from –3.7 seconds to +5.6 seconds.

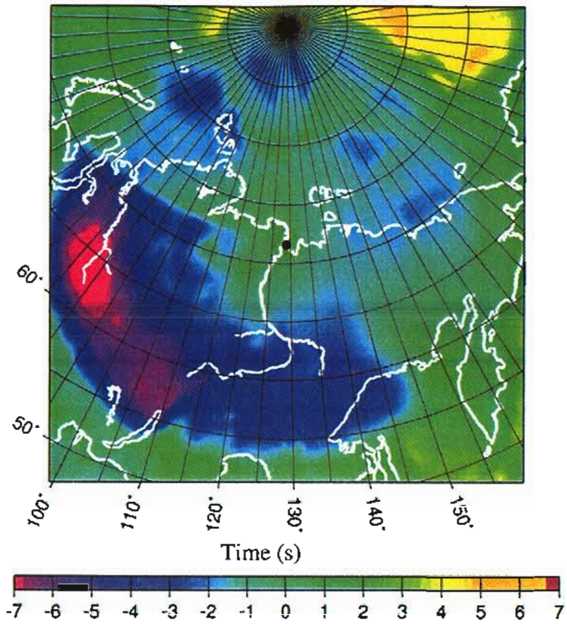

Figure 8-23. Surface focus P-wave SSSCs for station TIXI range from −8.0 seconds to +5.1 seconds.

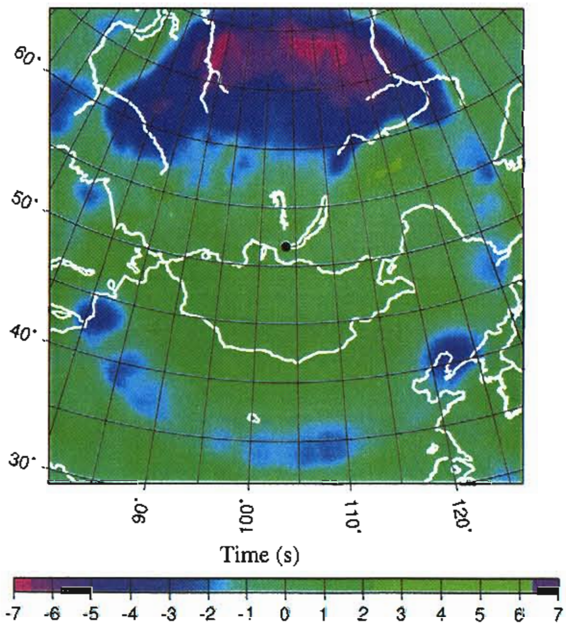

Figure 8-24. Surface focus P-wave SSSCs for station TLY range from −6.9 seconds to +3.0 seconds.

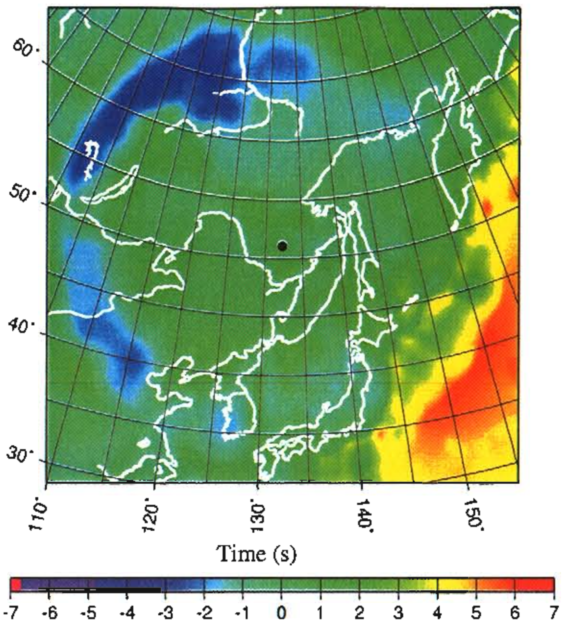

Figure 8-25. Surface focus P-wave SSSCs for station URG range from –3.6 seconds to +6.0 seconds.

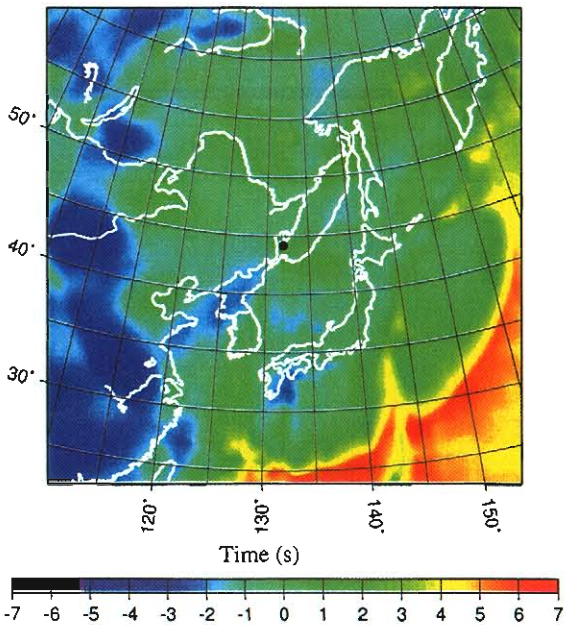

Figure 8-26. Surface focus P-wave SSSCs for station USK range from –4.6 seconds to +7.3 seconds.

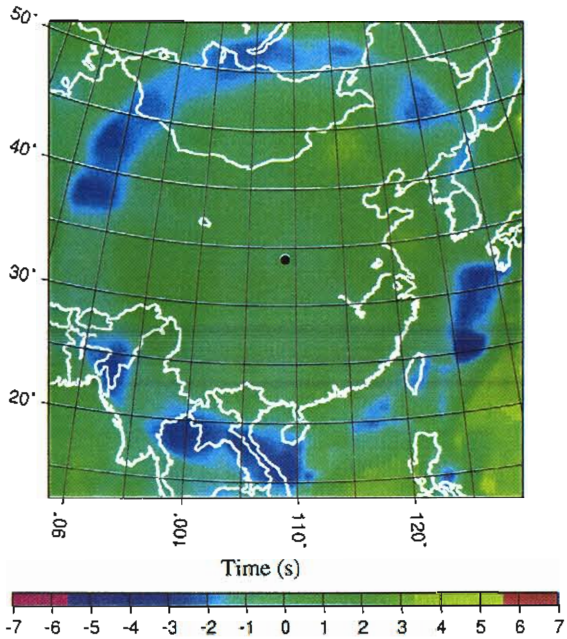

Figure 8-27. Surface focus P-wave SSSCs for station XAN range from –4.1 seconds to +4.0 seconds.

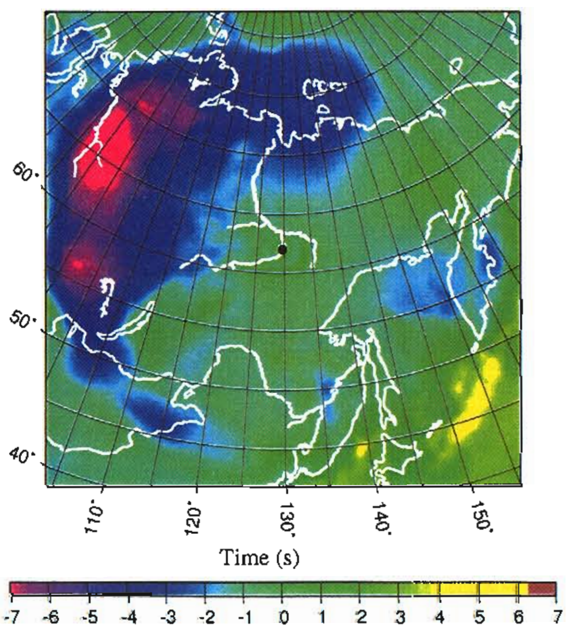

Figure 8-28. Surface focus P-wave SSSCs for station YAK1 range from –8.2 seconds to +5.4 seconds.

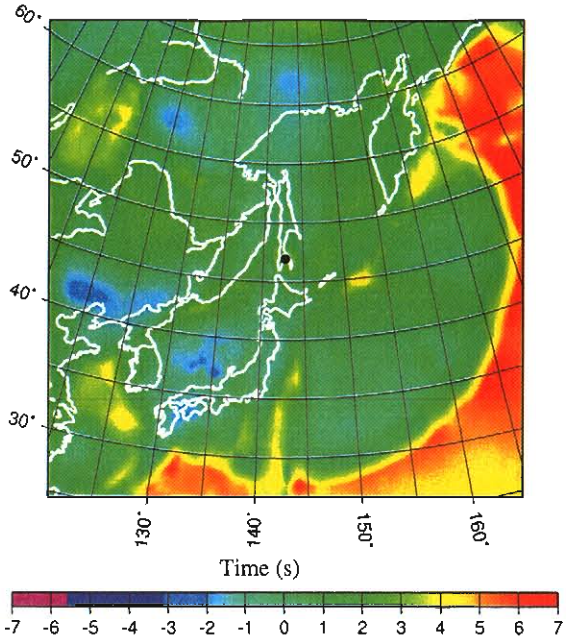

Figure 8-29. Surface focus P-wave SSSCs for station YSS1 range from –2.4 seconds to +7.3 seconds.

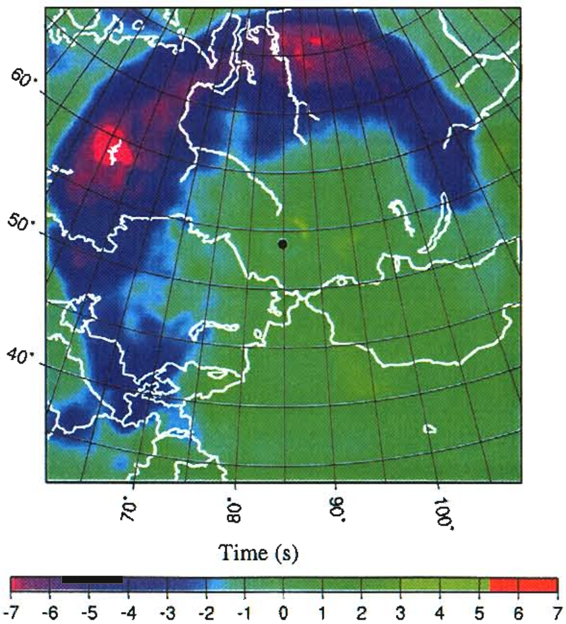

Figure 8-30. Surface focus P-wave SSSCs for station ZAL range from –7.8 seconds to +3.4 seconds.

SECTION 9

REFERENCES

Deutsch, C.V., and A.G. Journel (1998). *GSLIB Geostatistical Software Library and User's Guide*, 2nd ed., Oxford University Press, Inc., New York, 369 pp.

Engdahl, E. R., and E. Bergman (2001). Validation and generation of reference events by cluster analysis, *Proceedings*, 23rd Annual DTRA/NNSA Seismic Research Review, Jackson Hole, Wyoming.

Engdahl, E. R., R. van der Hilst, and R. Buland (1998). Global teleseismic earthquake relocation with improved travel times and procedures for depth determination, *Bull. Seism. Soc. Amer.* **88**, 722-743.

Fisk, M. D. (2002). Accurate locations of nuclear explosions at the Lop Nor Test Site using alignment of seismograms and IKONOS satellite imagery, *Bull. Seism. Soc. Amer.* 92, 2911-2925.

Johnson, M. and C. Vincent (2002). Development and Testing of a 3-D Velocity Model for Improved Event Location: A Case Study for the India-Pakistan Region, *Bull. Seism. Soc. Amer.* 92, 2893-2910.

Jordan, T. H., and K. A. Sverdrup (1981). Teleseismic location techniques and their application to earthquake clusters in the south-central Pacific, *Bull. Seism. Soc. Am.* **71**, 1105-1130.

Kennett, B.L.N., and E. R. Engdahl (1991). Travel times for global earthquake location and phase identification, *Geophys. J. Int.* **105,** 429-465.

Lomax, A. (1999). Probabilistic, non-linear earthquake location in 3-D media (An online guide to software), http://iapetus.unice.fr/~lomax/nlloc.

Moser, T.J. (1991). Shortest path calculation of seismic rays, *Geophysics*, **56**, 59-67.

Murphy, J. R., R. W. Cook, and W. L. Rodi (1998). Improved focal depth determinations for use in CTBT monitoring, *Proceedings*, 20th Annual Seismic Research Symposium on Monitoring a Comprehensive Test Ban Treaty, 255-264.

Murphy, J. R., R. W. Cook, and W. L. Rodi (2000). Improved focal depth determination for use in seismic monitoring of underground nuclear explosions, *Final Report*, Maxwell Technologies Report No. MSD-DFR-00-16621.

Murphy, J., W. Rodi, M. Johnson, I. Kitov, D. Sultanov, B. Barker, C. Vincent, V. Ovtchinnikov, and Y. Shchukin (2001). Seismic Calibration of Group 1 IMS

Stations in Eastern Asia for Improved IDC Event Location, *Interim Technical Report* SAIC-01/1021, SAIC, San Diego, CA.

Murphy, J. R., B. W. Barker, and W. L. Rodi (2002). Improved focal depth determination for use in nuclear explosion monitoring, Proceedings, 24th Seismic Research Review – Nuclear Explosion Monitoring: Innovation and Integration, Ponte Vedra Beach, FL.

Myers, S. C., and C. A. Schultz (1998). Demonstrating Improvement in Seismic Source Location Using Bayesian Kriging: A Case Study of the 1991 Racha Aftershock Sequence, *20th Annual Seismic Research Symposium*, Santa Fe.

Nolet, G. (1983). Inversion and resolution of linear tomographic systems (abstract). *Eos, Trans. Am. Geophys. Union* **74**, 775-776.

Paige, C.C., and M. A. Saunders (1982). LSQR: An algorithm for sparse linear equations and sparse least squares, *ACM Transactions on Mathematical Software*, March 1982.

Podvin, P., and I. Lecomte (1991). Finite difference computation of travel times in very contrasted velocity models: a massively parallel approach and its associated tools, *Geophys. J. Int.* **105,** 271-284.

Rodi, W. (2002). Algorithms for Calibration and Uncertainty Analysis in Seismic Event Location, *Proceedings*, The Fourth Location Workshop, Expert Group on Event Location Calibration, Oslo, Norway, 22-26 April.

Rodi, W., and M.N. Toksöz (2000). Grid-search techniques for seismic event location, *Proceedings*, 22nd Annual DoD/DOE Seismic Research Symposium.

Rodi, W.L., J.F. Masso, J.M. Savino, T.H. Jordan and J.B. Minster (1981). Relocation of earthquakes in eastern Washington based on a three-dimensional velocity model, *Final Technical Report* SSS-R-81-4857, S-Cubed, San Diego.

Rodi, W., C.A. Schultz, W.G. Hanley, S. Sarkar and H.S. Kuleli (2002). Grid-search location methods for ground-truth collection from local and regional seismic networks, *Proceedings*, 24th Annual DoD/DOE Seismic Research Review, Ponte Vedra Beach, Florida, DOE NNSA, 394–402.

Rodi, W., R. Engdahl, E. Bergman, F. Waldhauser, G. Pavlis and M. N. Toksoz (2002). A new grid-search multiple-event location algorithm and a comparison of methods, submitted to *Proceedings*, 24rd Annual DoD/DOE Seismic Research Review, Ponte Vedra Beach, Florida, DOE NNSA.

Rodi, W., S.C. Myers and C.A. Schultz (2003). Grid-search location methods for ground-truth collection from local and regional seismic networks, *Proceedings*,

25th Annual DoD/DOE Seismic Research Review, Tucson, Arizona, DOE NNSA.

Schultz, C. A., S. C. Myers, J. Hipp and C. J. Young (1998). Nonstationary Bayesian Kriging: A Predictive Technique to Generate Spatial Corrections for Seismic Detection, Location and Identification, *Bull. Seism. Soc. Am.* **88**, 1275-1288.

Seeber, L., and J. Armbruster (1979). Seismicity of the Hazara Arc in northern Pakistan: decollement vs basement faulting, in *Geodynamics of Pakistan*, A. Farah and K. A. DeJong (Editors), *Geological Survey of Pakistan,* 131-142.

Spencer, C., and D. Gubbins (1980). Travel-time inversion for simultaneous earthquake location and velocity structure determination in laterally varying media, *Geophys. J. R. Astr. Soc. 63*, 95-116.

Stevens, J. L., and D. A. Adams (1999). Improved Surface Wave Detection and Measurement Using Phase-Matched Filtering and Improved Regionalized Models, *Proceedings of the 21st Annual Seismic Research Symposium in Las Vegas, NV*, 274-282.

Stevens, J. L., D. A. Adams and G. E. Baker (2001). Improved surface wave detection and measurement using phase-matched filtering with a global one-degree dispersion model, *Proceedings of the 23rd Seismic Research Review: Worldwide Monitoring of Nuclear Explosions*, 420-430.

Twomey, S. (1977). *Introduction to the Mathematics of Inversion in Remote Sensing and Indirect Measurements*. Elsevier, Amsterdam.

Vidale, J. (1988). Finite difference calculations of travel times, *Bull. Seismol. Soc. Amer.* **78**, 2062-2076.

Vidale, J. (1990). Finite difference calculations of travel times in three dimensions, *Geophys.* 55, 521-526.

DISTRIBUTION LIST
DTRA-TR-03-25

DEPARTMENT OF DEFENSE

DEFENSE TECHNICAL INFORMATION CENTER
8725 JOHN J. KINGMAN ROAD,
SUITE 0944
FT. BELVOIR, VA 22060-0944
2 CYS ATTN: DTIC/OCA

DEFENSE THREAT REDUCTION AGENCY
8725 JOHN J. KINGMAN ROAD MS 6201
FT. BELVOIR, VA 22060-6218
2 CYS ATTN: TDND/D. BARBER

DEPARTMENT OF DEFENSE CONTRACTORS

ITT INDUSTRIES
ITT SYSTEMS CORPORATION
1680 TEXAS STREET, SE
KIRTLAND AFB, NM 87117-5669
2 CYS ATTN: DTRIAC
ATTN: DARE

SCIENCE APPLICATIONS INTERNATIONAL
CORPORATION
10260 CAMPUS DRIVE
MAIL STOP X1
SAN DIEGO, CA 92121
ATTN: J.R. MURPHY